1 Highlights

2 Thermal and magnetic evolution of an Earth-like planet with a basal magma ocean

- ³ Victor Lherm, Miki Nakajima, Eric G. Blackman
- The structural, thermal, buoyancy, and magnetic evolution of an Earth-like planet is investigated
- The planet evolution includes a transient iron-rich basal magma ocean with a time-dependent composition
- The nominal model predicts a basal magma ocean dynamo followed by a core dynamo after 1 billion years
- The model is sensitive to the initial temperature, mantle convection, composition, and radioactivity
 - An early silicate dynamo is possible with an electrical conductivity larger than 21500 S/m
- An early core dynamo is not possible with a thermal conductivity larger than 15.8 W/m/K

² Victor Lherm^{a,b,*}, Miki Nakajima^{a,b} and Eric G. Blackman^{b,c}

- ^aDepartment of Earth and Environmental Sciences, University of Rochester, 227 Hutchison Hall, Rochester 14627, NY, USA
- ^bDepartment of Physics and Astronomy, University of Rochester, 206 Bausch & Lomb Hall, Rochester 14627, NY, USA
 - ^cLaboratory for Laser Energetics, University of Rochester, 250 E River Rd, Rochester 14623, NY, USA

ARTICLE INFO

Keywords:

18 19

20

24

25

26

30

31

32

35

36 37

40

41

42

- 21 Terrestrial planets
 - Planetary evolution
- 23 Basal magma ocean
 - Dynamo
 - Magnetic field

ABSTRACT

Earth's geodynamo has operated for over 3.5 billion years. The magnetic field is currently powered by thermocompositional convection in the outer core, which involves the release of light elements and latent heat as the inner core solidifies. However, since the inner core nucleated no more than 1.5 billion years ago, the early dynamo could not rely on these buoyancy sources. Given recent estimates of the thermal conductivity of the outer core, an alternative mechanism may be required to sustain the geodynamo prior to nucleation of the inner core. One possibility is a silicate dynamo operating in a long-lived basal magma ocean. Here, we investigate the structural, thermal, buoyancy, and magnetic evolution of an Earth-like terrestrial planet. Using modern equations of state and melting curves, we include a time-dependent parameterization of the compositional evolution of an iron-rich basal magma ocean. We combine an internal structure integration of the planet with energy budgets in a coupled core, basal magma ocean, and mantle system. We determine the thermocompositional convective stability of the core and the basal magma ocean, and assess their respective dynamo activity using entropy budgets and magnetic Reynolds numbers. Our conservative nominal model predicts a transient basal magma ocean dynamo followed by a core dynamo after 1 billion years. The model is sensitive to several parameters, including the initial temperature of the core-mantle boundary, the parameterization of mantle convection, the composition of the basal magma ocean, the radiogenic content of the planet, as well as convective velocity and magnetic scaling laws. We use the nominal model to constrain the range of basal magma ocean electrical conductivity and core thermal conductivity that sustain a dynamo. This highlights the importance of constraining the parameters and transport properties that influence planetary evolution using experiments and simulations conducted at pressure, temperature, and composition conditions found in planetary interior, in order to reduce model degeneracies.

1. Introduction

- How planetary magnetic fields may protect planetary atmospheres from erosion by stellar winds is an active area
- of investigation (Lundin et al., 2007; Tarduno et al., 2010; Blackman and Tarduno, 2018; Gunell et al., 2018; Egan
- et al., 2019). In turn, magnetic fields may also influence the emergence of life and habitability (Tarduno et al., 2014;
- 48 Camprubí et al., 2019). Paleomagnetic evidence indicates the presence of a geomagnetic field for over 3.5 billion years
- (Gyr), potentially extending to 4.2 Gyr (Tarduno et al., 2010; Biggin et al., 2011; Tarduno et al., 2015; Borlina et al.,
- ⁵⁰ 2020; Tarduno et al., 2020; Bono et al., 2022; Taylor et al., 2023).
- The geomagnetic field is currently powered by thermal and compositional convection in the outer core, including
- the release of light elements at the inner core boundary (ICB) upon crystallization of the inner core (Jones, 2015).

ORCID(s): 0000-0001-5814-0637 (V. Lherm); 0000-0001-5014-0448 (M. Nakajima); 0000-0002-9405-8435 (E.G. Blackman)

^{*}Corresponding author

vlherm@ur.rochester.edu (V. Lherm); mnakajima@rochester.edu (M. Nakajima); blackman@pas.rochester.edu (E.G.

Since inner core nucleation depends on many factors, including the thermal evolution model of the planet, the current heat flow at the core-mantle boundary (CMB), and the radiogenic content of the core, the age of inner core formation is debated, but is typically less than 1.5 billion years ago (Ga) (Biggin et al., 2015; Labrosse, 2015; Nimmo, 2015b).

Therefore, an early geodynamo could not rely on buoyancy sources produced by the release of latent heat and light elements at the ICB.

Another key parameter that controls whether the outer core can sustain an early dynamo is the thermal conductivity of the core (Williams, 2018). If the thermal conductivity is excessively large, the heat of the core would be transferred by conduction rather than convection, leaving insufficient energy to power a dynamo. The thermal conductivity of the core was initially estimated in the range 20 – 50 W.m⁻¹.K⁻¹ (Stacey and Anderson, 2001; Stacey and Loper, 2007), with updated investigations confirming the low values (Basu et al., 2020; Hsieh et al., 2020). Recent experiments and simulations indicate values between 70 – 250 W.m⁻¹.K⁻¹ (de Koker et al., 2012; Ohta et al., 2016; Pozzo et al., 2012, 2022). The conflict between the upward revision of the thermal conductivity and the existence of a geomagnetic field throughout most of Earth's history is called the "new core paradox" (Olson, 2013).

A dynamo mechanism independent of core crystallization may be necessary to solve the "new core paradox" and sustain an early geomagnetic field (Landeau et al., 2022). The exsolution of light elements in the core, *e.g.* the precipitation of MgO or SiO₂ due to a decrease in solubility, could produce compositional convection and facilitate an early dynamo (O'Rourke and Stevenson, 2016; Hirose et al., 2017; Badro et al., 2018). However, the core must cool relatively quickly for this buoyancy source to overcome any early thermal stratification (Du et al., 2017, 2019). Mechanical forcing involving precession (Malkus, 1968; Stacey, 1973; Loper, 1975; Rochester et al., 1975; Tilgner, 2005) and tides (Le Bars et al., 2015; Grannan et al., 2017; Reddy et al., 2018) can also produce turbulent flows that could help generate an early magnetic field. Although tidal flows could have contributed to an early dynamo before 1.5 Ga, when the Earth's rotation rate and tidal deformation were higher, flows driven by precession seem too weak to drive the geodynamo (Landeau et al., 2022). Radioactive heating, rapid cooling, a colder solidus, a shallower core adiabat (Nimmo et al., 2004) and a high initial core temperature (Driscoll and Davies, 2023) may also have powered an early dynamo.

Alternatively, the early geomagnetic field may have been powered by a dynamo in a layer of molten silicates above the CMB (Labrosse et al., 2007; Ziegler and Stegman, 2013; Stixrude et al., 2020), known as a basal magma ocean (BMO). Several seismic and geochemical observations may be interpreted as remnants of an early BMO on Earth (Labrosse et al., 2015). This includes seismic heterogeneities above the CMB (Garnero and McNamara, 2008; Lay, 2015), including Large Low Shear Velocity Provinces (LLSVP) (Dziewonski et al., 1977; Lekic et al., 2012) and Ultra-Low Velocity Zones (ULVZ) (Garnero et al., 1993; Thorne and Garnero, 2004), as well as isotopic signatures

66

67

73

74

75

76

showing distinct geochemical reservoirs formed early in Earth's history (Boyet and Carlson, 2005; Mukhopadhyay, 2012; Mundl et al., 2017).

A primitive BMO could have been produced through several scenarios (Labrosse et al., 2015). At the end of 86 accretion, a giant impact may form a global magma ocean, which could crystallize downwards and form a BMO if 87 the intersection between the adiabatic temperature profile and the mantle liquidus occurs at mid-depth (Labrosse et al., 88 2007). Even if the intersection between the adiabat and the liquidus occurs at the CMB, crystals formed out of the 89 magma ocean are expected to be less dense than the melt. They should migrate upwards, leaving behind a denser iron-90 rich melt above the CMB (Boukaré et al., 2015; Nabiei et al., 2021). Alternatively, if the impact only melts a fraction 91 of the mantle (Tonks and Melosh, 1993; Nakajima et al., 2021), a dense metal silicate emulsion could accumulate at 92 the bottom of a local magma ocean (Rubie et al., 2015). The destabilization of this dense pond by diapirism (Karato 93 and Murthy, 1997; Samuel et al., 2010) or diking (Rubin, 1995; Stevenson, 2003) could then entrain molten silicates toward the core (Olson and Weeraratne, 2008), possibly forming a BMO. Finally, depending on the mechanisms of metal-silicate equilibration during (Kendall and Melosh, 2016; Landeau et al., 2021; Lherm et al., 2022; Lherm and Deguen, 2023) and after (Rubie et al., 2003; Deguen et al., 2014; Lherm and Deguen, 2018) a planetary impact, the 97 heat from core formation could be preferentially partitioned into the core and super-heat it. This could induce mantle melting above the CMB, resulting in a BMO.

After the formation of the BMO, iron, which is incompatible, is preferentially partitioned in the liquid as crystallization proceeds (Nomura et al., 2011; Andrault et al., 2012; Nabiei et al., 2021). Fractional crystallization is therefore responsible for the progressive enrichment of the BMO in iron, independently of the formation scenario. The density of the melt necessarily increases over time, leading to a gravitationally stable, long-lived BMO (Labrosse et al., 2007).

In order to understand planetary evolution, which includes processes operating at multiple scales, various models are required. For example, 3D models can capture turbulence, rotation, and dynamo effects in convective layers (Christensen and Wicht, 2015), 2D models can assess the role of solid-liquid multi-phase flow on the crystallisation of the BMO (Boukaré and Ricard, 2017), and fully 1D models can determine the thermal evolution of the planet using self-consistent radial distributions of thermodynamic and transport properties (Zhang and Rogers, 2022). Although these models accurately capture a variety of processes, they are computationally expensive. Alternatively, planetary evolution can be assessed using semi-analytical "box models" involving energy and entropy budgets (Nimmo, 2015a) averaged over each "box" (e.g. core, BMO, and mantle).

In an adiabatic (isentropic) and well-mixed layer such as a liquid core or a BMO, that involves a rapidly rotating, vigorously convective and electrically conductive fluid, the production of a self-sustained magnetic field requires that (i) thermocompositional convection supplies sufficient power to balance ohmic dissipation (Buffett et al., 1996; Lister,

100

101

102

103

104

105

106

107

108

109

110

111

112

113

114

2003) and that (ii) magnetic induction is significantly larger than magnetic diffusion (Christensen and Aubert, 2006).
 The power available to sustain a dynamo can be obtained by calculating energy and entropy budgets, while the induction
 criterion is assessed with a magnetic Reynolds number.

The theoretical framework governing energy and entropy budgets was originally developed for the Earth's core 119 (Verhoogen, 1961; Backus, 1975; Hewitt et al., 1975; Loper, 1978; Braginsky and Roberts, 1995; Lister and Buffett, 120 1995; Buffett et al., 1996; Gubbins et al., 2003, 2004; Nimmo, 2015a) to assess its thermal and magnetic evolution. 121 In particular, previous work investigated the age of the Earth's inner core (Labrosse et al., 1997, 2001), the influence 122 of radiogenic heating (Labrosse, 2003; Nimmo et al., 2004), the effect of light elements exsolution (O'Rourke and 123 Stevenson, 2016; O'Rourke et al., 2017; Mittal et al., 2020), the influence of a high thermal conductivities (Pozzo 124 et al., 2012; Gomi et al., 2013; Davies, 2015; Labrosse, 2015; Driscoll and Davies, 2023), the role of stably-stratified 125 layers in the core (Gomi et al., 2013; Laneuville et al., 2018; Greenwood et al., 2021) and the magnetic evolution of 126 super-Earth exoplanets (Blaske and O'Rourke, 2021; Bonati et al., 2021). In addition to planetary cores, energy and 127 entropy budgets have also been used to determine the thermal and magnetic evolution of a BMO on Earth (Labrosse 128 et al., 2007; Ziegler and Stegman, 2013; Laneuville et al., 2018; Blanc et al., 2020; Stixrude et al., 2020), Venus 129 (O'Rourke, 2020) and the Moon (Scheinberg et al., 2018; Hamid et al., 2023). 130

The magnetic Reynolds number of a convective and electrically conductive layer depends on the system length scale L, the typical convective velocity U, the magnetic constant μ_0 and the electrical conductivity σ

$$R_m = LU\mu_0\sigma. \tag{1}$$

When magnetic induction is significantly larger than magnetic diffusion, *i.e.* $R_m \gg 1$, a dynamo can operate and sustain a magnetic field. In practice, planetary dynamo simulations suggest $R_m = 40$ as a critical value (Christensen and Aubert, 2006) for large scale fields, consistent with kinematic helical convection dynamo calculations in a sphere (Chen et al., 2018).

In contrast to the core, where the dynamo is limited by the thermal conductivity, dynamo operation in a BMO is critically limited by the low electrical conductivity of the silicates. Assuming L = 300 km and U = 1 cm.s⁻¹ (Stixrude et al., 2020), the electrical conductivity required to reach the critical magnetic Reynolds number is typically $\sigma = 10^4$ S.m⁻¹. This exceeds the electrical conductivity of silicate melts at low pressure and temperature by at least two orders of magnitude (Ni et al., 2015). However, high pressure and temperature conditions (Scipioni et al., 2017), as well as the addition of metal, such as Fe and Ni (Holmström et al., 2018; Soubiran and Militzer, 2018; Stixrude et al., 2020), increase significantly the electrical conductivity of the silicates, potentially allowing a BMO to host a dynamo.

131

132

137

138

139

140

141

142

In this paper, we investigate the structural, thermal, buoyancy and magnetic evolution of a planet including a coupled solid mantle, a long-lived BMO and a solid and/or liquid core. Our goal is to obtain an evolution scenario for an Earth-like planet with a BMO and to assess the sensitivity of the model to key parameters. First, we establish an Earth-like nominal model using conservative parameters. We focus on the time evolution of the size of the BMO and the liquid core, as well as temperatures, compositions, heat flows, thermocompositional convective stability, rates of entropy production, magnetic Reynolds numbers and magnetic field intensities involved in these layers. We then analyse the sensitivity of this nominal model to specific parameters, including the initial temperature at the CMB, mantle convection parameterization, the composition of the BMO and the radiogenic content of the planet. We also investigate the influence of the thermal and electrical conductivities on the evolution of the planet, by constraining the existence and efficiency of dynamos hosted in the BMO and the core.

2. Model

We model the structural, thermal, buoyancy and magnetic evolution of an Earth-like planet with a mass $M_P = 5.972 \times 10^{24}$ kg and a core mass fraction CMF = 0.32. The variables of the model are summarized in Table 1 and the parameters are defined in Tables S1-S8.

We adopt the following workflow (Fig. 1). First, we pre-compute the internal structure over a wide range of imposed CMB temperatures (§2.1). This pre-computation is motivated because computation efficiency is predominantly limited by the integration of the internal structure. We then determine the structural and thermal evolution of the planet by computing the evolution of the temperature at the CMB with an energy budget (§2.2). Next, we determine the buoyancy profile evolution of the planet by computing buoyancy sources and sinks in the BMO and the core, *i.e.* the thermocompositional convective stability of both layers, including potential stably-stratified layers (§2.3). Finally, we obtain the magnetic evolution of the planet by computing entropy budgets, magnetic Reynolds numbers, and field intensities in the potential dynamo layers, *i.e.* the BMO and the outer core (§2.4).

The model is parameterized to generate an Earth-like evolution converging toward a structure similar to the Earth at present time, including properties such as the inner core radius, temperatures at the CMB and at the ICB, heat flows at the CMB and at the surface, and the surface magnetic field.

2.1. Structural evolution

We model a differentiated spherically symmetric Earth-like planet with a silicate mantle overlying a metal core (Fig. 2). We first define a reference structure with a solid MgSiO₃ mantle and a Fe core (§2.1.1). The mantle includes several solid phase transitions and the core may be liquid or solid. The reference structure is calculated for imposed temperatures at the CMB, with discrete integer degrees for $3000 \le T_{CMB} \le 8000$ K. The internal structure is then

Table 1 Summary of model variables. In the text, the physical quantities at the surface, at the top of the BMO, at the CMB, at the ICB, and at the center are respectively identified with the subscripts P, BMO, CMB, ICB and C. The subscripts m, b and c, oc and ic refer to the mantle, the BMO, the core, the outer core and the inner core. The subscripts R, S, G, C and C and C refer to radiogenic heating, secular cooling, gravitational energy, latent heat and adiabatic terms.

Symbol	Units	Definition
В	Т	Magnetic field intensity
b_{dip}	-	Internal to outer-boundary dipole ratio
<i>c</i> .	ppm	Radiogenic element concentration
C	kg.m ⁻³	Codensity
c_P	$J.kg^{-1}.K^{-1}$	Specific heat capacity
\dot{D}		Partition coefficient
E	$W.K^{-1}$	Rate of entropy production
\hat{E}	$J.mol^{-1}$	Molar internal energy
f	-	Inner-boundary mass anomaly fraction
F	$kg.s^{-1}$	Mass anomaly flow rate
\hat{F}	J.mol ⁻¹	Molar Helmholtz free energy
	m.s ⁻²	Gravity
g h	$W.kg^{-1}$	
	W.mg W.m ⁻¹ .K ⁻¹	Specific heat production rate
k		Thermal conductivity
K_S	Pa	Isentropic bulk modulus
K_T	Pa	Isothermal bulk modulus
L	m	Convective system length scale
m	kg	Mass distribution
M	kg	Mass
\mathcal{M}	$A.m^2$	True dipole moment
P	Pa	Pressure
q	$kg.m^{-2}.s^{-1}$	Mass anomaly flux
Q	W	Heat flow
r	m	Radius
R_m	_	Magnetic Reynolds number
Ro	_	Rossby number
\hat{S}	$J.K^{-1}.mol^{-1}$	Molar entropy
t	S	Time
T	K	Temperature
T_{I}	K	Liquidus temperature
u'	$m.s^{-1}$	Radial contraction velocity
U	m.s ⁻¹	Convective velocity
v	m.s ⁻¹	Flow velocity
V	m ³	Volume
Ŷ	m^3 .mol ⁻¹	Molar volume
•	K ⁻¹	
α	K	Thermal expansion coefficient
α_c	-	Compositional expansion coefficient
χ		Mole fraction
ϵ	$kg.m^{-3}.s^{-1}$	Volumetric buoyancy source
γ	_	Grüneisen parameter
K	$m^2.s^{-1}$	Thermal or mass diffusivity
μ	Pa.s	Dynamic viscosity
Ω	s^{-1}	Rotation rate
Φ	W	Convective power
ψ	$m^2.s^{-2}$	Gravitational potential
ρ	kg.m ⁻³	Density
σ	S.m ⁻¹	Electrical conductivity
Θ	K	Einstein temperature
ξ	_	Mass fraction
ζ	$J.mol^{-1}.K^{-2}$	Thermo-electronic heat capacity

modified by redefining the temperature profile of the mantle. First, we evaluate the possible formation of a liquid BMO, depending on the intersection between the temperature profile anchored at the imposed temperature of the CMB and the mantle liquidus (§2.1.2). Then, we redefine a consistent temperature profile in the solid upper mantle using a thermal boundary layer model (§2.1.3).

The following equations distinguish the BMO as a separate layer, but when the BMO is fully crystallized, the radius of the bottom of the mantle is the same as the CMB and BMO subscripts must be interpreted as CMB subscripts.

176

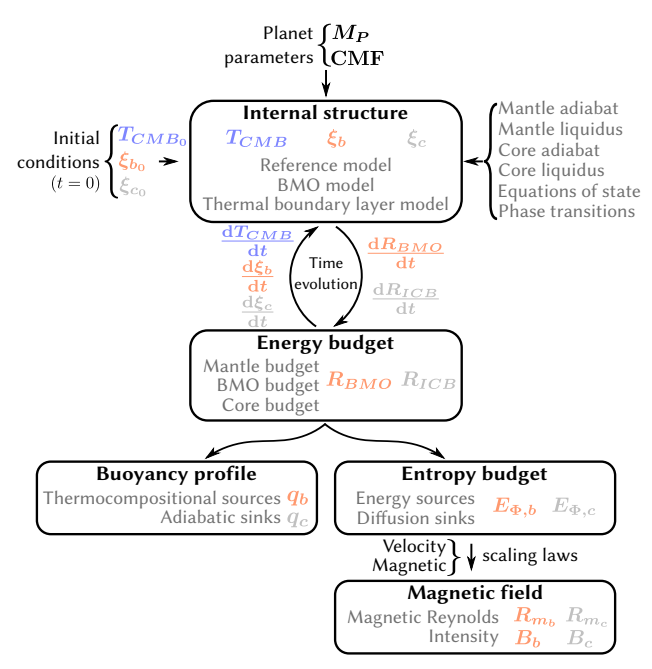


Figure 1: Description of the model workflow. The internal structure ($\S2.1$) and energy budgets ($\S2.2$) determine concomitantly the structural and thermal evolution of the planet over time. The convective stability of the BMO and the core is obtained at each time step by calculating buoyancy profiles ($\S2.3$). Similarly, the magnetic evolution is obtained by calculating entropy budgets ($\S2.4.1$), magnetic Reynolds numbers ($\S2.4.2$) and magnetic field intensities ($\S2.4.3$) at each time step. The physical quantities are defined in the text and Table 1.

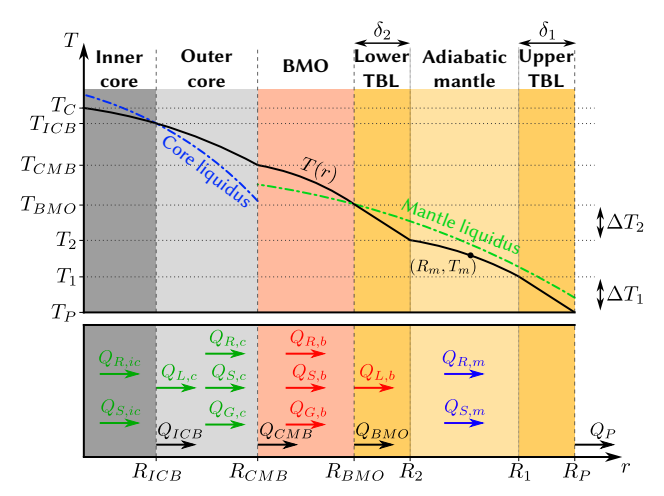


Figure 2: Definition of the layers and interfaces that can constitute the internal structure of the planet, *i.e.* a solid mantle, a liquid BMO, a liquid outer core and a solid inner core. The mantle is divided into an adiabatic section located between two thermal boundary layers (TBL). The extents of the BMO and the outer core are determined by the intersection of the adiabatic temperature profile anchored at the CMB and the appropriate liquidus. The arrows depict the heat flows Q involved in the energy budget. The radiogenic heating, secular cooling, gravitational energy and latent heat terms are denoted with the subscripts R, S, G and L.

- 180 Similarly, the notation distinguishes an inner core. However, if the core is fully molten, the radius at the bottom of the
- core is zero and ICB subscripts must be interpreted as C subscripts.

2.1.1. Reference model

Our reference structural model uses Boujibar et al. (2020), which is based on (Valencia et al., 2006; Seager et al., 183 2007; Driscoll and Olson, 2011). We obtain the mass distribution m, gravity g, pressure P and density ρ as a function of 184 radius r by integrating a continuity equation, a Poisson's equation, a hydrostatic equilibrium equation, and an Adams-185 Williamson equation 186

$$\frac{\mathrm{d}m}{\mathrm{d}r} = 4\pi r^2 \rho,\tag{2}$$

$$\frac{dm}{dr} = 4\pi r^2 \rho,$$

$$\frac{dg}{dr} = 4\pi G \rho - 2G \frac{m}{r^3},$$

$$\frac{dP}{dr} = -\rho g,$$
(2)

$$\frac{\mathrm{d}P}{\mathrm{d}r} = -\rho g,\tag{4}$$

$$\frac{\mathrm{d}\rho}{\mathrm{d}r} = -\frac{\rho^2 g}{K_S},\tag{5}$$

where G is the gravitational constant. The isentropic bulk modulus K_S depends on the temperature T, the thermal 187 expansivity α and the Grüneisen parameter γ 188

$$K_{S} = K_{T} \left(1 + \alpha \gamma T \right). \tag{6}$$

The isothermal bulk modulus K_T is defined using a third order Vinet-Rydberg (Vinet et al., 1989) equation of state 189 (EOS), defined in Appendix A (Eq. 57-59). We also use an adiabatic temperature profile in both the mantle and the 190 core, with a corresponding temperature gradient defined as 191

$$\frac{\mathrm{d}T}{\mathrm{d}r} = -\frac{\rho g \gamma}{K_s} T. \tag{7}$$

Although this is justifiable for the outer core and mantle, we expect a conductive inner core with a different temperature 192 profile. 193

We consider up to three phases in the solid mantle with peridotite (Pd), perovskite (Pv) and post-perovskite (pPv) (Boujibar et al., 2020). The phase boundaries are parameterized with

$$P = P_c + \gamma_c (T - T_c) \tag{8}$$

where P_c , T_c and γ_c are a reference pressure, temperature and a Clapeyron slope, defined in Table S3. We also define the core liquidus T_l (Stixrude, 2014; Boujibar et al., 2020) using a Simon-Glatzel equation (Simon and Glatzel, 1929)

$$T_l = T_{l_0} \left(\frac{P - P_{l_0}}{a_l} + 1 \right)^{b_l},\tag{9}$$

where T_{l_0} , P_{l_0} , a_l and b_l are a reference temperature, pressure and two composition-related parameters, defined in Table S4. To account for the depression of the liquidus from light elements, we multiply Eq. 9 by $\left[1 - \ln(1 - \chi_{c_l})\right]^{-1}$, where $\chi_{c_l} = 0.13$ is the fixed mole fraction of light elements (Boujibar et al., 2020). We do not consider a direct influence of the changing light element content on the core liquidus.

We determine the reference profile by integrating Eq. 2-7, together with Eq. 57-59, from the surface, at $r = R_P$, toward the center of the planet (Boujibar et al., 2020). The surface boundary conditions are

$$m_P = M_P, g_P = \frac{GM_P}{R_P^2}, P_P = 1.013 \times 10^5 \text{ Pa}, \rho_P = 3226 \text{ kg.m}^{-3}, T_P = 300 \text{ K}.$$
 (10)

The density jumps that occur in the mantle upon phase transitions, at the CMB, and at the ICB upon crystallization of the inner core are calculated assuming continuity of the isothermal bulk modulus (Eq. 57).

The mantle temperature profile of the reference model is adiabatic and anchored at the surface temperature, i.e. 206 using $T(R_P) = T_P$ as a boundary condition. This approximation allows us to precompute the internal structure as it does not require modeling the temperature profile of the mantle. In contrast, using a thermal boundary layer model in 208 the integration of the internal structure would require to calculate concomitantly the thermal evolution of the planet to 209 determine the depth of the mantle, the thickness of the boundary layers and the temperature drop in these layers. This 210 approximation is justified because temperature is mostly involved in the integration of the internal structure through 211 Eq. 6, where $\alpha \gamma T \simeq 3 \times 10^{-2} \ll 1$. Furthermore, temperature has only a weak influence on solid phase transitions 212 in the mantle because of the small Clapeyron slopes (Boujibar et al., 2020). As an example, increasing T_P by 2000 K 213 would change the density profile of the mantle by 0.6% on average. 214

The core temperature profile is also adiabatic but is anchored at the imposed CMB temperature T_{CMB} , *i.e.* the boundary condition is $T(R_{CMB}) = T_{CMB}$ (Boujibar et al., 2020). This is inaccurate for the inner core which is conductive. However, the influence on the position of the ICB is relatively weak since the adiabatic profile of the outer core is anchored at the CMB.

Since we impose the planet mass, the reference model is sensitive to the exact radius of the planet. We search for the value of R_P that gives a solution where mass and gravity go to zero at the center and where the pressure, density and temperature remain smooth and finite (Driscoll and Olson, 2011). This optimization is parameterized to give a typical error of 1 km on R_P . Variations of R_P too far from the optimal value may cause the solution to diverge close to the center (e.g. Eq. 3).

2.1.2. Basal magma ocean model

202

203

215

216

217

218

219

220

221

222

223

In our model, we follow Blanc et al. (2020), assuming that a BMO may exist (i) if the slope of the BMO adiabatic temperature profile is steeper than that of the mantle liquidus and (ii) if the temperature is larger than the liquidus at

the CMB. The BMO then extends from the CMB to the intersection between the BMO adiabat and the mantle liquidus (Fig. 2). This neglects the role of density contrasts between melt and crystals on the evolution of the BMO (Boukaré et al., 2015; Caracas et al., 2019; Nabiei et al., 2021).

The BMO adiabatic temperature profile, anchored at the CMB, is defined by

230

$$T(r) = T_{CMB} \exp\left(\int_{\rho_{CMB}^+}^{\rho(r)} \frac{\gamma_b}{\rho'} d\rho'\right),\tag{11}$$

where γ_b is an effective thermal Grüneisen parameter and ρ_{CMB}^+ is the mantle density at the CMB. The density profile used in Eq. 11 is a linear fit of the reference density profile obtained in the solid mantle. This facilitates eliminating 232 density jumps that might occur from solid phase transitions in the mantle from the BMO adiabat. As a result, the BMO 233 density profile is based on that of the solid mantle in the reference model at the same depth. It follows that the mass 234 distribution, gravity, and pressure of the BMO are also set to the value of the reference profile. As such, we neglect the 235 influence of changes in density caused by melting and variations in composition on the adiabatic temperature profile of 236 the BMO and on the mass distribution, gravity, and pressure profiles of the planet. We therefore do not self-consistently 237 integrate the planet structure with the BMO. Determining such a self-consistent profile would require integrating Eq. 238 2-7 from the surface, using the appropriate EOS for the BMO, and concomitantly calculating the thermal evolution of 239 the planet to determine the BMO thickness. 240

We determine the thermodynamics quantities of the BMO from the molar Helmholtz free energy \hat{F}_b of an effective EOS (Appendix B). Hereafter, the thermodynamic quantities commonly known as extensive, including free energy and volume, are defined for a mole of matter and are thus actually intensive molar quantities, denoted with a hat. The free energy \hat{F}_b corresponds to an ideal mixing model between MgSiO₃ and FeO

$$\hat{F}_b = \hat{F}_{\text{MoSiO}_2} + (\hat{F}_{\text{FeO}} - \hat{F}_{\text{MoSiO}_2})\chi_b,\tag{12}$$

where χ_b is the mole fraction of FeO in the BMO. \hat{F}_{MgSiO_3} uses a generalized Rosenfeld-Tarazona EOS (Wolf and Bower, 2018) and \hat{F}_{FeO} uses a Vinet-Rydberg EOS with a thermal and an electronic contribution (Morard et al., 2022). This allows us to consider the progressive enrichment of the BMO in iron-rich oxides.

We derive the thermodynamic quantities of the BMO from \hat{F}_b . This includes the isothermal bulk modulus $K_T = \hat{V}(\partial^2 \hat{F}/\partial \hat{V}^2)_T$, the isentropic bulk modulus $K_S = K_T (1 + \alpha \gamma T)$, the heat capacity at constant volume

 $\hat{C}_V = -T(\partial^2 \hat{F}/\partial T^2)_{\hat{V}}$, the heat capacity at constant pressure $\hat{C}_P = \hat{C}_V (1 + \alpha \gamma T)$, and the thermal expansivity $\alpha = -1/K_T(\partial^2 \hat{F}/\partial \hat{V}\partial T)$. Since the internal structure is not integrated self-consistently with a BMO EOS, the density

at which the thermodynamics quantities are computed is underestimated due to a lack of iron in the reference profile.

We also derive the effective thermal Grüneisen parameter used in the adiabatic temperature profile (Eq. 11) from 253 \hat{F}_b , using $\gamma_b = \alpha \hat{V} K_S / \hat{C}_P$. However, unlike other thermodynamic quantities used in the energy, buoyancy and entropy 254 terms, γ_b is defined using fixed temperature and composition, corresponding respectively to the initial temperature 255 at the CMB and the initial composition of the BMO. As a result, the radial profile of the BMO adiabatic temperature 256 gradient is constant over time. This simplification is required to determine the thermal evolution of the BMO (see Eq. 22 257 in §2.2) assuming that a time-varying Grüneisen parameter has a negligible effect on the adiabatic gradient (Gubbins 258 et al., 2003). In our nominal model, the maximum value of the radially-averaged Grüneisen parameter computed a 259 posteriori using time-dependent temperature and composition is only 16.8% larger than the fixed value based on the 260 initial conditions. 261

The mantle liquidus also depends on the BMO composition and is expected to shift toward lower temperatures as the BMO is enriched in FeO (Boukaré et al., 2015; Ballmer et al., 2017; Blanc et al., 2020). We use a linear phase diagram between MgSiO₃ (Fei et al., 2021) and FeO (Morard et al., 2022). The BMO liquidus is therefore defined as

$$T_{l_b} = T_{l_{\text{MgSiO}_3}} + (T_{l_{\text{FeO}}} - T_{l_{\text{MgSiO}_3}})\xi_b, \tag{13}$$

where ξ_b is the mass fraction of FeO in the BMO. The two end-members are defined using Simon-Glatzel equations (Eq. 9). The liquidus parameters are defined in Table S4.

As with the Grüneisen parameter, the mantle liquidus is computed using the pressure profile of the reference model at initial time, neglecting the effects of temperature variation and inner core crystallization on reference model. This simplification is required to include the correction related to the compositional depression of the liquidus, computed at constant pressure, in the crystallization rate of the BMO (see Appendix D). In our nominal model, the maximum difference between the radially-averaged liquidus computed *a posteriori* using the time-dependent pressure profile of the reference model and the fixed pressure profile at initial time is only 0.02%.

2.1.3. Thermal boundary layer model

262

263

264

267

268

269

270

271

272

273

274

275

276

In the solid part of the mantle, we redefine the temperature profile using a thermal boundary layer model similar to Driscoll and Bercovici (2014), that includes two boundary layers (Fig. 2). Temperature differences across the upper and lower boundary layers are denoted by ΔT_1 and ΔT_2 , with T_1 and T_2 the temperatures at the bottom of the upper boundary layer and at the top of the lower boundary layer. The thicknesses of the boundary layers are denoted by δ_1 and δ_2 , with R_1 and R_2 the lower radius of the upper boundary layer and the upper radius of the lower boundary layer.

We assume an adiabatic temperature profile outside of the boundary layers, so that T_1 can be expressed as a function of an average mantle temperature T_m , giving

$$\Delta T_1 = T_1 - T_P = T_m \eta_1 - T_P,\tag{14}$$

where η_1 refers to the adiabatic temperature decrease from the average mantle temperature to the bottom of the upper boundary layer. Eq. 14 gives

$$\eta_1 = \exp\left(-\int_{\bar{R}_m}^{R_1} \frac{\rho g \gamma}{K_S} dr\right),\tag{15}$$

where \bar{R}_m is an average radius corresponding to the average mantle temperature. We assume that $\delta_1 \ll L_m$, where $L_m = R_P - R_{BMO}$ is the thickness of the mantle, which gives $R_1 \sim R_P$. Furthermore, we assume that \bar{R}_m and T_m depend respectively on the outer radius of the BMO R_{BMO} and on the temperature at the top of the BMO T_{BMO}

$$\begin{cases}
\bar{R}_m = \frac{R_{BMO} + R_P}{2} \\
T_m = \frac{T_{BMO} + T_P}{2}
\end{cases}$$
(16)

which allows us to write ΔT_1 as a function of quantities independent of the boundary layer model, *i.e.* R_{BMO} , T_{BMO} , R_P and T_P .

We determine the upper boundary layer thickness by assuming that the local Rayleigh number Ra_1 equals the free-slip critical value $Ra_{cr} = 660$ (Howard, 1966; Solomatov, 1995; Driscoll and Bercovici, 2014). This gives

$$Ra_1 = \frac{\rho_P \alpha_P g_P \Delta T_1 \delta_1^3}{\kappa_P \mu_P} = Ra_{cr},\tag{17}$$

where ρ_P , α_P , g_P , μ_P , $\kappa_P = k_P/(\rho_P c_{P_P})$, k_P and c_{P_P} are density, thermal expansivity, gravity, dynamic viscosity, thermal diffusivity, thermal conductivity and specific heat capacity at constant pressure at the surface of the planet.

We assume that these quantities vary negligibly within the thermal boundary layer in calculating δ_1 . We assume that the viscosity at the surface of the upper boundary layer is $\mu_P = \mu_m/f_\mu$, where μ_m is the viscosity of the mantle and $f_\mu = 10$ is an arbitrary factor (Driscoll and Bercovici, 2014). Following Driscoll and Bercovici (2014), the mantle viscosity is

$$\mu_m = \mu_{m_0} \exp\left(\frac{A_\mu}{R\bar{T}}\right). \tag{18}$$

where $\mu_{m_0}=1.1\times 10^{15}$ Pa.s is a reference viscosity, $A_{\mu}=3\times 10^5$ J.mol⁻¹ is an activation energy, and \bar{T} is the average temperature of the mantle assuming an adiabatic profile and $T(R_P)=T_P+\Delta T_1$. The parameters are defined in Table S6. The thermal conductivity at the surface k_P is calculated in Appendix C (van den Berg et al., 2010) using the pressure at the surface, a temperature equal to $T_P+\Delta T_1/2$ and thermodynamic quantities computed at the surface.

Using Eq. 17, we write a generalized expression of the upper boundary layer thickness by replacing the 1/3 exponent by a parameter β

$$\delta_1 = L_m \left(Ra_{cr} \frac{\kappa_P \mu_P}{\rho_P \alpha_P g_P \Delta T_1 L_m^3} \right)^{\beta}. \tag{19}$$

In this context, we can interpret the surface heat flow in term of a Nusselt number, *i.e.* the ratio between convective and conductive heat transfer (Driscoll and Bercovici, 2014). Ra_{cr} and β can therefore be interpreted as the prefactor and the exponent of the $Nu \propto Ra^{\beta}$ relationships (Solomatov, 1995; Schubert et al., 2001).

In the upper boundary layer $(R_1 \le r \le R_P)$, we use a linear temperature profile with a constant temperature gradient

$$\frac{\mathrm{d}T}{\mathrm{d}r} = -\frac{\Delta T_1}{\delta_1} \quad \text{with} \quad T(R_P) = T_P, \tag{20}$$

where ΔT_1 and δ_1 are respectively obtained from Eq. 14 and 19. In the convecting region of the mantle $(R_2 \le r < R_1)$,
we use an adiabatic temperature profile (Eq. 7) with $T(R_1) = T_1$, where T_1 is obtained from Eq. 20. In the lower
boundary layer $(R_{BMO} \le r < R_2)$, we use a linear temperature profile with a constant temperature gradient

$$\frac{dT}{dr} = -\frac{1}{4\pi R_{BMO}^2} \frac{1}{k_2} Q_{BMO} \quad \text{with} \quad T(R_{BMO}) = T_{BMO}, \tag{21}$$

where the thermal conductivity in the lower boundary layer k_2 is estimated in Appendix C (van den Berg et al., 2010), using the pressure at the interface with the BMO, a temperature that extends the adiabatic temperature profile defined in the convecting region of the mantle (Eq. 7) to R_{BMO} , and thermodynamic quantities computed at the bottom of the mantle. Since the heat flow Q_{BMO} at the top of the BMO is obtained from the energy budget (§2.2), we can therefore obtain concomitantly ΔT_2 and δ_2 by computing the intersection between the adiabatic temperature profile in the convecting mantle (Eq. 7) and the linear temperature profile in the lower boundary layer (Eq. 21).

2.2. Thermal evolution

316

317

318

The thermal evolution of the planet is obtained by computing the evolution of the internal structures to different thermal states (§2.1). We follow a method initially developed for the Earth's core (Gubbins et al., 2003, 2004), and

later adapted for the BMO (Labrosse et al., 2007; Blanc et al., 2020; O'Rourke, 2020), to obtain the time evolution of
the temperature at the CMB with coupled energy budgets of the solid mantle (§2.2.1), BMO (§2.2.2) and core (§2.2.3).

In the energy budgets, we assume that the BMO and the core are adiabatic and well-mixed by convection (Gubbins
et al., 2003, 2004). In the BMO, this assumption becomes invalid when the melt fraction decreases below 40%
(Solomatov and Stevenson, 1993; Lejeune and Richet, 1995), which means that the dynamics of multi-phase flows
beyond the rheological transition should be considered (Boukaré and Ricard, 2017). If the thermodynamic quantities
of the BMO and the core vary slowly over time, in particular the Grüneisen parameter, the adiabatic temperature profiles
allows the following simplification (Gubbins et al., 2003),

$$\frac{\mathrm{D}T}{\mathrm{D}t} = \frac{T}{T_{CMB}} \frac{\mathrm{d}T_{CMB}}{\mathrm{d}t},\tag{22}$$

327 where

330

331

$$\frac{\mathbf{D}_{\bullet}}{\mathbf{D}t} = \frac{\partial_{\bullet}}{\partial t} + \mathbf{u} \cdot \nabla_{\bullet} \tag{23}$$

is a Lagrangian derivative accounting for the effect of the thermal contraction. \mathbf{u} is the slow radial velocity of contraction, in the BMO or the core.

2.2.1. Energy budget of the mantle

For the mantle, we write the energy budget as

$$Q_P = Q_{Rm} + Q_{Sm} + Q_{BMO}, (24)$$

where Q_P is the heat flow at the surface of the planet (expressed in W), $Q_{R,m}$ is the radiogenic heating in the mantle, $Q_{S,m}$ is the secular cooling of the mantle and Q_{BMO} is the heat flow at the top of the BMO (Appendix E).

The surface heat flow is expressed as the heat flow through the upper boundary layer of the solid mantle (Driscoll and Bercovici, 2014)

$$Q_P = 4\pi R_P^2 k_1 \frac{\Delta T_1}{\delta_1},\tag{25}$$

where the thermal conductivity in the upper boundary layer k_1 is estimated in Appendix C (van den Berg et al., 2010), using pressure, temperature and thermodynamic quantities averaged over the upper boundary layer. In addition, ΔT_1 and δ_1 are respectively obtained from Eq. 14 and 19. The radiogenic heating $Q_{R,m}$ (Eq. 82) is integrated over the volume of the mantle. We assume an Earth-like radiogenic content where ²³⁸U, ²³⁵U, ²³²Th and ⁴⁰K are the only isotopes contributing (Jaupart et al., 2015). We simplify the separate contribution of each radioisotope into a unique parameter, equivalent to an effective concentration, defined as the mantle fraction $f_h = 0.58$ of bulk silicate Earth (BSE) radiogenic production. This radiogenic term is independent of the CMB cooling rate. In contrast, the secular cooling $Q_{S,m}$ (Eq. 84) can be expressed as a function of the CMB cooling rate using the adiabatic profile simplification (Eq. 22) in the BMO.

2.2.2. Energy budget of the basal magma ocean

345

346

351

352

353

354

355

356

357

358

350

360

In the BMO, we write the energy budget as

$$Q_{BMO} = Q_{R,b} + Q_{S,b} + Q_{G,b} + Q_{L,b} + Q_{CMB}$$
(26)

where $Q_{R,b}$ is the heat flow corresponding to radiogenic heating in the BMO, $Q_{S,b}$ is the BMO secular cooling, $Q_{G,b}$ is a gravitational energy due to the release of FeO upon crystallization, $Q_{L,b}$ is the corresponding latent heat and Q_{CMB} is the heat flow at the CMB (Appendix E). We neglect the heat flows associated with the heat of reaction, pressure heating and pressure effects on freezing (Blanc et al., 2020; O'Rourke, 2020).

We integrate the radiogenic heating $Q_{R,b}$ (Eq. 87) over the BMO volume using the same specific heat production rate as in the mantle, thereby assuming homogeneous radiogenic heating in the BMO and the mantle. As with the mantle, this term is independent of the CMB cooling rate. In contrast, the secular cooling term $Q_{S,b}$ (Eq. 88) can be directly expressed as a function of the CMB cooling rate using the adiabatic profile (Eq. 22) in the BMO. In addition, the gravitational energy term $Q_{G,b}$ (Eq. 89), which is actually a compositional energy due to the release of FeO (Labrosse, 2003) upon crystallization, depends on the rate of release of FeO, which can be expressed as a function of the BMO crystallization rate. Finally, the latent heat term $Q_{L,b}$ (Eq. 91) is proportional to the BMO crystallization rate.

The secular cooling $Q_{S,b}$, the gravitational energy $Q_{G,b}$ and the latent heat $Q_{L,b}$ terms can therefore be expressed as a function of the cooling rate at the CMB. If the BMO is well-mixed, the rate of release of FeO into the BMO is proportional to the crystallization rate of the BMO (Gubbins et al., 2004; Blanc et al., 2020), with

$$\frac{\mathrm{D}\xi_b}{\mathrm{D}t} = -\frac{4\pi R_{BMO}^2 \rho_{BMO}^- \Delta \xi_{BMO}}{M_b} \frac{\mathrm{d}R_{BMO}}{\mathrm{d}t} = C_{\xi_b} \frac{\mathrm{d}R_{BMO}}{\mathrm{d}t},\tag{27}$$

where ρ_{BMO}^- is the density of the BMO at the solid mantle interface, M_b is the mass of the BMO, and C_{ξ_b} is the proportionality factor. The composition change across the interface is

$$\Delta \xi_{BMO} = \xi_b (1 - D_{BMO}),\tag{28}$$

where D_{BMO} is the iron partition coefficient between liquid and solid.

In order to obtain an Earth-like nominal model with no BMO at present time, we set $D_{BMO}=0.85$. This value is larger than experimental measurements of the iron partition coefficient, which gives values between $D_{BMO}=0.1-0.2$ (Nomura et al., 2011; Tateno et al., 2014) and $D_{BMO}=0.5-0.6$ (Andrault et al., 2012). However, this discrepancy might be explained by the linear phase diagram assumption (Eq. 13). Using a realistic crystallization sequence in the MgO – FeO – SiO₂ system at the pressure and temperature conditions of the BMO (Boukaré et al., 2015; Nabiei et al., 2021) might reconcile an Earth-like evolution with lower values of the partition coefficient.

Adapting the results of Gubbins et al. (2003) to the BMO, in conjunction with the findings of Blanc et al. (2020),
we show that the BMO crystallization rate is proportional to the CMB cooling rate, with a correction corresponding
to the depression of the liquidus as the BMO is enriched in iron

$$\frac{\mathrm{d}R_{BMO}}{\mathrm{d}t} = C_{R_b} \frac{\mathrm{d}T_{CMB}}{\mathrm{d}t},\tag{29}$$

where C_{R_h} is the proportionality factor (see Appendix D).

2.2.3. Energy budget of the core

375

382

383

384

385

In the core, we write the energy budget as

$$Q_{CMR} = Q_{Rc} + Q_{Sc} + Q_{Gc} + Q_{Lc} + Q_{ICR}, (30)$$

where $Q_{R,c}$ is the heat flow corresponding to radiogenic heating in the outer core, $Q_{S,c}$ is the outer core secular cooling, $Q_{G,c}$ is the gravitational energy due to the release of light elements upon crystallization, $Q_{L,c}$ is the corresponding latent heat and Q_{ICB} is the heat flow at the ICB. The heat flow at the ICB is

$$Q_{ICB} = Q_{R,ic} + Q_{S,ic},\tag{31}$$

where $Q_{R,ic}$ and $Q_{S,ic}$ are the radiogenic heating and the secular cooling of the inner core, respectively (see Appendix E). As with the BMO, we neglect the heat flows associated with the heat of reaction, pressure heating and pressure effects on freezing (Gubbins et al., 2003, 2004).

The radiogenic heating terms $Q_{R,c}$ and $Q_{R,ic}$ (Eq. 92 and 98) are respectively integrated over the volume of the outer and inner core. We assume that 40 K is the only radiogenic element contributing to the radiogenic heating and we choose a moderate potassium concentration in the core, *i.e.* $c_c = 20$ ppm (Hirose et al., 2013; Labrosse, 2015). We therefore assume that radiogenic production is homogeneous in the inner and outer core. As with the mantle and

the BMO, these terms are independent of the cooling rate at the CMB. In contrast, the secular cooling terms $Q_{S,c}$ and $Q_{S,ic}$ (Eq. 94 and 99) can be expressed as a function of the CMB cooling rate using Eq. 22 in the outer core, and an infinite thermal conductivity, *i.e.* an isothermal profile where the temperature is equal to the liquidus (O'Rourke et al., 2018), in the inner core. The gravitational energy term $Q_{G,c}$ (Eq. 95) depends on the rate of release of light elements (Labrosse, 2003), which can be expressed as a function of the crystallization rate of the inner core. Finally, the latent heat term $Q_{L,c}$ (Eq. 97) is proportional to the crystallization rate of the inner core.

As with the BMO, the secular cooling $Q_{S,c}$, the gravitational energy $Q_{G,c}$ and the latent heat $Q_{L,c}$ terms can therefore be expressed as a function of the cooling rate at the CMB. If the outer core is well-mixed, the rate of release of the light elements into the outer core is proportional to the crystallization rate of the core (Gubbins et al., 2004), with

$$\frac{\mathrm{D}\xi_c}{\mathrm{D}t} = \frac{4\pi R_{ICB}^2 \rho_{ICB}^+ \xi_c}{M_{oc}} \frac{\mathrm{d}R_{ICB}}{\mathrm{d}t} = C_{\xi_c} \frac{\mathrm{d}R_{ICB}}{\mathrm{d}t},\tag{32}$$

where ξ_c is the mass fraction of light elements in the outer core, ρ_{ICB}^+ is the density of the outer core at the ICB, M_{oc} is the mass of the outer core, and C_{ξ_c} is the proportionality factor. Here we assume that there are no light elements in the inner core, *i.e.* $\Delta \xi_{ICB} = \xi_c$ (Gubbins et al., 2004).

Following Gubbins et al. (2003), the crystallization rate of the core is proportional to the cooling rate at the CMB

$$\frac{\mathrm{d}R_{ICB}}{\mathrm{d}t} = C_{R_c} \frac{\mathrm{d}T_{CMB}}{\mathrm{d}t},\tag{33}$$

where C_{R_c} is the proportionality factor (see Appendix D).

2.2.4. Integration of the initial value problem

399

Using the relationships between the release rates, the crystallization rates and the cooling rates in the BMO (Eq. 27 and 29) and the core (Eq. 32 and 33), we can write the secular cooling terms ($Q_{S,b}$, $Q_{S,c}$, $Q_{S,ic}$), the gravitational energy terms ($Q_{G,b}$, $Q_{G,c}$) and the latent heat terms ($Q_{L,b}$, $Q_{L,b}$) as a function of the cooling rate at the CMB. In addition, since we can write explicitly the heat flow at the surface (Q_P) and the radiogenic heating terms ($Q_{R,b}$, $Q_{R,c}$, $Q_{R,c}$) as a function of time, we obtain

$$Q_{P} - Q_{R,m} - Q_{R,b} - Q_{R,c} - Q_{R,ic} = \left[\tilde{Q}_{S,m} + \tilde{Q}_{S,b} + \tilde{Q}_{S,c} + \tilde{Q}_{S,ic} + \tilde{Q}_{G,b} + \tilde{Q}_{G,c} + \tilde{Q}_{L,b} + \tilde{Q}_{L,c}\right] \frac{dT_{CMB}}{dt}, (34)$$

where the functions $\tilde{Q}_X(r) = Q_X(r,t) \left(\frac{\mathrm{d}T_{CMB}(t)}{\mathrm{d}t} \right)^{-1}$ only depend on r.

We obtain the thermal evolution of the planet by solving numerically Eq. 34 as an initial value problem with an explicit Runge-Kutta method of order 5. Since the internal structure is pre-computed at discrete integer degrees, each integration of Eq. 34 uses the structure calculated at the closest available temperature to calculate the terms involved in the energy budget.

We determine the initial CMB temperature $T_{CMB_0} = 5710$ K, and therefore the initial BMO thickness $L_{b_0} = 952$ km, by assessing the temperature at which the BMO adiabat (Eq. 11) is tangent to the mantle liquidus (Eq. 13), both computed at the initial composition. The initial conditions for the composition of the BMO and the core are $\xi_{b_0} = 16$ wt% (Caracas et al., 2019; Blanc et al., 2020) and $\xi_{c_0} = 5.6$ wt% (Masters and Gubbins, 2003; Gubbins et al., 2013; Labrosse, 2014, 2015).

In our model, both the thickness and crystallization rate of the BMO tend toward zero (e.g. Fig. 4). As a result, 417 the BMO becomes very thin and never completely solidifies. This asymptotic behavior, similar to the exponential 418 decay of the BMO thickness obtained by Labrosse et al. (2007), arises from several assumptions used in our model. 419 In particular, we assume that the BMO is adiabatic and well-mixed, and that crystallization follows a linear phase 420 diagram. However, in reality, the BMO is expected to follow a more complex crystallization sequence, leading to a 421 rheological transition and eventual solidification. Since these features are not explicitly considered in our model, we 422 instead employ a heuristic criterion to determine the crystallization time of the BMO. We define the BMO as fully 423 solidified when the temperature difference across it reaches 1 K, which corresponds to a 1.4 km BMO. This choice 424 allows to obtain an Earth-like nominal model, where the BMO is either fully crystallized at present time, or where the BMO is sufficiently small for solid mantle convection to concentrate the remaining liquid into melt pockets (Labrosse et al., 2007; O'Rourke, 2020). This means that the solidification of the BMO is not self-consistently determined by the 427 model, since the choice of this criterion directly influences the crystallization timescale. 428

2.3. Buoyancy evolution

408

409

410

411

412

413

414

415

416

429

430

432

433

The competition between thermocompositional sources (2.3.1) and adiabatic sinks (2.3.2) of buoyancy determines the convective stability (2.3.3) of the BMO and the core. Within the Boussinesq approximation, thermal and compositional buoyancy sources can be combined into a codensity (density anomaly) field C, defined by Braginsky and Roberts (1995) as

$$C = \bar{\alpha}\bar{\rho}T' + \alpha_c\bar{\rho}\xi',\tag{35}$$

where the temperature T' and the mass fraction ξ' are deviations from an adiabatic well-mixed reference state, $\bar{\rho}$ is the average density of the layer (BMO or core), $\bar{\alpha}$ is the average thermal expansion coefficient and α_c is a compositional expansion coefficient (Eq. 90 and 96). As a result, we assume that the temperature and composition fields have the same

effective diffusivity κ , neglecting double-diffusivity effects. We can then write a single codensity transport equation

$$\frac{\partial C}{\partial t} + \mathbf{v} \cdot \nabla C = \kappa \nabla^2 C + \epsilon,\tag{36}$$

where ${\bf v}$ is the local flow velocity and ϵ corresponds to the volumetric sources of buoyancy. The total codensity can be separated into a steady background profile $C_0(r)$, with superimposed fluctuations $C'(r,\theta,\varphi,t)$. Eq. 36 can then be decomposed into a conduction equation

$$0 = \kappa \nabla^2 C_0 + \epsilon, \tag{37}$$

and a perturbation equation

$$\frac{\partial C'}{\partial t} + \mathbf{v} \cdot \nabla (C_0 + C') = \kappa \nabla^2 C'. \tag{38}$$

2.3.1. Thermal and compositional sources

The conduction equation (Eq. 37), which includes the volumetric sources of buoyancy, allows us to compare the relative influence of thermal and compositional buoyancy sources on convection (Davies and Gubbins, 2011) in both the BMO and the core. The thermal buoyancy sources are the heat sources in the energy budget. This includes radiogenic heating ($q_{R,b}$ and $q_{R,c}$) (Eq. 102), secular cooling ($q_{S,b}$ and $q_{S,c}$) (Eq. 105), viscous or ohmic dissipation of the motion produced by gravitational redistribution of FeO ($q_{G,b}$) or light elements ($q_{G,c}$) (Eq. 108), latent heat released at the ICB ($q_{L,c}$) (Eq. 111), and heat sources at the CMB (q_{CMB}) or ICB (q_{ICB}) (Eq. 114). The compositional buoyancy sources correspond to the progressive release of dense FeO in the BMO ($q_{C,b}$), or light elements in the core ($q_{C,c}$) (Eq. 117). Since the layers are well-mixed, these compositional terms behave as equivalent uniform compositional sinks.

For each buoyancy source, we solve separate conduction equations using the appropriate volumetric source term (Appendix F). For thermal sources, volumetric source terms are obtained by multiplying the corresponding volumetric heat source by $\bar{\alpha}/\bar{c}_P$, where \bar{c}_P is the average value of the specific heat capacity at constant pressure within the BMO or the core. For compositional sources, volumetric source terms are obtained by multiplying the rate of release of FeO, or light elements, by $\bar{\rho}\alpha_c$. This gives a conductive codensity gradient that is functionally equivalent to the cotemperature gradients of Davies and Gubbins (2011), namely

$$C_0'(r) = -\frac{1}{\kappa_T} \frac{1}{r^2} \int_{r_0}^r x^2 \epsilon(x) dx + \frac{A}{r^2},$$
(39)

where A is an integration constant, κ_T is a turbulent, not molecular, diffusivity (Gubbins et al., 2015), and r_0 is a reference radius.

For each buoyancy source, the integration constant is determined using a boundary condition corresponding to a
mass anomaly flux at the appropriate interface (Appendix F) (Gubbins et al., 2015). The mass anomaly fluxes, defined
as

$$q(r) = \kappa_T C_0'(r),\tag{40}$$

correspond to the thermal or chemical anomaly that passes through a unit of surface area per unit time (Aubert et al., 2009), and are expressed in kg.m⁻².s⁻¹. The buoyancy sources act as negative, destabilizing codensity gradients and mass anomaly fluxes. For thermal sources, the mass anomaly fluxes are obtained by multiplying the corresponding heat flux (expressed in W.m⁻²), which corresponds to a heat flow (expressed in W) per unit of surface at the appropriate interface, by $\bar{\alpha}/\bar{c}_P$. For compositional sources, the mass anomaly fluxes at the CMB are zero because we neglect exchanges between the BMO and the core, as well as thermodiffusion and barodiffusion, which correspond to negligible buoyancy sinks (Davies and Gubbins, 2011).

2.3.2. Equivalent adiabatic sinks

470

471

472

473

474

The buoyancy profile also includes sinks that contribute to stabilize the convecting layers. Thermal conduction corresponds to the main equivalent buoyancy sink in the system. It removes heat from convection and acts as a positive and stabilizing codensity gradient and mass anomaly flux. The adiabatic codensity gradients are obtained by multiplying the adiabatic temperature gradient by $\bar{\rho}\bar{\alpha}$ (Eq. 35). The corresponding mass anomaly fluxes of the BMO and the core are then

$$\begin{cases} q_{A,b} = -\kappa_{m_b} \bar{\rho} \bar{\alpha} \frac{\mathrm{d}T}{\mathrm{d}r}, \\ q_{A,c} = -\kappa_{m_c} \bar{\rho} \bar{\alpha} \frac{\mathrm{d}T}{\mathrm{d}r}, \end{cases}$$

$$\tag{41}$$

where κ_{m_b} and κ_{m_c} are molecular diffusivities and not turbulent ones (Gubbins et al., 2015). These diffusivities can be expressed as a function of the thermal conductivities in the BMO k_b and the core k_c , with $\kappa_m = k/(\bar{\rho}\bar{c}_P)$. However, the thermal conductivities, which depend on pressure, temperature and composition, remain uncertain, both in the BMO (Holmström et al., 2018; Soubiran and Militzer, 2018; Stixrude et al., 2020) or in the core (Ohta et al., 2016; Basu et al., 2020; Pozzo et al., 2022). In our model, we therefore set conservative values with $k_b = 8 \text{ W.m}^{-1}.\text{K}^{-1}$ and $k_c = 70 \text{ W.m}^{-1}.\text{K}^{-1}$.

2.3.3. Convective stability criterion

487

496

500

The total mass anomaly flux, which corresponds to the sum of the mass anomaly fluxes associated with the thermocompositional sources and sinks of buoyancy, can be used to determine the local convective stability of the BMO and the core (Davies and Gubbins, 2011; Pozzo et al., 2012; Gubbins et al., 2015). The reason for using mass anomaly fluxes instead of codensity gradients is that the destabilizing codensity gradients are associated with a turbulent diffusivity whereas the equivalent adiabatic flux uses a molecular diffusivity (Gubbins et al., 2015).

The total mass anomaly flux of the BMO and the core are therefore defined as

$$\begin{cases}
q_b = q_{R,b} + q_{S,b} + q_{G,b} + q_{L,b} + q_{CMB} + q_{A,b} \\
q_c = q_{R,c} + q_{S,c} + q_{G,c} + q_{L,c} + q_{ICB} + q_{A,c}
\end{cases}$$
(42)

The total mass anomaly flux can be used to determine the local convective stability of the layer and in particular the presence of stably-stratified layers. Convecting and stably-stratified regions are given by an equivalent Schwarzschild criterion

$$\begin{cases} q(r) < 0 & \text{if convecting} \\ q(r) \ge 0 & \text{if stable} \end{cases}$$
 (43)

The stability boundary is defined where the equivalent adiabatic mass anomaly flux is balanced by the destabilizing mass anomaly fluxes associated with the thermocompositional buoyancy sources. If the sum of the destabilizing mass anomaly fluxes is smaller, in magnitude, than the equivalent adiabatic mass anomaly flux, the BMO and the core may be partly or fully stably-stratified. This corresponds to destabilizing codensity profiles being less steep than the equivalent adiabatic profile.

The stably-stratified layers defined with Eq. 43 are not properly included in our thermal evolution model. In particular, we overestimate the secular cooling of these conductive layers assuming an adiabatic profile throughout the core. Considering such layers would require to compute the buoyancy profiles at every time step when integrating the energy budget.

2.4. Magnetic evolution

In this model, the magnetic evolution of the planet is obtained by assessing whether the potential dynamo layers, i.e. the BMO and the outer core, have (i) sufficient power to sustain a dynamo and (ii) a magnetic induction larger than magnetic diffusion. In practice, we first use entropy budgets (§2.4.1), initially developed for the Earth's core (Gubbins et al., 2003, 2004) and later adapted for the BMO (Blanc et al., 2020; O'Rourke, 2020), to assess the entropy criterion.

Then, we estimate the magnetic Reynolds number (§2.4.2) to assess the induction criterion. Finally, we estimate the intensity of the magnetic field (§2.4.3) powered in each layer.

2.4.1. Entropy budget

507

508

517

518

519

520

521

522

523

524

525

526

527

528

529

530

531

We write the entropy budget of the BMO and the core as

$$E_{R,b} + E_{S,b} + E_{G,b} + E_{L,b} + E_{CMB} = E_{k,b} + E_{\alpha,b} + E_{\Phi,b}, \tag{44}$$

$$E_{R,c} + E_{S,c} + E_{G,c} + E_{L,c} + E_{ICB} = E_{k,c} + E_{\alpha,c} + E_{\Phi,c}, \tag{45}$$

where all terms are rates of entropy production (Nimmo, 2015a), expressed in W.K⁻¹. The left-hand side of the 509 equations corresponds to source terms, including the entropy of radiogenic heating E_R (Eq. 118), the entropy of secular 510 cooling E_S (Eq. 119), the entropy of gravitational energy E_G due to the release of FeO and light elements (Eq. 120), the 511 entropy of latent heat E_L (Eq. 121), as well as the entropy E_{CMB} and E_{ICB} associated with the heat source at the CMB 512 and the ICB (Eq. 122). The right-hand side corresponds to sink terms, including the entropy of thermal diffusion E_k 513 (Eq. 123), the entropy of molecular diffusion E_{α} (Eq. 124) and the combined entropy of ohmic and viscous dissipation 514 E_{Φ} . We neglect entropy terms associated with the heat of reaction, pressure heating and pressure effects on freezing, 515 in both the BMO (Blanc et al., 2020; O'Rourke, 2020) and the core (Gubbins et al., 2003, 2004). 516

Each term can be written as the product of the corresponding heat flow and an efficiency factor, divided by an effective operating temperature (Appendix G). The efficiency factors correspond to the thermodynamic efficiency of the buoyancy sources. Buoyancy sources that are produced at the bottom of the layer are more efficient than buoyancy sources distributed throughout the layer.

The dissipation term E_{Φ} can be expressed as the sum of ohmic and viscous dissipation. Since E_{Φ} is the only unknown in the entropy budgets, we can obtain this term by subtracting the thermal and molecular diffusion terms from the source terms. In addition, we assume that the viscous dissipation term is negligible in comparison with the ohmic dissipation term in both the BMO (Blanc et al., 2020; O'Rourke, 2020) and the core (Aubert et al., 2009). E_{Φ} can thus be related to the gravitational energy that sustains convection (Buffett et al., 1996), which means that it corresponds to the energy fraction that contributes to generate a magnetic field. Therefore, E_{Φ} can be used as a first criterion for the operation of a dynamo in the BMO (Blanc et al., 2020) and the core (Davies, 2015; Greenwood et al., 2021; Driscoll and Davies, 2023). If $E_{\Phi} > 0$, the power available is sufficient to sustain a dynamo.

2.4.2. Magnetic Reynolds number

In addition to the entropy criterion, the magnetic Reynolds number has to exceed a critical value for magnetic induction to sufficiently overcome magnetic diffusion and a dynamo to operate continuously in the convecting layer.

The magnetic Reynolds numbers of the BMO and the core are defined as

$$\begin{cases}
R_{m_b} = U_b L_b \mu_0 \sigma_b \\
R_{m_c} = U_c L_c \mu_0 \sigma_c
\end{cases},$$
(46)

where U_b , L_b , σ_b and U_c , L_c , σ_c are respectively the characteristic convective velocity, the thickness and the electrical 533 conductivity of the BMO and the core. Using these definitions, a self-sustained magnetic field might be expected in the 534 respective layers if $R_m > 40$ (Christensen and Aubert, 2006). This critical value, obtained from magnetohydrodynamic 535 (MHD) simulations in the Earth's core, is not universal but is commonly used as a criterion for dynamo operation, so 536 we adopt it for both the BMO and the core, separately. Another condition, depending on the approximation of the 537 mean field equations and the interplay between the BMO and the core is the dynamo number (Ziegler and Stegman, 538 2013). However, we do not consider this criterion here. Electrical conductivities, like thermal conductivities, remain 539 uncertain, both in the BMO (Holmström et al., 2018; Soubiran and Militzer, 2018; Stixrude et al., 2020) and the core 540 (Ohta et al., 2016; Basu et al., 2020; Pozzo et al., 2022). We therefore set conservative values of $\sigma_b = 3 \times 10^4 \text{ S.m}^{-1}$ and $\sigma_c = 1 \times 10^6 \text{ S.m}^{-1}$. The convective velocities are obtained using scaling laws derived from MHD numerical simulations (Aubert et al., 543

The convective velocities are obtained using scaling laws derived from MHD numerical simulations (Aubert et al., 2009). The scaling laws relate the dimensionless convective velocity, *i.e.* a Rossby number Ro, to the total dissipation, *i.e.* a dimensionless convective power $\tilde{\Phi}$, determined from the entropy budgets by multiplying the dissipation term by an effective dissipation temperature (Appendix H). These scaling laws, initially developed for the Earth's core, may differ for the BMO since a silicate dynamo would operate in a thinner shell and have a larger Prandtl number. Nevertheless, we use the same scaling law in the BMO and the core, which gives

$$\left. \begin{array}{l} Ro_b = \frac{U_b}{L_b \Omega} \\ Ro_c = \frac{U_c}{L_c \Omega} \end{array} \right\} = c_U \tilde{\Phi}^{\alpha_U}, \tag{47}$$

where c_U and α_U are respectively the prefactor and exponent of the scaling law, obtained from a least-square fit on a set of dynamo simulations (Aubert et al., 2009), and Ω is the rotation rate of the planet. Since the evolution of the Earth's rotation rate over time remains uncertain (Touma and Wisdom, 1994; Daher et al., 2021), we choose a linear evolution of the length of day from 5 h (Canup and Asphaug, 2001; Cuk and Stewart, 2012) at t = 0 to one Earth day at t = 4.5 Gyr.

The exponents of the scaling laws can also be derived analytically from various force balance arguments (Christensen, 2010). In the mixing length theory (MLT) regime, the balance between the inertia term and the

buoyancy term in the momentum equation implies that the convective velocity scales as $\tilde{\Phi}^{1/3}$. In the Coriolis-InertiaArchimedean (CIA) regime, the balance between the Coriolis term, the inertia term and the buoyancy term implies that
the velocity scales as $\tilde{\Phi}^{2/5}$. Finally, in the Magnetic-Archimedean-Coriolis (MAC) regime, the balance between the
Lorentz force, the buoyancy force and the Coriolis force implies a $\tilde{\Phi}^{1/2}$ scaling. The prefactors of the scaling laws are
obtained using a least-square fit on the set of dynamo simulations of Aubert et al. (2009) (Appendix H). The scaling
law parameters are defined in Table S8.

2.4.3. Magnetic field intensity

562

The magnetic field of the BMO and the core are also obtained using scaling laws derived from MHD numerical simulations (Aubert et al., 2009). The scaling laws relate the dimensionless magnetic field \tilde{B} to the dimensionless convective power (Appendix H). As with the convective velocity, we use the same scaling law in the BMO and the core which gives

$$\left. \begin{array}{l} \tilde{B}_b = \frac{B_b}{\sqrt{\bar{\rho}_b \mu_0} \Omega L_b} \\ \tilde{B}_c = \frac{B_c}{\sqrt{\bar{\rho}_c \mu_0} \Omega L_c} \end{array} \right\} = c_B f_{\Omega}^{1/2} \tilde{\Phi}^{\alpha_B}, \tag{48}$$

where c_B and α_B are the prefactor and exponent of the scaling law, obtained from a least-square fit of dynamo simulations (Aubert et al., 2009). B_b , $\bar{\rho}_b$ and B_c , $\bar{\rho}_c$ are the internal magnetic field and average density of the BMO and the core, respectively. f_{Ω} is the ohmic dissipation fraction of the convective power. Following Aubert et al. (2009) for the core and O'Rourke (2020) for the BMO, we set $f_{\Omega} = 0.9$ in both layers. The exponents of the MLT, CIA and MAC balance are respectively 1/3, 3/10 and 1/4 (Christensen, 2010). The prefactors are also obtained using a least-square fit on the set of dynamo simulations of Aubert et al. (2009) (Appendix H). The scaling law parameters are defined in Table S8.

In order to obtain the surface magnetic field produced by the BMO and the core, we first determine the relative strength of the internal field in each layer and the dipole field at the outer boundary using a scaling law (Aubert et al., 2009)

$$\begin{cases} b_{dip,b} = c_{dip} \left(1 - \frac{R_{CMB}}{R_{BMO}} \right) \left(1 + f_b \right) \\ b_{dip,c} = c_{dip} \left(1 - \frac{R_{ICB}}{R_{CMB}} \right) \left(1 + f_c \right) \end{cases}$$

$$(49)$$

where f_b and f_c are the fraction of the mass anomaly flow rate produced at the inner boundary of the BMO and the core, and $c_{dip} = 7.3$ is a prefactor obtained from a least-square fit of dynamo simulations (Aubert et al., 2009). A mass anomaly flow rate (expressed in kg.s⁻¹), is the thermal, or chemical, anomaly passing through a surface area per unit

time and equals the mass anomaly flux integrated over a surface area. Fractions of the mass anomaly flow rate are defined as

$$\begin{cases} f_b = \frac{F_{CMB}}{F_{CMB} + F_{BMO}} \\ f_c = \frac{F_{ICB}}{F_{ICB} + F_{CMB}} \end{cases} , \tag{50}$$

where F_{ICB} , F_{CMB} and F_{BMO} are the mass anomaly flow rates at the ICB, the CMB and the top of the BMO. Then, we determine the true dipole moment of the BMO and the core with

$$\begin{cases} \mathcal{M}_{b} = \frac{4\pi R_{BMO}^{3}}{\sqrt{2}\mu_{0}} \frac{B_{b}}{b_{dip,b}} \\ \mathcal{M}_{c} = \frac{4\pi R_{CMB}^{3}}{\sqrt{2}\mu_{0}} \frac{B_{c}}{b_{dip,c}} \end{cases}, \tag{51}$$

and finally obtain the intensity of the magnetic field at the surface with

$$\begin{cases}
B_{P,b} = \frac{\mu_0}{4\pi R_P^3} \mathcal{M}_b \\
B_{P,c} = \frac{\mu_0}{4\pi R_P^3} \mathcal{M}_c
\end{cases}$$
(52)

3. Earth-like planet nominal evolution

Our nominal model uses the assumptions detailed in §2, together with the parameters defined in tables S1-S8, to determine the structural (3.1), thermal (3.2), buoyancy (3.3) and magnetic (3.4) evolution of the planet.

3.1. Structural evolution

588

589

590

591

593

596

597

598

Fig. 3 shows the time evolution of the density, gravity, pressure and temperature as a function of radius for the nominal model. The density profile of the BMO corresponds to a linear fit of the reference profile defined for the solid mantle, while the gravity and pressure profiles of the BMO are identical to the reference profile (§2.1.2). In the supplementary material, we provide the time evolution of the Grüneisen parameter, thermal expansion coefficient, isothermal bulk modulus and specific heat capacity at constant pressure for the nominal model (Fig. S1).

The density profile shows a density jump corresponding to the CMB at approximately 3140 km under the surface the planet (Fig. 3a). In the mantle, the density profile also shows two density jumps at approximately 810 km and 2600 km. They correspond respectively to the peridotite to perovskite and to the perovskite to post-perovskite solid phase transitions. In the core, after 3.8 Gyr, the density profile shows density jumps corresponding to the inner core nucleation. These jumps are also visible as slope discontinuities on the gravity (Fig. 3b) and pressure (Fig. 3c) profiles, in particular at the CMB. Since the integration of the internal structure is conducted using an imposed planet mass,

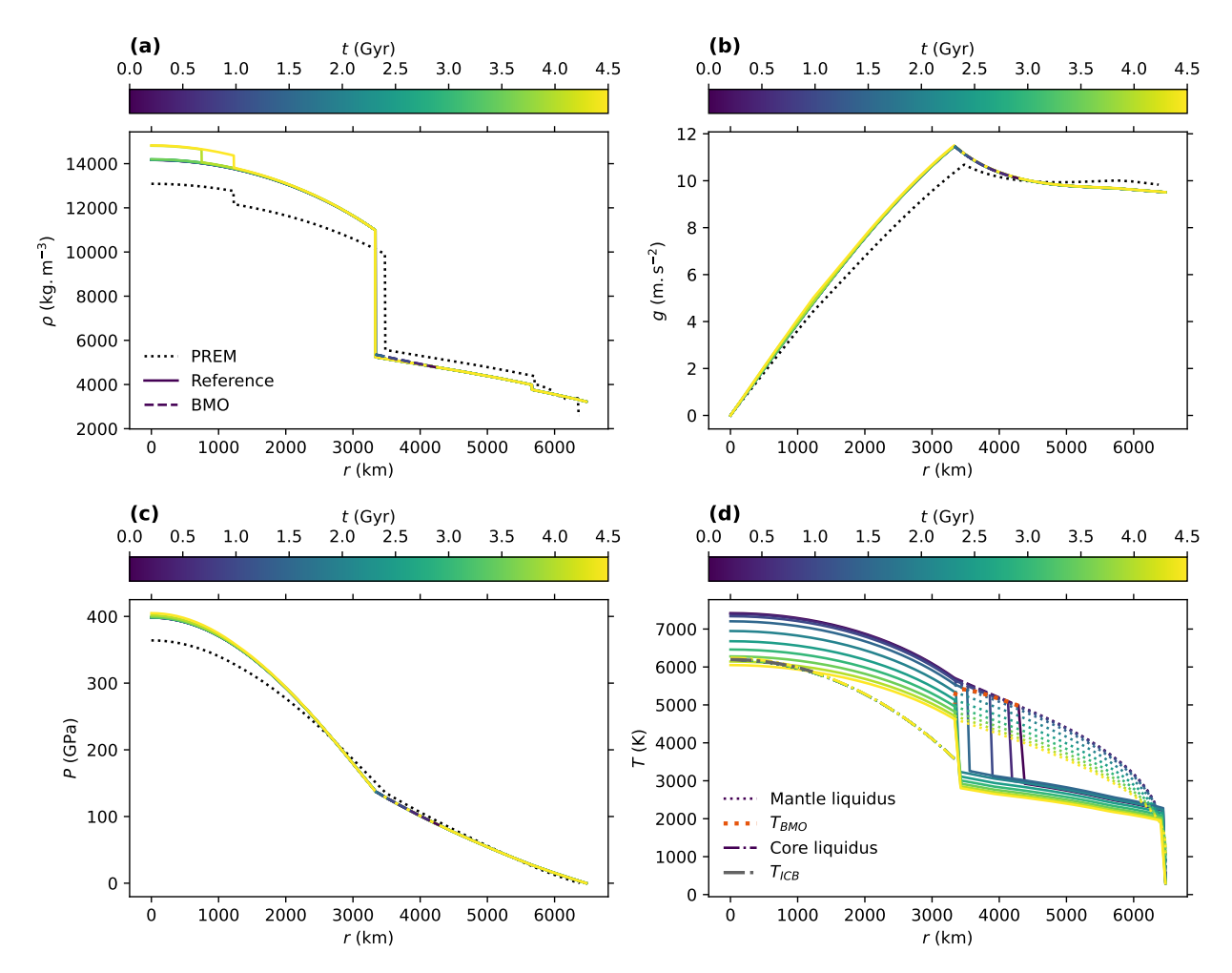


Figure 3: Density ρ (a), gravity g (b), pressure P (c) and temperature T (d) as a function of the radius r. Solid lines correspond to profiles obtained using the reference model. Dashed lines correspond to profiles using the BMO model. The colors correspond to the time t. Black dotted lines correspond to the Preliminary Reference Earth Model (PREM) defined by Dziewonski and Anderson (1981). Panel (d): Colored dotted lines and dash-dotted lines correspond respectively to the mantle and core liquidus. The red dotted line and the dash-dotted line correspond respectively to the temperature at the top of the BMO and at the ICB.

the radius of the planet, of the CMB and of the solid phase transitions slightly change over time as the temperature of the planet decreases and upon crystallization of the inner core. For the same reasons, the gravity and pressure profiles also change slowly over time.

In the mantle, the temperature profile (Fig. 3d) is defined by the BMO model (Eq. 11) and by the mantle thermal boundary layer model (Eq. 20-21). The BMO, defined by the intersection between the adiabatic profile and the mantle liquidus, crystallizes progressively from the top down until it fully solidifies at 2.8 Gyr. The mantle liquidus decreases over time as the BMO is increasingly enriched in FeO (Eq. 13), producing a depression of the melting curve as the BMO crystallizes (Boukaré et al., 2015; Ballmer et al., 2017; Blanc et al., 2020). In the core, the temperature profile is defined by the reference model (Eq. 7). The inner core starts to crystallize at 3.8 Gyr, when the temperature profile of

600

601

602

603

604

605

606

607

the core intersects the core liquidus at the center of the planet. The core liquidus is fixed over time because it is defined for an imposed composition (Eq. 9).

3.2. Thermal evolution

Fig. 4 shows the thickness of the BMO and the radius of the inner core, the temperatures at the top of the BMO, at the CMB, at the ICB and at the center of the planet, as well as the composition of the BMO and the core as a function of time for the nominal model. The planet initially starts with a fully liquid core and a thick BMO (Fig. 4a). As the BMO progressively crystallizes, the temperature at the CMB decreases whereas the temperature at the top of the BMO increases as the depth of this upper interface increases (Fig. 4b). Before 1.6 Gyr, the temperature evolution at the top of the BMO is dominated by fast crystallization, which explains this temperature increase. After 1.6 Gyr, the BMO crystallization rate significantly diminishes, in relation with its observed temperature decrease, caused by overall planet cooling. At 2.8 Gyr, the temperature at the top of the BMO merges with that at the CMB (within 1 K), which means that the BMO is fully crystallized (within 1 km), according to the criterion defined in \$2.2.4. During the crystallization, the BMO is progressively enriched in FeO (Fig. 4c). Between 2.8 Gyr and 3.8 Gyr, the planet progressively cools, with a fully crystallized BMO and a fully molten core. At 3.8 Gyr, the central temperature of the planet becomes smaller than the core liquidus (Fig. 4b), leading to core nucleation. As the size of the inner core increases (Fig. 4a), the outer core is progressively enriched in light elements (Fig. 4c).

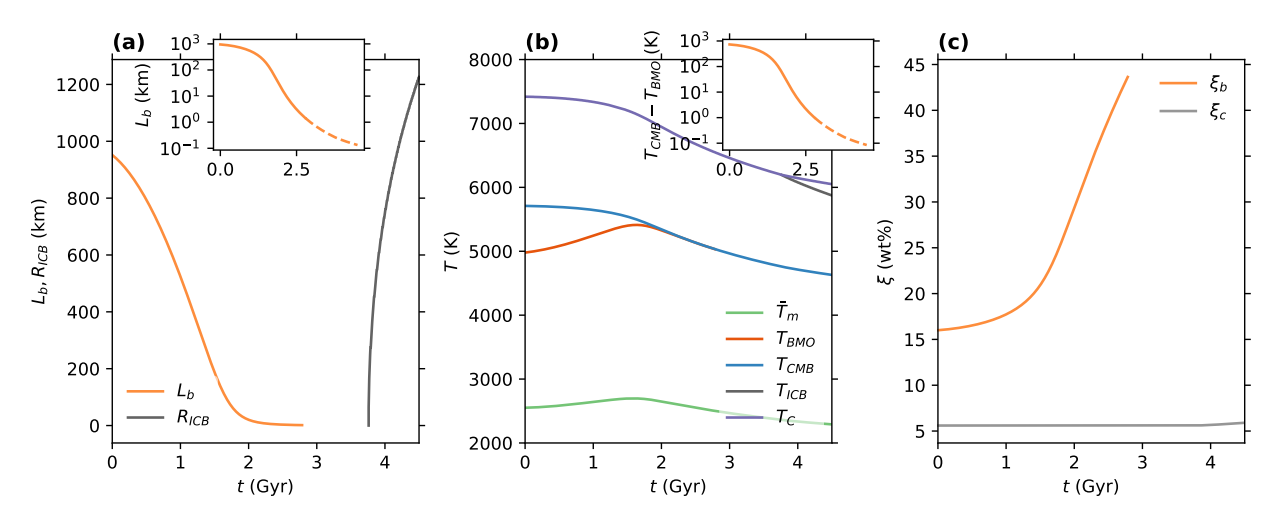


Figure 4: (a) BMO thickness L_b and ICB radius R_{ICB} as a function of time t. Inset: L_b , in logarithmic scale, as a function of t. The dashed line corresponds to thicknesses where the temperature difference across the BMO is less than 1 K. (b) Temperature at the top of the BMO T_{BMO} , at the CMB T_{CMB} , at the ICB T_{ICB} and at the center of the planet T_C as a function of time t. Inset: Temperature difference across the BMO $T_{CMB} - T_{BMO}$, in logarithmic scale, as a function of t. The dashed line corresponds to temperature differences across the BMO that are less than 1 K. (c) Mass fraction of the BMO FeO ξ_b and of the core light elements ξ_c as a function of time t.

Fig. 5 shows the heat flows in the mantle, the BMO and the core as a function of time for the nominal model. The heat flow at the surface of the planet is mainly driven by the heat flow at the top of the BMO when it exists, *i.e.* by the activity in the BMO and the core (Fig. 5a). The surface heat flow Q_P (Eq. 25) initially increases during 1.6 Gyr, due to an increasing temperature difference across the mantle, explained by the increasing depth of the interface between the BMO and the mantle. After 1.6 Gyr, the surface heat flow decreases as the crystallization rate of the BMO decreases (Fig. 4a). Similarly, the secular cooling of the mantle $Q_{S,m}$ (Eq. 84) initially increases for 2.0 Gyr as the cooling rate at the CMB increases (Fig. 4b) and as the volume of the mantle progressively expands, due to the crystallization of the BMO. After 2.0 Gyr, the secular cooling of the mantle decreases, consistently with a decreasing cooling rate (Fig. 4b). Finally, although the volume of the mantle initially increases, the radiogenic heating of the mantle $Q_{R,m}$ (Eq. 82) decreases monotonously due to radioactive decay.

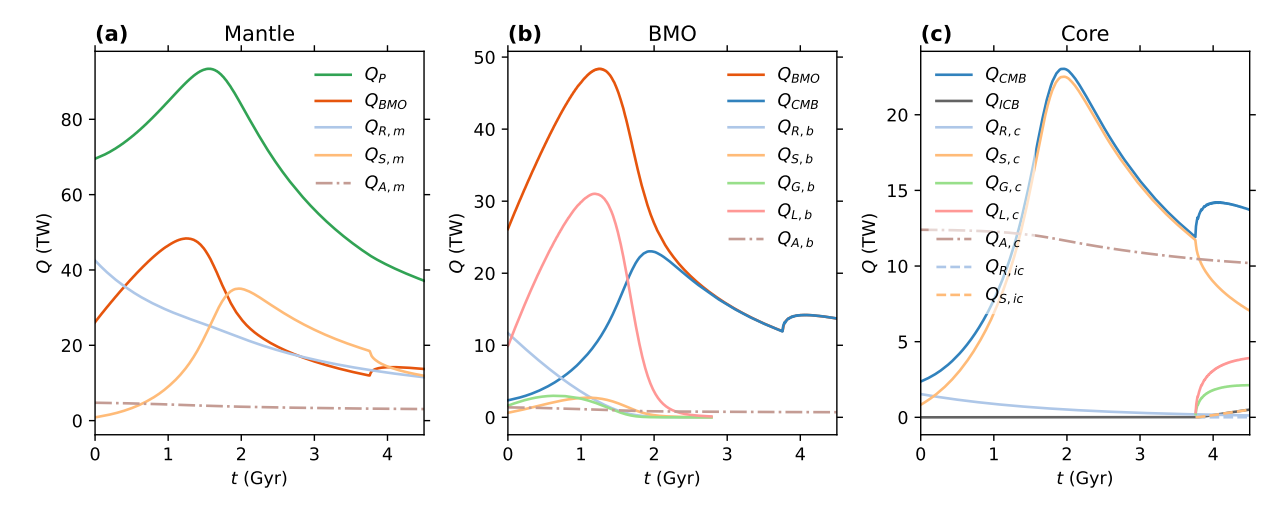


Figure 5: Heat flows Q in the mantle (a), the BMO (b) and the core (c) as a function of time t. The radiogenic heating, secular cooling, gravitational energy and latent heat terms are denoted with the subscripts R, S, G and L. The heat flows at the surface of the planet, at the top of the BMO, at the CMB and at the ICB are denoted with the subscripts P, BMO, CMB and ICB.

The heat flow at the surface of the BMO, Q_{BMO} , is mainly driven by the latent heat produced upon crystallization of the BMO (Fig. 5b). The latent heat flow, and thus the heat flow at the surface of the BMO, initially increase for 1.2 Gyr before decreasing until the BMO is fully crystallized. Since the latent heat $Q_{L,b}$ (Eq. 91) is proportional to the rate of crystallization of the BMO, this change may be explained by the transition from an increasing to a decreasing crystallization rate (Fig. 4a). Similarly, the gravitational energy $Q_{G,b}$ (Eq. 89) and the secular cooling $Q_{S,b}$ (Eq. 88) initially increase due to increased crystallization (Fig. 4a) and cooling rates (Fig. 4b). They eventually decrease as the BMO shrinks and as the crystallization and cooling rates decrease. Finally, the radiogenic heating of the BMO $Q_{R,b}$ (Eq. 87) decreases over time and goes to zero due a BMO decreasing in size, as well as radioactive decay.

Before the nucleation of the inner core, the heat flow at the CMB is mainly driven by the secular cooling of the core (Fig. 5c). The secular cooling of the core, and thus the heat flow at the CMB, initially increase during 2.0 Gyr before decreasing until the nucleation of the inner core. Since the secular cooling $Q_{S,c}$ (Eq. 94) is proportional to the cooling rate of the core, this evolution is consistent with the transition from an increasing to a decreasing cooling rate at the CMB (Fig. 4b). The initial increase of the CMB heat flow is explained by the concomitant crystallisation of the BMO, which increases the surface heat flow, and reduces, after 1.2 Gyr, the cooling rate buffer related to the BMO activity. After the nucleation of the inner core, the energy budget is significantly modified by contributions from the latent heat $Q_{L,c}$ (Eq. 97) and gravitational energy $Q_{G,c}$ (Eq. 95) released at the ICB, leading to an increasing heat flow at the CMB. The secular cooling $Q_{S,ic}$ (Eq. 99) and radiogenic heating $Q_{R,ic}$ (Eq. 98) of the inner core also contribute to this modification, but to a lesser extent. Finally, in contrast to the mantle and the BMO, the radiogenic heating of the core $Q_{R,c}$ (Eq. 92) is negligible, except at early times.

3.3. Buoyancy evolution

Fig. 6 shows the mass anomaly flux in the BMO and the outer core at different times. In the BMO, the total mass anomaly flux q_b is negative at all times, which means that the BMO is convective (Fig. 6a-c). The positive equivalent adiabatic sink $q_{A,b}$ is negligible in comparison with the negative buoyancy sources. At early times, the convection is mainly driven by the compositional term $q_{C,b}$, related to the release of FeO upon crystallization of the BMO (Fig. 6a). Close to the CMB, the heat produced by the core q_{CMB} dominates the buoyancy profile. As the BMO crystallizes, the radius fraction dominated by the influence of the core increases (Fig. 6b), until it dominates in the whole BMO (Fig. 6c). Although the radiogenic heating term $q_{R,b}$ is a major buoyancy source at early times (Fig. 6a), its influence significantly decreases over time due to radioactive decay. The secular cooling $q_{S,b}$ and dissipation $q_{G,b}$ terms are minor sources of buoyancy. The latent heat term $q_{L,b}$ does not contribute to the buoyancy profile since latent heat is released at the top of the BMO (Eq. 111).

In the core, the total mass anomaly flux q_c is initially positive before it becomes negative, which means that the core becomes convective after an initial stably-stratified stage (Fig. 6d-f). At early times, the buoyancy profile is dominated by the positive equivalent adiabatic sink $q_{A,c}$ (Fig. 6d). Subsequently, the negative buoyancy sources overcome the adiabatic sink, facilitating convection (Fig. 6e). Before nucleation of the inner core, the convection is mainly driven by secular cooling of the core $q_{S,c}$, with a minor and decreasing contribution of radiogenic heating $q_{R,c}$. After nucleation of the inner core, convection is mainly driven by the compositional term $q_{C,c}$, related to the release of light elements, and to a lesser extent by the latent heat term $q_{L,c}$ (Fig. 6f). The contributions from the inner core q_{ICB} , as well as dissipation $q_{G,c}$, are minor sources of buoyancy.

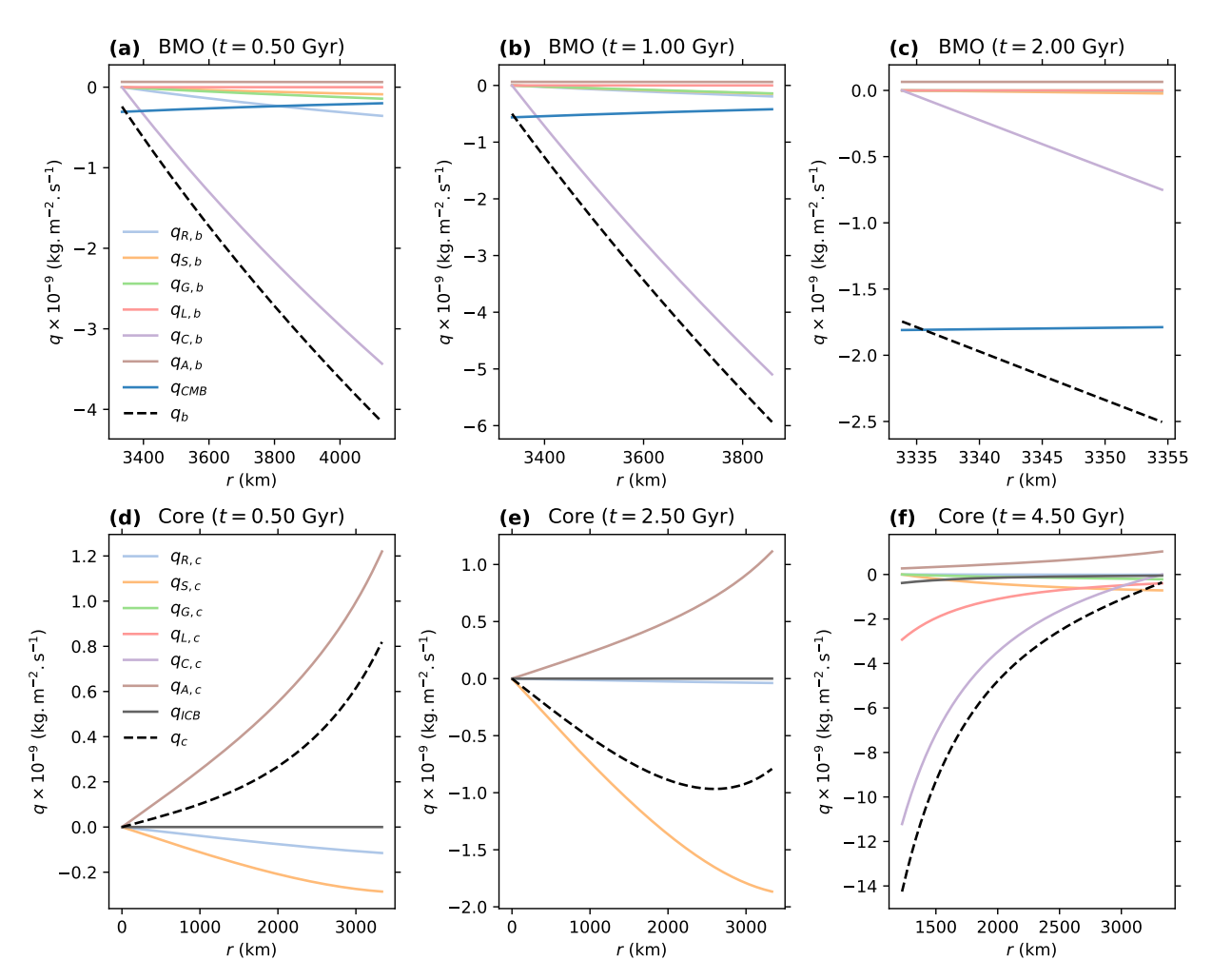


Figure 6: Mass anomaly flux q in the BMO at t=0.5 Gyr (a), t=1.0 Gyr (b) and t=2.0 Gyr (c), and in the outer core at t=0.5 Gyr (d), t=2.5 Gyr (e) and t=4.5 Gyr (f) as a function of radius r. Radiogenic heating, secular cooling, dissipation, latent heat, compositional and equivalent adiabatic buoyancy terms are denoted by the subscripts R, S, G, L, C and A. The contributions from the core at the CMB and from the inner core the ICB are denoted with the subscripts CMB and ICB. Dashed lines correspond to the total mass anomaly flux. The equivalent adiabatic terms use respectively $k_b=8$ W.m $^{-1}$.K $^{-1}$ and $k_c=70$ W.m $^{-1}$.K $^{-1}$.

Fig. 7 shows the time evolution of the total mass anomaly flux in the BMO and the outer core. In the BMO, the total mass anomaly flux q_b is always negative (Fig. 7a). Thus, the BMO is fully convective, from the combined action of compositional convection and heating at the CMB (Fig. 6a-c). In the core, the total mass anomaly flux q_c is initially positive, so that the core is fully stably-stratified (Fig. 7b). At 0.8 Gyr, the mass anomaly flux becomes progressively negative, starting from the bottom of the core, as the CMB heat flow and the core cooling rate increase. This produces an upper stably-stratified layer overlying a convective core. At 1.3 Gyr, the total mass anomaly flux eventually becomes negative all the way to the top of the core, making it fully convective, due to the increase of the secular cooling term (Fig. 6d-e). At 3.8 Gyr, a discontinuity in the total mass anomaly flux enhances the vigor of convection. The flux

673

674

675

676

677

678

magnitude suddenly increases with the release of latent heat at the ICB and the onset of compositional convection due to light elements released from the inner core (Fig. 6f).

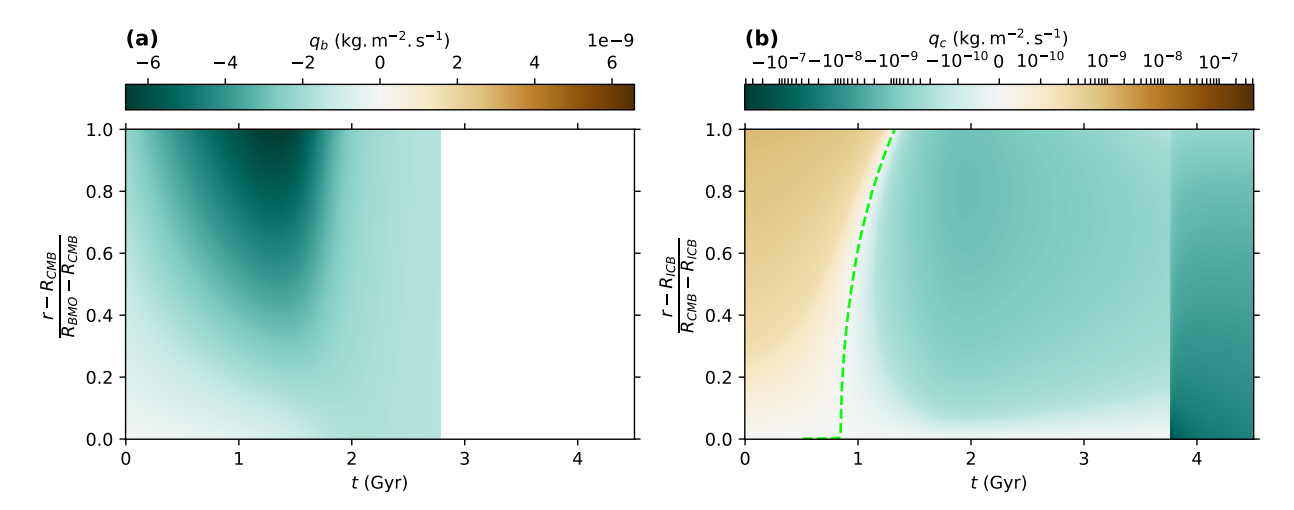


Figure 7: Total mass anomaly flux, *i.e.* buoyancy profiles, in the BMO q_b (a) and the outer core q_c (b) as a function of time t. Radii are normalized by the thickness of the corresponding layer.

3.4. Magnetic evolution

683

684

685

686

687

688

689

690

691

692

693

694

695

696

697

698

699

700

Fig. 8 shows the rates of entropy production in the BMO and the core as a function of time for our nominal model. In the BMO, the dissipation term $E_{\Phi,b}$ is always positive, which means that there is enough power available to sustain a dynamo in this layer (Fig. 8a). The entropy sources are dominated by the gravitational energy term $E_{G,b}$ (Eq. 120), consistently with the high efficiency factor associated with this term (Nimmo, 2015a), and to a lesser extent by the contribution of the core E_{CMB} (Eq. 122), particularly at late times when the BMO has shrunk significantly. The radiogenic heating term $E_{R,b}$ (Eq. 118) also contributes to the entropy budget, in particular at early times. In contrast, the secular cooling term $E_{S,b}$ (Eq. 119) is a minor source of entropy and the latent heat term $E_{L,b}$ (Eq. 121) does not contribute to the entropy budget since latent heat is released at the top the BMO. The gravitational energy $E_{G,b}$, secular cooling $E_{S,b}$ and core contribution E_{CMB} terms initially increase over time due to the increase of the corresponding heat sources, as a result of enhanced crystallization (Fig. 4a) and cooling (Fig. 4b) rates. They eventually decrease as the heat flows diminish, due to a shrinking BMO, reduced cooling and crystallization rates, and as the temperature difference between the top of the BMO and the CMB vanishes. In addition to the decrease in temperature difference, the radiogenic heating term $E_{R,b}$ also decreases due to a diminishing radiogenic heat flow, as a result of a shrinking BMO and radioactive decay. The entropy sinks are dominated by the thermal diffusion term $E_{k,b}$ (Eq. 123), with a negligible contribution from the molecular diffusion term $E_{a,b}$ (Eq. 124). They decrease monotonically over time, mainly because the BMO shrinks, but also because the average temperature of the BMO initially rises as its average depth increases.

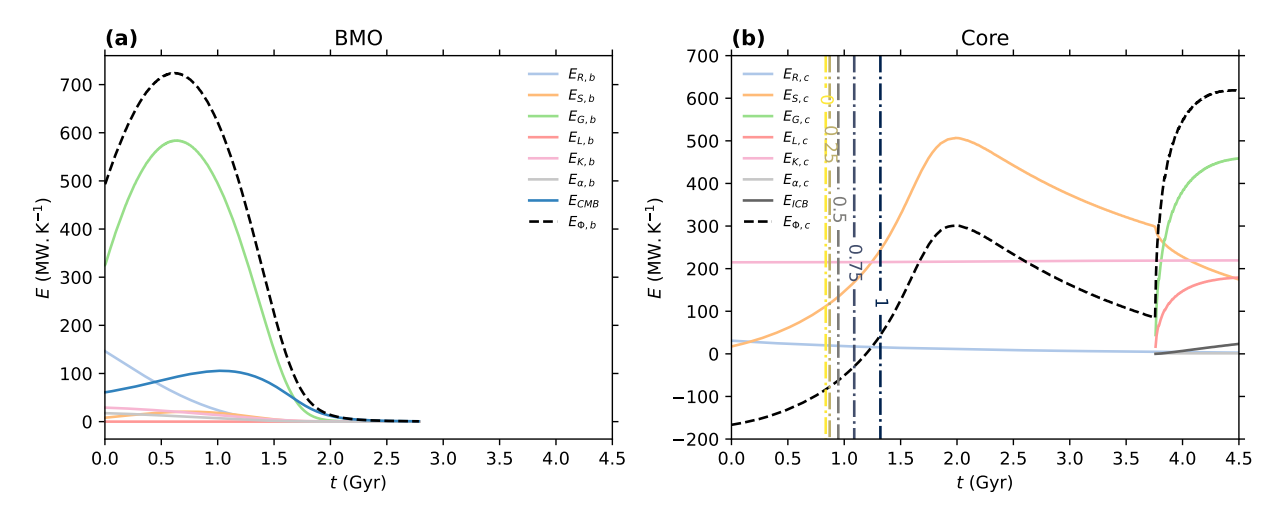


Figure 8: Rates of entropy production E in the BMO (a) and the outer core (b) as a function of time t. The radiogenic heating, secular cooling, gravitational energy, latent heat, thermal diffusion, molecular diffusion, and dissipation terms are denoted with the subscripts R, S, G, L, k, α and Φ . The contributions from the core at the CMB and from the inner core the ICB are denoted with the subscripts CMB and ICB. The thermal diffusion terms use respectively $k_b = 8 \text{ W.m}^{-1}.\text{K}^{-1}$ and $k_c = 70 \text{ W.m}^{-1}.\text{K}^{-1}$.

Before nucleation of the inner core, the dissipation term $E_{\Phi,c}$ is initially negative for 1.2 Gyr, which means that there is not enough power to sustain an early dynamo in this layer (Fig. 8b). Although the secular cooling term $E_{S,c}$ (Eq. 119) increases with time, as the CMB heat flow and core cooling increase, the entropy budget is dominated by the thermal diffusion sink $E_{k,c}$ (Eq. 123). After 1.2 Gyr, dissipation becomes positive as the secular cooling term continues to increase, and core convection starts, allowing sufficient power to sustain a core dynamo. The secular cooling term $E_{S,c}$ initially increases due to the increase of the corresponding heat flow (Fig. 5c) from enhanced cooling at the CMB (Fig. 4b). At 2.0 Gyr, it eventually decreases as the heat flow diminishes. The radiogenic heating term $E_{R,c}$ (Eq. 118), which decreases over time due to radioactive decay, is negligible. The thermal diffusion term $E_{k,c}$ is almost constant, due to a decreasing core temperature balanced by a reduced temperature gradient.

After nucleation of the inner core, the dissipation term $E_{\Phi,c}$ increases significantly, mainly due to the gravitational energy $E_{G,c}$ (Eq. 120) and latent heat $E_{L,c}$ (Eq. 121) released at the ICB. Radiogenic heating and secular cooling of the inner core E_{ICB} (Eq. 122) also contribute to this increase. The gravitational energy $E_{G,c}$, latent heat $E_{L,c}$ and inner core contribution E_{ICB} terms increase over time, until they are diminished by decreasing crystallization and cooling rates, and as the outer core shrinks.

Fig. 9 shows the magnetic Reynolds numbers and the internal magnetic field intensities in the BMO and the core, as well as the corresponding surface magnetic field intensities as a function of time for the nominal model. The scaling laws obtained from a fit on dynamo numerical simulations are compared with scaling laws based on force balance arguments (Appendix H). In the BMO, the magnetic Reynolds number obtained using the best-fit scaling law is initially

larger than $R_m = 40$ during 1.0 Gyr, which means that a self-sustained dynamo is operating in this layer (Fig. 9a). The average intensities of the corresponding internal and surface magnetic fields are, respectively, B = 1.2 mT and $B_P = 140.4 \,\mu\text{T}$ (Fig. 9b-c). After 1.0 Gyr, the magnetic Reynolds number decreases below the critical value as the size of the BMO and the convective velocity decrease, thereby suppressing magnetic field growth in the BMO. In the core, the magnetic Reynolds number obtained using the best-fit scaling law is larger than $R_m = 40$ after 1.2 Gyr, before which the power available to sustain a dynamo is insufficient (Fig. 8b). The average intensities of the corresponding internal and surface magnetic field are respectively B = 1.4 mT and $B_P = 17.3 \,\mu\text{T}$.

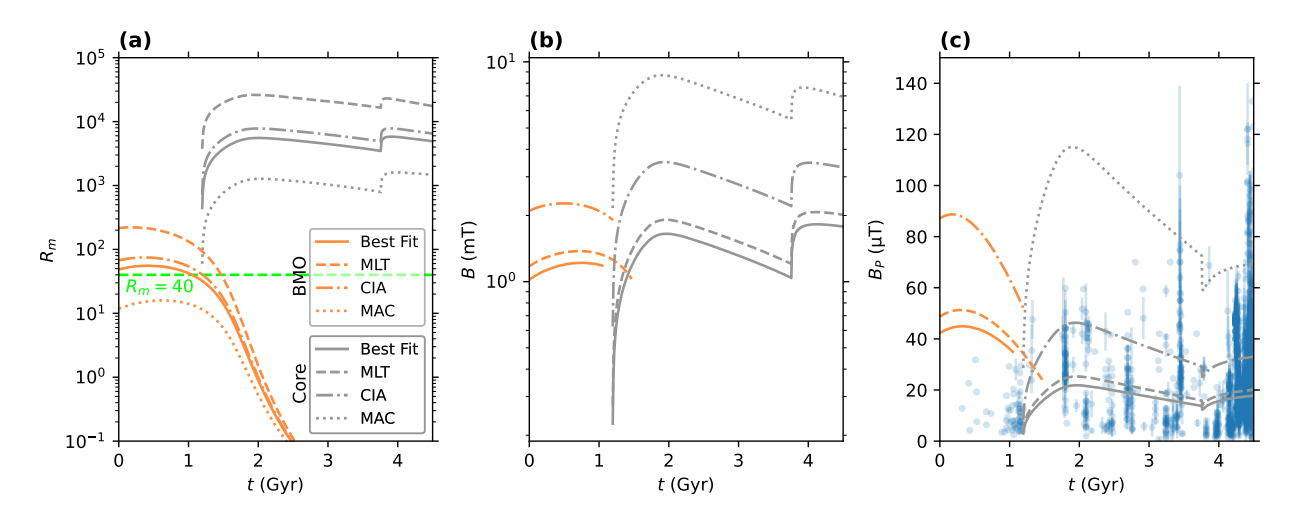


Figure 9: Magnetic Reynolds number R_m (a), internal magnetic field intensity B (b) and surface magnetic field intensity B_P (c) as a function of time t. The solid (BMO) and dashed (core) lines are obtained using the best-fit scaling law of Aubert et al. (2009). The dash-dotted (BMO) and dotted lines (core) are obtained using power-law scalings with an imposed exponent derived from the mixing length theory (MLT), the Coriolis-Inertia-Archimedean (CIA) or the Magnetic-Archimedean-Coriolis (MAC) regime. The magnetic Reynolds numbers use respectively $\sigma_b = 3 \times 10^4 \ \mathrm{S.m^{-1}}$ and $\sigma_c = 1 \times 10^6 \ \mathrm{S.m^{-1}}$. The gray markers correspond to Earth's paleomagnetic measurements of the surface magnetic field from the PINT database (Bono et al., 2022).

In both the BMO and the core, the estimated magnetic Reynolds number and the magnetic field intensities are sensitive to the scaling law for convective velocity and magnetic field intensity. For the magnetic Reynolds numbers, the CIA scaling law is closer to the best-fit scaling law than the MLT and MAC scaling laws (Fig. 9a), whereas for the magnetic field intensities, the MLT scaling law is closer to the best-fit scaling law than the CIA and MAC scaling laws (Fig. 9b-c). Depending on the scaling law, the magnetic Reynolds numbers and the magnetic field intensities in the BMO and the core may vary by more than an order of magnitude. In the BMO, the MAC scaling law predicts a magnetic Reynolds number smaller than the critical value. This explains the lack of magnetic field with this scaling law.

4. Sensitivity to the model parameters

735

736

737

738

739

741

743

744

745

746

761

762

763

In this section, we investigate the sensitivity of the model to several parameters. We focus on the role of the initial temperature at the CMB (§4.1), the parameterization of mantle convection (§4.2), as well as the composition (§4.3) and radiogenic heating (§4.4) of the BMO and the core. We also investigate the sensitivity to the thermal and electrical conductivities of these layers (§4.5). We do not investigate systematically the thermodynamic parameterization of the mantle, BMO and core, *i.e.* the parameterization of the solid phase transitions, EOS, and liquidus.

4.1. Initial temperature at the CMB

In our model, the initial temperature at the CMB, which corresponds to the temperature at which the BMO adiabat is tangent to the liquidus, is set to $T_{CMB_0} = 5710$ K. This is the maximum value used for our parameter sweep, because a higher temperature would produce a fully molten mantle instead of the intended BMO. The minimum value of the sweep, *i.e.* $T_{CMB_0} = 5010$ K, delineates a transition toward an inconsistent situation whereby the low temperature difference across the mantle and thick upper boundary layer (Eq. 19) produce insufficient heat flow (25) to accommodate the imposed radiogenic heat flow.

Fig. 10 shows the entropy of dissipation, the magnetic Reynolds number and the intensity of the surface magnetic 747 field as a function of the difference ΔT_{CMB_0} with the initial temperature used the nominal model, for the BMO and 748 the core. When ΔT_{CMB_0} increases, the initial thickness of the BMO decreases, and the surface heat flow increases due 749 to an increased temperature difference between the top of the BMO and the surface. The BMO then crystallizes earlier 750 (Fig. 10a) and the silicate dynamo operation window is reduced (Fig. 10c,e). If $T_{CMB_0} \le 5690$ K, the silicate dynamo 751 vanishes. If $T_{CMB_0} \le 5620$ K, the mantle remains fully solid. When ΔT_{CMB_0} increases, the thickness of the BMO 752 diminishes. This increases the temperature at the top of the BMO, and reduces the gravitational energy of the BMO (Eq. 753 89). The entropy of gravitational energy (Eq. 120), dominant in the BMO entropy budget (Fig. 8a), thus decreases, 754 reducing the entropy of dissipation (Fig. 10a). Assuming $\alpha_u = 2/5$ (see Table S8), the magnetic Reynolds number 755 scales as $\Phi^{2/5}$ (Eq. 46, 47 and 127). Since the convective power is proportional to the entropy of dissipation (Eq. 126), 756 the magnetic Reynolds number of the BMO decreases when ΔT_{CMB_0} increases (Fig. 10c). Assuming $\alpha_B = 1/3$ (see 757 Table S8), the magnetic field intensity scales as $\Phi^{1/3}L_b^{-2/3}$ (Eq. 48 and 127). Since the BMO thickness decreases when 758 ΔT_{CMB_0} increases, the magnetic field intensity of the BMO slightly increases (Fig. 10e), even if the convective power 759 decreases as a result of a reduced entropy of dissipation.

If the BMO exists, increasing ΔT_{CMB_0} enhances the heat flow at the CMB, due to an increased surface heat flow and an earlier BMO crystallization. Sufficient power is then available to allow an earlier core dynamo onset (Fig. 10b,d,f). Furthermore, the resulting colder core crystallizes earlier. In contrast, if the mantle remains solid, increasing ΔT_{CMB_0} reduces the temperature difference through the mantle and therefore the heat flow at the surface (Eq. 25). If

 $T_{CMB_0} \le 5210$ K, the CMB heat flow then becomes insufficient to power a core dynamo at early times (Fig. 10b,d,f). Inner core nucleation then becomes necessary to sustain a magnetic field. When corrected for the time shift related to inner core nucleation, the entropy of dissipation (Fig. 10b), magnetic Reynolds number (Fig. 10d), and magnetic field intensity (Fig. 10f) of the core are relatively independent of T_{CMB_0} .

766

767

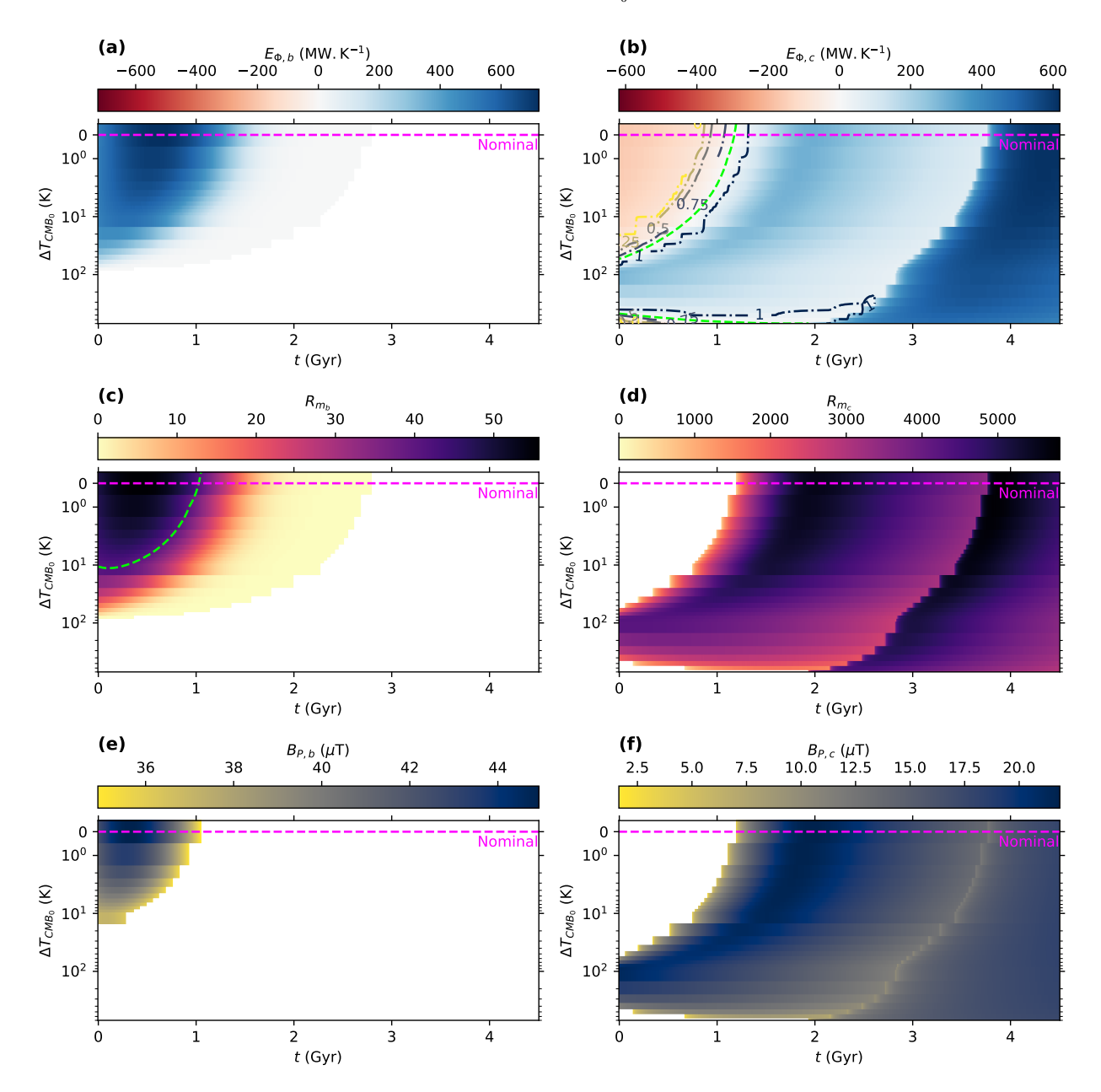


Figure 10: Sensitivity of the entropy of dissipation E_{Φ} (a,b), magnetic Reynolds number R_m (c,d) and surface magnetic field intensity B_P (e,f) of the BMO (a,c,e) and the core (b,d,f) to the initial temperature at the CMB T_{CMB_0} , expressed as the difference ΔT_{CMB_0} with the initial temperature used the nominal model, as a function of time t. Green dashed lines correspond to $E_{\Phi}=0$ (a,b) and $R_m=40$ (c,d). Pink dashed lines correspond to the value of the parameter used in the nominal model.

4.2. Mantle convection

In our model, mantle convection is controlled by the thermal boundary layer model, which depends on the $Nu \propto Ra^{\beta}$ relationship, as well as the mantle viscosity and thermal conductivity. Here, we focus on the reference viscosity of the mantle μ_{m_0} , but provide a parameter sweep of β (Fig. S2) and the mantle thermal conductivity (Fig. S3) in the supplementary material. In order to obtain an Earth-like evolution, the nominal value of μ_{m_0} is set to 1.1×10^{15} Pa.s. The maximum value of the sweep, i.e. $\mu_{m_0} = 2.1 \times 10^{15}$ Pa.s, corresponds to the value above which the thickness of the BMO, and the temperature at the CMB, would initially increase, leading to a fully molten mantle instead of the intended BMO. Such a large μ_{m_0} would produce a thick upper boundary layer (Eq. 19), leading to an insufficient release of energy (Eq. 25) to obtain a BMO that decreases in size, and reduces the CMB temperature. The minimum value of the sweep is arbitrarily set to $\mu_{m_0} = 1.0 \times 10^{12}$ Pa.s.

Fig. 11 shows the entropy of dissipation, the magnetic Reynolds number and the intensity of the surface magnetic field as a function of μ_{m_0} for the BMO and the core. When μ_{m_0} decreases, the upper boundary layer becomes smaller (Eq. 19), which produces an enhanced surface heat flow (Eq. 25). This intensification of mantle convection leads to an earlier solidification of the BMO (Fig. 11a), associated with a shorter silicate dynamo operation window (Fig. 11c). When μ_{m_0} decreases, the BMO crystallizes faster, increasing the dominant entropy of gravitational energy (Eq. 120), and the associated entropy of dissipation (Fig. 11a). The magnetic Reynolds number also increases (Fig. 11c), since the convective power increases with the entropy of dissipation (Eq. 126), and because the magnetic Reynolds number scales as $\Phi^{2/5}$ (Eq. 46, 47 and 127). Similarly, the magnetic field intensity increases (Fig. 11e), since the convective power and the thickness of the BMO respectively increases and decreases when μ_{m_0} decreases, and because the magnetic field scales as $\Phi^{1/3} L_h^{-2/3}$ (Eq. 48 and 127).

In the core, the decrease of μ_{m_0} allows for an earlier dynamo onset, starting at initial time when $\mu_{m_0} \le 4 \times 10^{13}$ Pa.s (Fig. 11b,d,f). This may be explained by an increased surface heat flow and an earlier solidification of the BMO, increasing the heat flow at the CMB and providing sufficient power to sustain an earlier magnetic field. The enhanced cooling of the core is also responsible for an earlier inner core nucleation, leading to a full crystallization when $\mu_{m_0} \le 1 \times 10^{13}$ Pa.s (Fig. 11b,d,f). Since the cooling rate of the core increases when μ_{m_0} decreases, the entropy source terms increase along with the entropy of dissipation (Fig. 11b). The magnetic Reynolds number (Fig. 11d) and the magnetic field intensity (Fig. 11f) also increase from the enhanced convective power (Eq. 47 and 48).

4.3. Composition

In our model, the composition of the BMO strongly influences the planet evolution, and is governed by the the iron partition coefficient D_{BMO} and the initial mass fraction ξ_{b_0} of FeO. However, our model is independent of the core composition because we define the EOS and the liquidus of the core with a fixed light element content. In addition,

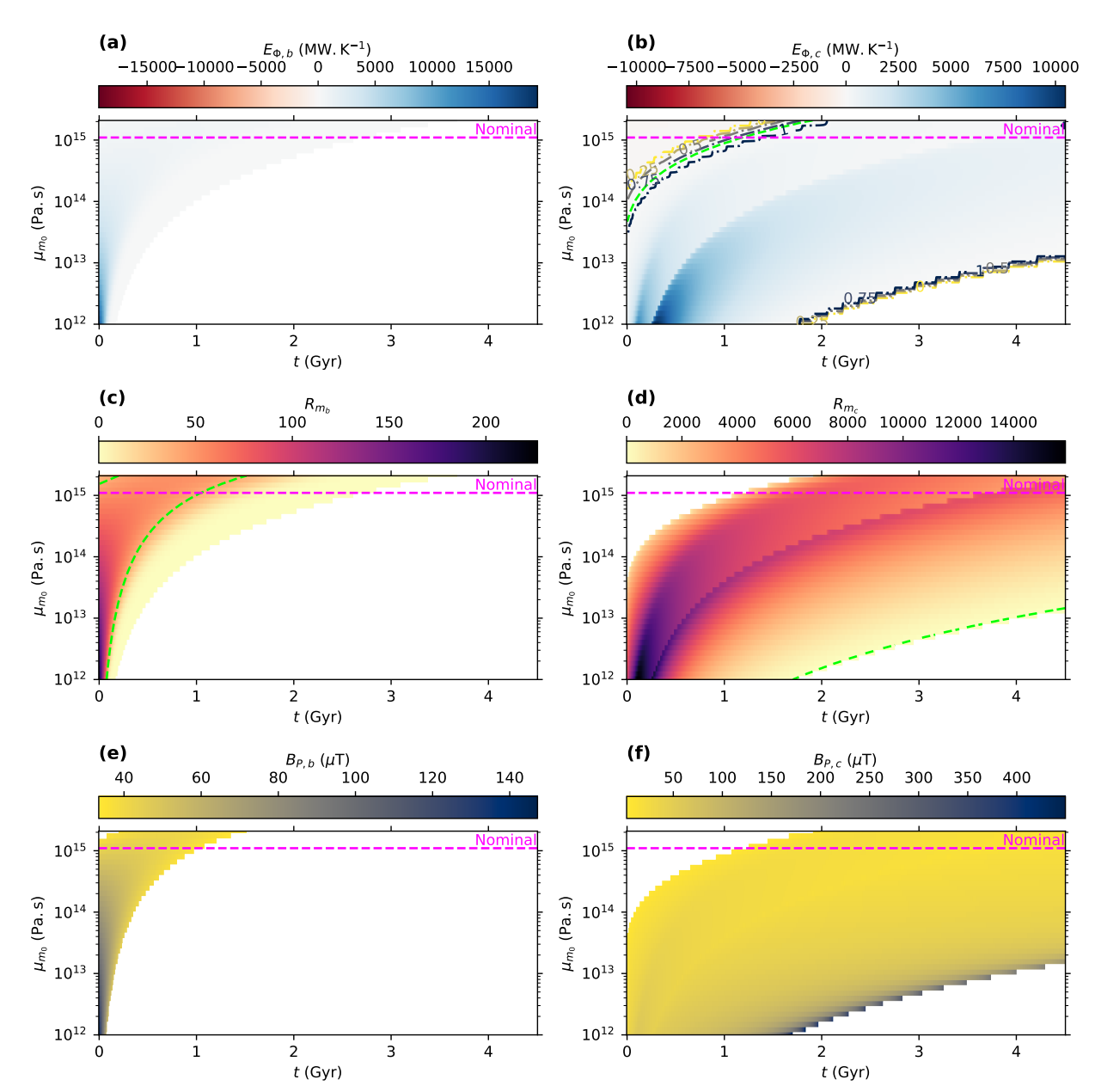


Figure 11: Sensitivity of the entropy of dissipation E_{Φ} (a,b), magnetic Reynolds number R_m (c,d) and surface magnetic field intensity B_P (e,f) of the BMO (a,c,e) and the core (b,d,f) to the reference viscosity of the mantle μ_{m_0} , as a function of time t. Green dashed lines correspond to $E_{\Phi}=0$ (a,b) and $R_m=40$ (c,d). Pink dashed lines correspond to the value of the parameter used in the nominal model.

the planet evolution is also influenced by the compositional density jump at the top of the BMO $\Delta_{\xi}\rho_{BMO}$ and at the ICB $\Delta_{\xi}\rho_{ICB}$. Here, we focus on D_{BMO} , but we provide a parameter sweep of ξ_{b_0} (Fig. S4), $\Delta_{\xi}\rho_{BMO}$ (Fig. S5) and $\Delta_{\xi}\rho_{ICB}$ (Fig. S6) in the supplementary material. To obtain an Earth-like evolution, we set the nominal value of the iron partition coefficient to $D_{BMO}=0.85$. We conduct the parameter sweep in the range $0 < D_{BMO} < 1$, where iron is preferentially partitioned into the melt.

800

801

802

803

804

Fig. 12 shows the entropy of dissipation, the magnetic Reynolds number and the intensity of the surface magnetic field as a function of D_{BMO} for the BMO and the core. When D_{BMO} decreases, the rate of release of FeO increases, raising the FeO content and depressing the liquidus. Furthermore, the temperature difference through the mantle decreases, reducing the surface heat flow (Eq. 25). This reduces the BMO crystallization rate (Fig. 12a) and extends the BMO-hosted dynamo operation window (Fig. 12c). When D_{BMO} decreases, the change in composition across the interface between the BMO and the mantle increases (Eq. 28), reducing the compositional expansion coefficient (Eq. 90, and decreasing the gravitational energy of the BMO (Eq. 89). The dominant entropy of gravitational energy (Eq. 120) therefore decreases, reducing the entropy of dissipation (Fig. 12a). Since the magnetic Reynolds number scales as $\Phi^{2/5}$ (Eq. 46, 47 and 127), it slightly decreases with D_{BMO} (Fig. 12c) due to the reduced convective power (Eq. 126). Similarly, the magnetic field intensity, which scales as $\Phi^{1/3}L_h^{-2/3}$ (Eq. 48 and 127), decreases with D_{BMO} (Fig. 12e), due to the reduced convective power and thicker BMO.

In the core, dynamo onset is largely independent of D_{BMO} (Fig. 12b,d,f), although it occurs slightly earlier for lower values of D_{BMO} . Lower D_{BMO} means an increase in the CMB cooling rate and heat flow at early time ($t \lesssim 1.3$ Gyr), compensating for reduced BMO heat flow and crystallization rate, from the depression of the liquidus. In contrast, lowering D_{BMO} means that the inner core nucleation is significantly delayed, leading to a fully liquid core at 4.5 Gyr, for $D_{BMO} \leq 0.35$ (Fig. 12b,d,f). This is explained by a lower CMB cooling rate from a lower surface heat flow for most of the later planet evolution ($t \gtrsim 1.3$ Gyr).

If $t \lesssim 1.3$ Gyr, the CMB cooling rate slightly increases when D_{BMO} decreases. The entropy of secular cooling, which dominates the entropy budget of the core before inner core nucleation, thus increases, leading to a slight increase of the entropy of dissipation (Fig. 12b). In contrast, if $t \gtrsim 1.3$ Gyr, lower CMB cooling rates lead to decreasing entropy of secular cooling and entropy of dissipation. Similarly, since the onset of core dynamo occurs when $t \gtrsim 1.3$ Gyr, the magnetic Reynolds number (Fig. 12d) and the magnetic field intensity (Fig. 12f) decrease due to reduced convective power (Eq. 47 and 48).

4.4. Radiogenic heating

In our model, radiogenic heating in the BMO and the mantle is controlled by the mantle fraction f_h of BSE radiogenic production. In the core, heat production is driven by the 40 K core concentration c_c . Here, we focus on f_h , but we provide a parameter sweep of c_c in the supplementary material (Fig. S7). The nominal value of the mantle fraction of the BSE radiogenic production is $f_h = 0.58$, and the sweep is conducted for $f_h > 0$. As with previous parameters, the maximum value of this parameter sweep, *i.e.* $f_h = 0.7$, corresponds to the value above which the thickness of the BMO, and the temperature at the CMB, would initially increase, leading to a fully molten mantle instead of the intended BMO. Such a large f_h would be responsible for low heat flows at the top of the BMO and at the

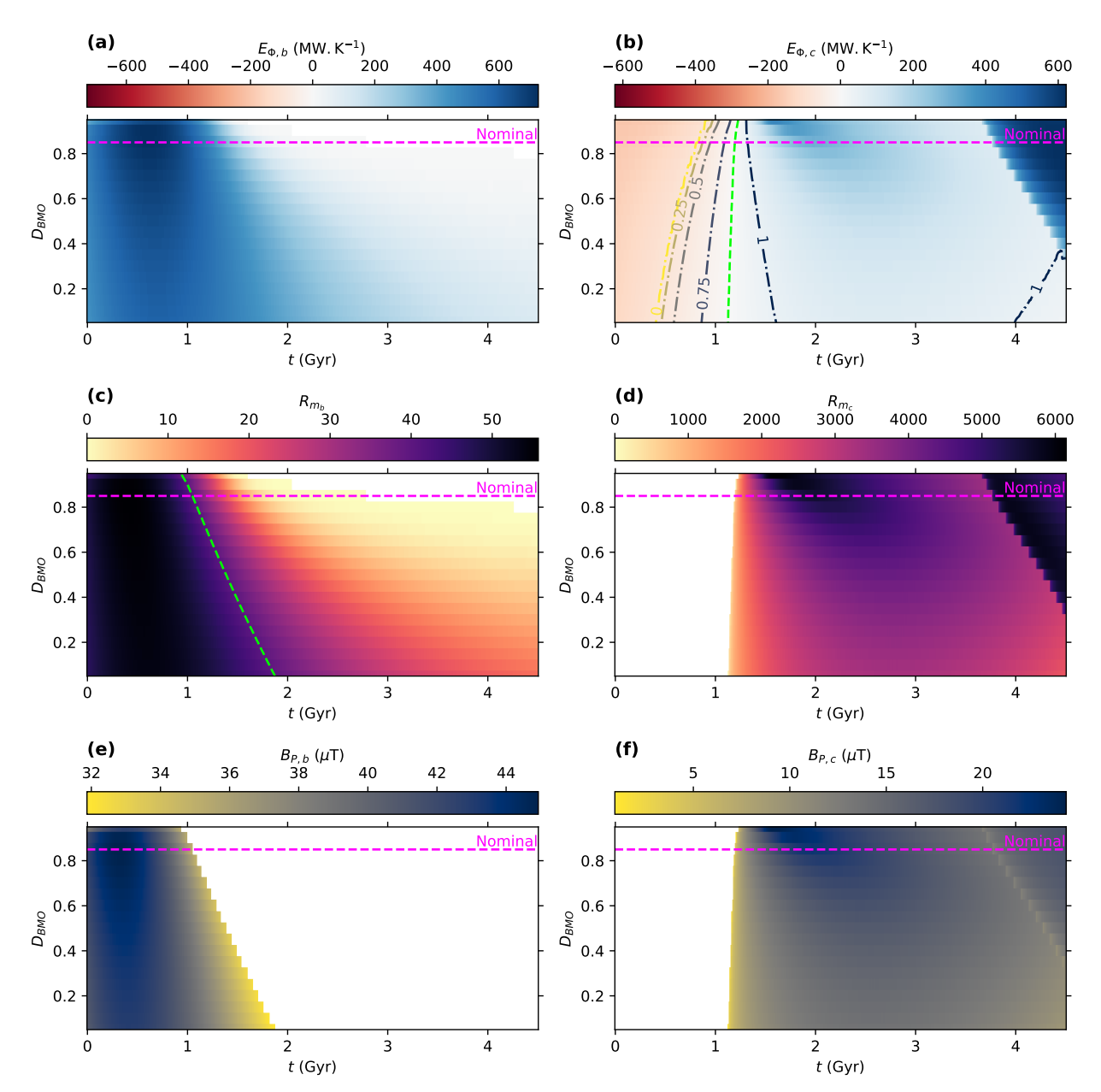


Figure 12: Sensitivity of the entropy of dissipation E_{Φ} (a,b), magnetic Reynolds number R_m (c,d) and surface magnetic field intensity B_P (e,f) of the BMO (a,c,e) and the core (b,d,f) to the iron partition coefficient D_{BMO} , as a function of time t. Green dashed lines correspond to $E_{\Phi}=0$ (a,b) and $R_m=40$ (c,d). Pink dashed lines correspond to the value of the parameter used in the nominal model.

CMB, leading to an insufficient release of energy to obtain a obtain a BMO decreasing in size, and reduce the CMB temperature.

Fig. 13 shows the entropy of dissipation, the magnetic Reynolds number and the intensity of the surface magnetic field as a function of f_h for the BMO and the core. When f_h increases, the internal heat production of the BMO and the solid mantle increases, leading to a reduced cooling rate of the BMO (Eq. 34), and therefore protracted

836

837

838

839

840

crystallization (Fig. 13a) and silicate dynamo operation (Fig. 13c). The entropy of dissipation decreases (Fig. 13a), as a larger f_h reduces the FeO release rate, reducing the dominant entropy source from gravitational energy (Eq. 120). The magnetic Reynolds number also decreases (Fig. 13c), since the convective power diminishes with decreasing entropy of dissipation, and because the magnetic Reynolds number scales as $\Phi^{2/5}$. Similarly, the magnetic field intensity decreases (Fig. 13e), since the convective power and the thickness of the BMO respectively decrease and increase as f_h increases, and because the magnetic field scales as $\Phi^{1/3}L_h^{-2/3}$ (Eq. 48 and 127).

In the core, the increase of f_h promotes a lower heat flow at the CMB, explaining a delayed dynamo onset and inner core nucleation (Fig. 13b,d,f). Since the cooling rate of the core decreases when f_h increases, the source terms of the entropy budget decrease, leading to a decreasing entropy of dissipation (Fig. 11b). The magnetic Reynolds number (Fig. 11d) and the magnetic field intensity (Fig. 11f) also decrease due to reduced convective power (Eq. 47 and 48).

4.5. Thermal and electrical conductivity

847

848

849

850

851

In the BMO, dynamo operation is mostly limited by the relatively low electrical conductivity σ_b of the silicates. In our model, we set the nominal value of σ_b to 3×10^4 S.m⁻¹ (Holmström et al., 2018; Soubiran and Militzer, 2018; Stixrude et al., 2020). To obtain a consistent parameter sweep, the thermal conductivity of the BMO k_b is defined concomitantly with σ_b , using the Wiedemann-Franz law. We define the total thermal conductivity as the sum of ionic $k_{b,l}$ and electronic $k_{b,e}$ contributions

$$k_b = k_{b,l} + k_{b,e}.$$
 (53)

Following Deng and Stixrude (2021), the ionic contribution is

$$k_{b,l} = k_{b,l_0} \left(\frac{T}{T_k}\right)^{a_{k,b}} \left(\frac{\rho}{\rho_k}\right)^{b_{k,b}},$$
 (54)

where the prefactor k_{b,l_0} , the exponents $a_{k,b}$ and $b_{k,b}$, as well as the reference temperature T_k and density ρ_k are defined in Table S6, and where temperature and density are averaged over the BMO at any given time. The electronic contribution is related to the electrical conductivity of the BMO by the Wiedemann-Franz law

$$k_{b,e} = LoT\sigma_b, \tag{55}$$

where the temperature is averaged over the BMO at any given time and Lo is the Lorenz number. Since Lo remains uncertain in the BMO (Soubiran and Militzer, 2018), we use the theoretical value $Lo = 2.443 \times 10^{-8} \text{ V}^2.\text{K}^{-2}$. The time-averaged thermal conductivity of the BMO, which varies only marginally over time (see Fig. S8), is obtained

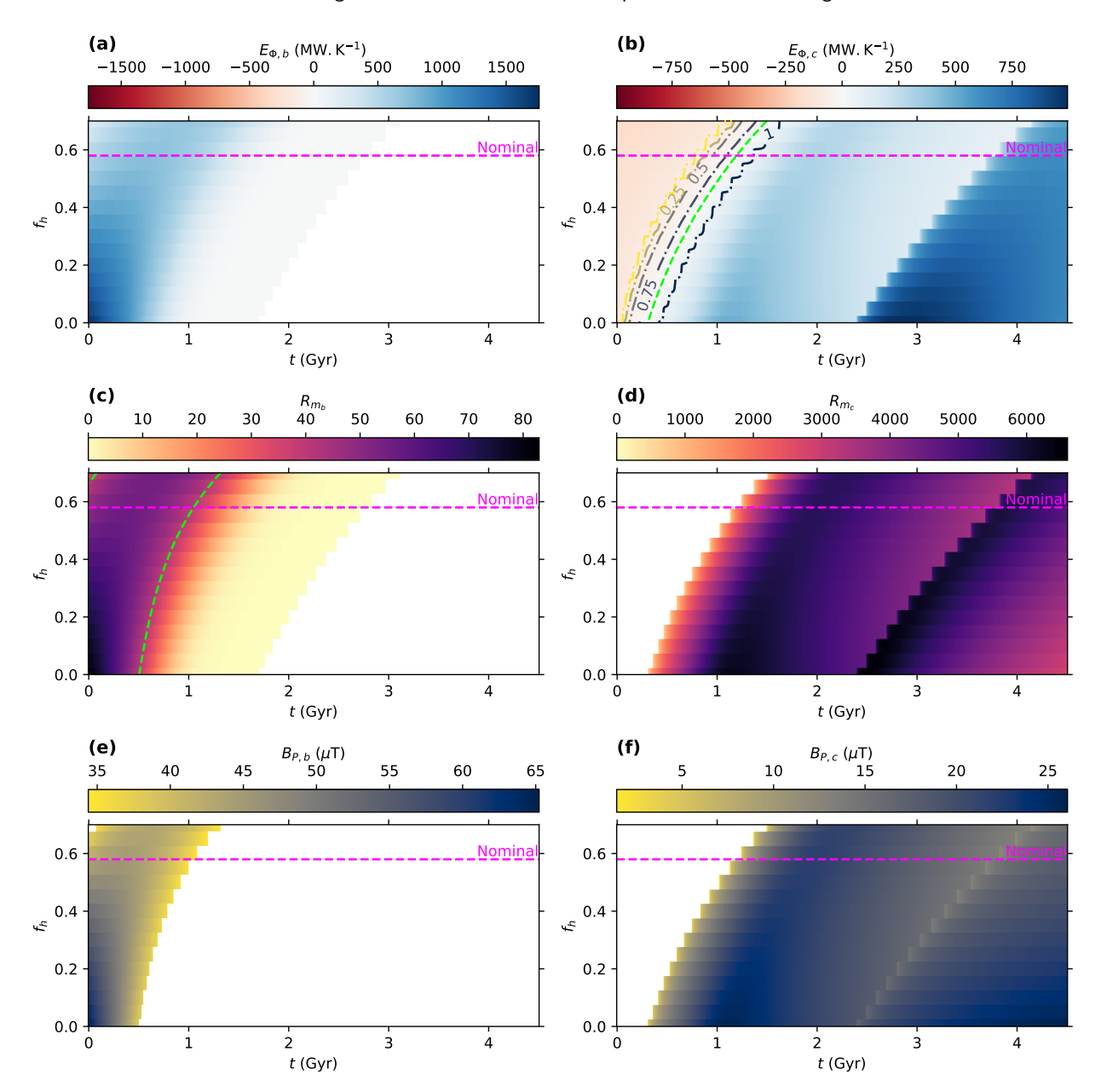


Figure 13: Sensitivity of the entropy of dissipation E_{Φ} (a,b), magnetic Reynolds number R_m (c,d) and surface magnetic field intensity B_P (e,f) of the BMO (a,c,e) and the core (b,d,f) to the mantle fraction of the BSE radiogenic heating f_h , as a function of time t. Green dashed lines correspond to $E_{\Phi}=0$ (a,b) and $R_m=40$ (c,d). Pink dashed lines correspond to the value of the parameter used in the nominal model.

by using the nominal value of σ_b in Eq. 55. This gives $k_b = 8.03 \text{ W.m}^{-1}.\text{K}^{-1}$, where $k_{b,l} = 4.26 \text{ W.m}^{-1}.\text{K}^{-1}$ and $k_{b,e} = 3.77 \text{ W.m}^{-1}.\text{K}^{-1}$, consistently with the imposed $k_b = 8 \text{ W.m}^{-1}.\text{K}^{-1}$ in the nominal model.

In the core, dynamo operation is mostly limited by the thermal conductivity k_c of the liquid metal, the core being an efficient electrical conductor (Williams, 2018). In our model, we set the nominal value of k_c to 70 W.m⁻¹.K⁻¹ (Ohta et al., 2016; Basu et al., 2020; Hsieh et al., 2020; Pozzo et al., 2022). As with the BMO, we define the electrical

866

867

868

conductivity of the core σ_c concomitantly with k_c , using the Wiedemann-Franz law. However, since the electronic contribution is the only factor contributing to k_c , we have

$$k_c = LoT\sigma_c,$$
 (56)

where temperature is averaged over the outer core at any given time. Since Lo remains uncertain in the core (Williams, 2018), we also use the theoretical value $Lo = 2.443 \times 10^{-8} \text{ V}^2.\text{K}^{-2}$. The time-averaged electrical conductivity of the core, which also marginally varies over time (see Fig. S8), is obtained by using the nominal value of k_c in Eq. 56. This gives $\sigma_c = 4.88 \times 10^5 \text{ S.m}^{-1}$, consistently with the imposed $\sigma_c = 1 \times 10^6 \text{ S.m}^{-1}$ in the nominal model.

Fig. 14 shows the entropy of dissipation, the magnetic Reynolds number, and the intensity of the surface magnetic field as a function of σ_b and k_c . Because the temperature and the density of the BMO and the core vary over time, the conductivities shown on the right y-axis, calculated using the Wiedemann-Franz law, correspond to time-averaged values.

In the BMO, the entropy of dissipation is always positive and varies by less than 10% over the range of thermal and electrical conductivity investigated (Fig. 14a). If the thermal conductivity increases, the entropy of dissipation, and therefore the power available to the dynamo, slightly decreases as the entropy of thermal diffusion increases (Eq. 123). In contrast, the magnetic Reynolds number increases significantly with electrical conductivity (Eq. 46), making a silicate dynamo possible if $\sigma_b \ge 2.15 \times 10^4 \text{ S.m}^{-1}$ (Fig. 14c). However, the intensity of the magnetic field produced in the BMO is relatively independent of the electrical conductivity (Fig. 14e), consistently with the relatively constant entropy of dissipation (Eq. 48 and 126).

In the core, the entropy of dissipation decreases when the thermal conductivity increases (Fig. 14b), due to an increasing entropy of thermal diffusion (Eq. 123). As a result, the time at which enough power is available to power a dynamo is delayed. In particular, if $k_c \ge 15.8 \text{ W.m}^{-1}.\text{K}^{-1}$, a core dynamo is impossible at early times. Furthermore, if $k_c \ge 168 \text{ W.m}^{-1}.\text{K}^{-1}$, the dynamo is impossible before the additional supply of entropy from inner core nucleation. If sufficient power is available, the magnetic Reynolds number is always greater than $R_m = 40$ (Fig. 14d), which means that a core dynamo is possible. Although an increasing thermal conductivity contributes to reduce the magnetic Reynolds number through reduced convective velocities, the evolution of the magnetic Reynolds number is dominated by the electrical conductivity (Eq. 46). Thus, the magnetic Reynolds number increases with the transport properties of the core. Finally, the intensity of the magnetic field decreases as the thermal conductivity increases (Fig. 14f), consistently with a reduced entropy of dissipation (Eq. 48 and 126).

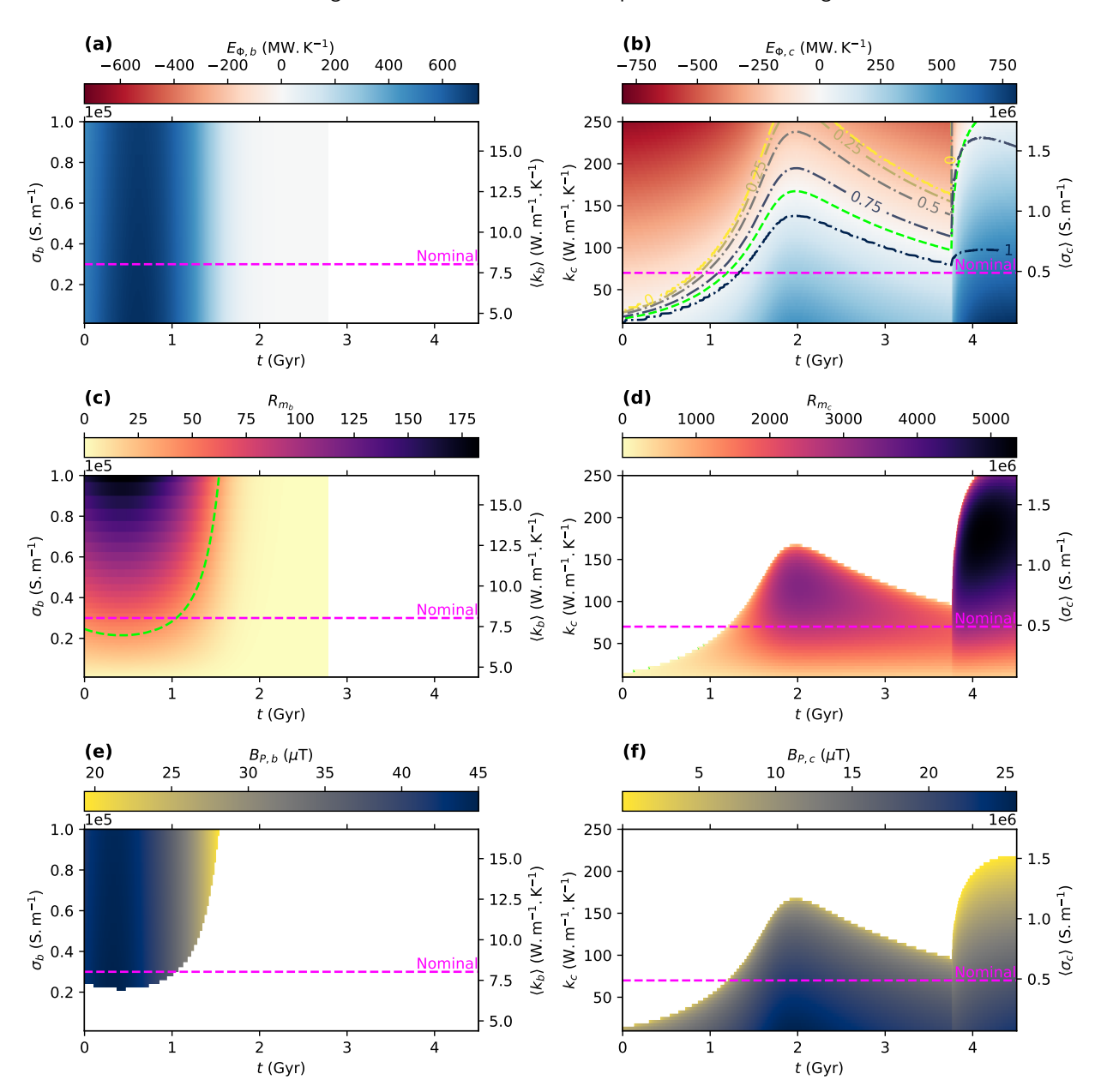


Figure 14: Influence of the BMO electrical conductivity σ_b (a,c,e) and of the core thermal conductivity k_c (b,d,f) on the entropy of dissipation E_{Φ} (a,b), magnetic Reynolds number R_m (c,d) and surface magnetic field intensity B_P (e,f), as a function of time t. The right y-axis shows the time-averaged thermal (a,c,e) and electrical (b,d,f) conductivities calculated from the imposed left y-axis conductivity using the Wiedemann-Franz law. Green dashed lines correspond to $E_{\Phi}=0$ (a,b) and $R_m=40$ (c,d). Pink dashed lines correspond to the value of the parameter used in the nominal model.

5. Discussion

896

897

898

5.1. Comparison with Earth

Our nominal model converges toward the present-day Earth structure. The density, gravity and pressure profiles of the planet (§3.1) are consistent with the Preliminary Reference Earth Model (PREM) (Dziewonski and Anderson,

1981). In detail, our model CMB is 4.3% deeper than PREM because Earth's mantle includes iron and is thus denser than pure MgSiO₃ (Boujibar et al., 2020). In addition, the core density is 11.1% larger in our model since our core EOS uses pure Fe. As such, the gravity at the CMB and the pressure at the center are respectively 11.1% and 11.2% larger than in PREM.

Temperatures at the CMB and at the ICB (§3.2) are respectively $T_{CMB} = 4630$ K and $T_{ICB} = 5874$ K at 4.5 Gyr, which is within, or close to, present-day estimates in the Earth's core, *i.e.* $T_{CMB} = 3400 - 4600$ K (Hirose et al., 2021) and $T_{ICB} = 5050 - 6250$ K (Nimmo, 2015b). Furthermore, the final radius of the model inner core is 1226 km, close to the 1221 km of actual Earth's inner core (Dziewonski and Anderson, 1981). At t = 0, the model temperature of the CMB is $T_{CMB_0} = 5710$ K. This is significantly higher than the $T_{CMB_0} = 4800 - 5000$ K temperature range obtained from metal-silicate equilibration (Fischer et al., 2017), but is compatible with previous models that give initial temperatures in the range $T_{CMB_0} = 4570 - 6400$ K (Driscoll and Davies, 2023).

Heat flows values at the CMB and the surface (§3.2) are respectively $Q_{CMB} = 13.7 \text{ TW}$ and $Q_P = 37.2 \text{ TW}$ at 4.5 Gyr. These are within the range estimated for the Earth, namely $Q_{CMB} = 5-17 \text{ TW}$ at the CMB and $Q_P = 35-41 \text{ TW}$ at the surface of the mantle (Jaupart et al., 2015).

Paleomagnetic data (Bono et al., 2022) are generally compatible with the magnetic field produced by a core dynamo 914 (§3.4). However, our nominal model present-day surface magnetic field $B_P = 17.8 \ \mu \text{T}$ is slightly smaller than the typical range estimated for the Earth, i.e. $B_P = 25 - 65 \mu T$ (Alken et al., 2021). The nominal model predicts a BMO silicate dynamo lifetime consistent with previous models, with typical cessation times in the range 1-2.5 Gyr (Ziegler and Stegman, 2013; Blanc et al., 2020; O'Rourke, 2020; Stixrude et al., 2020). However, the BMO magnetic field predicted before 1.0 Gyr is significantly larger than paleomagnetic measurements and previous models (O'Rourke, 919 2020; Stixrude et al., 2020). The model sensitivity to the magnetic scaling laws (Appendix H), initially developed for 920 the Earth's core, as well as various parameters (§4), may contribute to explaining these differences with the nominal 921 model. Uncertainties in paleomagnetic data must also be considered (Tarduno et al., 2010, 2015; Borlina et al., 2020; 922 Tarduno et al., 2020; Taylor et al., 2023). 923

5.2. Comparison to previous works

925

926

927

928

929

930

In this section, we highlight the main methodological extensions proposed by our model. We therefore propose a comparison to previous models that compute planetary evolution with energy budgets, leaving aside higher-dimension models (e.g. Zhang and Rogers, 2022).

In our model, we partially couple the radially integrated internal structure of an Earth-like planet with a BMO to its thermal evolution. This differs from earlier works (Labrosse et al., 2007; Ziegler and Stegman, 2013; Blanc et al., 2020; O'Rourke, 2020) where the internal structure of the planet is simplified by using fixed thermodynamic properties,

a radially-averaged BMO, and where the core is either radially-averaged or parameterized using radially-dependent polynomials. We also invoke a simple parameterization of the time-dependent compositional evolution of the BMO and consider its feedback on the EOS and melting curve. This differs from previous work for which the thermodynamic properties of the BMO are independent of composition (Labrosse et al., 2007; Ziegler and Stegman, 2013; Blanc et al., 2020; O'Rourke, 2020), and the melting curve depression is either imposed (Blanc et al., 2020), or defined using a linear phase diagram fixed over time (Labrosse et al., 2007; Ziegler and Stegman, 2013; O'Rourke, 2020).

We couple the core, BMO, and mantle in the planet energy budget, and prescribe the surface heat flow with a thermal 937 boundary layer model of the mantle. This augments previous work where the core energy budget is simplified (Labrosse 938 et al., 2007; Ziegler and Stegman, 2013; Blanc et al., 2020) and the cooling history of the BMO is imposed with a mantle 939 boundary layer model (Labrosse et al., 2007; Ziegler and Stegman, 2013), an exponential decay based on radiogenic 940 heating (Blanc et al., 2020), and a linear decay (O'Rourke, 2020). Furthermore, we determine the thermocompositional 0/1 stability of the BMO and the core, highlighting the dominant sources of convection and revealing potential stably-942 stratified layers. This builds upon previous work where this method was only applied to the core (Davies and Gubbins, 943 2011; Pozzo et al., 2012; Gubbins et al., 2015). Finally, we determined the conditions of dynamo operation in the BMO 944 and the core by using entropy budgets to assessing if sufficient power is available to sustain a magnetic field, and if 945 magnetic induction exceeds magnetic diffusion, using magnetic Reynolds numbers. This extends previous work where 946 the dynamo activity is only assessed through magnetic Reynolds numbers (Ziegler and Stegman, 2013; Scheinberg 947 et al., 2018; O'Rourke, 2020), or entropy budgets (Blanc et al., 2020).

5.3. Sensitivity of the model

0/10

950

951

952

953

956

957

958

959

960

961

The planet evolution is sensitive to several parameters, including the initial temperature at the CMB (§4.1), the parameterization of mantle convection (§4.2), the composition of the BMO (§4.3) and the radiogenic content of the planet (§4.4). Since the model is sensitive to these parameters, this highlights the need to better constrain these quantities with experiments and simulations at planetary interior conditions.

The initial temperature at the CMB, T_{CMB_0} , depends on the accretion history of the planet, and the efficiency of heat partitioning between the mantle and the core (Rubie et al., 2015). This requires understanding the conditions of magma ocean formation following giant impacts at the end of accretion (Tonks and Melosh, 1993; Nakajima and Stevenson, 2015; Nakajima et al., 2021), the processes that lead to the formation of long-lived BMO (Labrosse et al., 2015), and heat partitioning between metal and silicates during (Landeau et al., 2021; Lherm et al., 2022) and after (Deguen et al., 2014) the impacts. Furthermore, given the definition of T_{CMB_0} (§2.2.4), variations of this parameter may also be interpreted as uncertainties in the EOS, through the adiabatic temperature profile, and the liquidus of the BMO.

ggn

Mantle convection involves several parameters, including a critical Rayleigh number and the exponent of the $Nu \propto Ra^{\beta}$ relationship (Ricard, 2015). These parameters depend on the proportion of internal heating, the rheology of the mantle and partial melting (Driscoll and Bercovici, 2014), as well as the dynamics of plate tectonics. Mantle convection is also influenced by the mantle viscosity, which depends nonlinearly on temperature, pressure, stress and mineralogical variables (Ricard, 2015), the thermal conductivity, which depends on pressure and temperature (van den Berg et al., 2010), and the EOS, which depends on the composition of the solid mantle (Fumagalli and Klemme, 2015; Irifune and Tsuchiya, 2015).

The evolution of the planet depends on parameters related to composition, including in particular the iron partition coefficient D_{BMO} , the initial mass fraction ξ_{b_0} of FeO, the compositional density jump at the top of the BMO $\Delta_{\xi}\rho_{BMO}$, and at the compositional density jump at the ICB $\Delta_{\xi}\rho_{ICB}$. D_{BMO} has been determined experimentally for moderate iron concentrations, giving values in the range 0.1-0.6 (Nomura et al., 2011; Andrault et al., 2012; Tateno et al., 2014). Experimental dispersion might be explained by differences in the sample analyses, variations in the iron oxidation and spin states, and the presence of aluminium (Boukaré et al., 2015). D_{BMO} may also change at high iron concentrations (Blanc et al., 2020). ξ_{b_0} is expected to depend on the formation mechanism of the BMO (Labrosse et al., 2015), and metal-silicate equilibration during core formation (Rubie et al., 2015). In addition, the value of $\Delta_{\xi}\rho_{ICB}$, which depends on the light elements content of the core, is uncertain (Hirose et al., 2013), as is $\Delta_{\xi}\rho_{BMO}$ (Caracas et al., 2019). Finally, uncertainties in the EOS and liquidus of MgSiO₃ (Fratanduono et al., 2018; Wolf and Bower, 2018) and FeO (Morard et al., 2022; Dobrosavljevic et al., 2023) are likely to influence the value of these parameters. Our model is also expected to be sensitive to the crystallization sequence of the BMO (Boukaré et al., 2015; Nabiei et al., 2021).

The model depends on parameters related to radiogenic heating, including the mantle fraction f_h of BSE radiogenic production and the 40 K core concentration c_c . f_h depends on heat production in the convective mantle and the lithosphere. However, these radioactive heat sources remain uncertain, since the range of mantle and lithosphere heat production are respectively 9-17 TW and 7-8 TW (Jaupart et al., 2015). Similarly, the concentration of 40 K in the core is also uncertain, with proposed concentration exceeding 130 ppm (Hirose et al., 2013).

The magnetic evolution of the planet is also sensitive to the electrical conductivity σ_b of the silicates and the thermal conductivity k_c of the liquid metal (§4.5). In the BMO, *ab initio* calculations show that the thermal conductivity is expected to increase by several order of magnitude at high pressure and temperature conditions (Scipioni et al., 2017), and with the addition of metal (Holmström et al., 2018; Soubiran and Militzer, 2018; Stixrude et al., 2020). These calculations typically yield electrical conductivities in the range $10^4 - 10^5$ Pa.s, which cover our silicate dynamo threshold of $\sigma_b \ge 2.15 \times 10^4$ S.m⁻¹. As a result, the existence of a silicate dynamo on an Earth-like planet remains open to debate. In the core, recent experiments and simulations provide a relatively broad range of thermal conductivity (Ohta et al., 2016; Basu et al., 2020; Hsieh et al., 2020; Pozzo et al., 2022), falling within 20 - 250 W.m⁻¹.K⁻¹. This raises

questions about the age of the dynamo onset and inner core nucleation, as well as the need for an alternative mechanism to explain paleomagnetic data. In any case, the sensitivity of the model to these transport properties highlights the need to better constrain these quantities.

5.4. Model limitations and future opportunities

Our model has a number of limitations that offer opportunities for further work. The internal structure of the planet should be integrated self-consistently (Zhang and Rogers, 2022) using an EOS that accurately parameterizes the effects of thermal boundary layers, melting, and evolving compositions. The sensitivity of the model to the EOS and melting curves should also be explicitly evaluated. In the solid mantle, the parameterization of the EOS should be improved by including iron (Irifune and Tsuchiya, 2015) and additional phase transitions (Tsuchiya and Tsuchiya, 2011; Umemoto et al., 2017). In the BMO, an evolving multi-component composition in realistic pressure and temperature conditions should be included, by using for example, a crystallization sequence in the MgO – FeO – SiO₂ system (Boukaré et al., 2015; Nabiei et al., 2021). This could be used to parameterize the mantle liquidus more accurately than a linear phase diagram. The EOS of the BMO should also be parameterized using self-consistent integration, rather than simply the reference density profile of the solid mantle. In the core, light elements should influence the parameterization of both the EOS and the liquidus (Hirose et al., 2021).

The planet evolution should include conductive layers (Gomi et al., 2013; Laneuville et al., 2018; Greenwood et al., 2021) with conductive temperature profiles in the solid inner core, the stably-stratified layers, and the thermal boundary layers, where we presently overestimate the cooling rates by using adiabatic profiles. The dynamics of multi-phase flows beyond the low melt fraction rheological transition (Boukaré et al., 2015; Boukaré and Ricard, 2017) should be parameterized to allow for situations where the BMO is not necessarily well-mixed and adiabatic. The role of the density contrast between melt and crystals on the formation and evolution of the BMO should also be considered (Boukaré et al., 2015; Caracas et al., 2019; Nabiei et al., 2021). Radiogenic production should account for the fractionation of radioisotopes between the BMO and the mantle, as well as between between the outer and the inner core, during the crystallization of the liquid phases.

The magnetic evolution of the planet relies on scaling laws extrapolated over several orders of magnitude to reach the conditions of planetary interiors, potentially leading to dynamics invisible in the dynamo simulations (Christensen, 2010). These scaling laws, originally developed for the Earth's core, may be modified in the BMO, with a dynamo operating in a thinner shell (Heimpel et al., 2005) at a larger Prandtl number (Simitev and Busse, 2005). Furthermore, a dynamo produced in the BMO may interact with the underlying core. For example, even if the core is stably-stratified, vigorous horizontal flows are likely to develop, converting the BMO poloidal field into a toroidal field and leading to a reinforcement of the silicate dynamo (Ziegler and Stegman, 2013). Such interaction may require a criterion for dynamo

operation that accounts for the magnetic Reynolds number in both layers, *e.g.* a dynamo number (Ziegler and Stegman, 2013).

Beyond an Earth-like planet investigated in this paper, the model can be used to analyse the evolution of other objects likely to have a BMO. In addition to Venus (O'Rourke, 2020) and the Moon (Hamid et al., 2023), Mars has had a BMO that still exists today (Khan et al., 2023; Samuel et al., 2023). Beyond the Solar System, terrestrial exoplanets may host a BMO, in particular Super-Earths (Blaske and O'Rourke, 2021; Zhang and Rogers, 2022).

6. Conclusion

In this paper, we have investigated the structural, thermal, buoyancy, and magnetic evolution of an Earth-like planet, with a coupled mantle, long-lived BMO, and solid and/or liquid core. Using conservative parameters, we have produced an Earth-like nominal model that includes an early silicate dynamo. Our parameter sensitivity sweep of the model provides insight into the range of BMO electrical conductivity and core thermal conductivity required to sustain a dynamo.

In our nominal model, the Earth-like planet starts with high temperature, thick iron-rich BMO, and a fully liquid core. Vigorous convection in the BMO, primarily compositionally driven by release of FeO from above, provides a supercritical magnetic Reynolds number and sufficient power to sustain a silicate dynamo. The intense activity of the BMO limits the heat flow at the CMB, producing a stably-stratified core with no core dynamo at early times.

As the planet cools, the solidifying BMO is progressively enriched in iron, while the release rate of FeO, the crystallization rate of the BMO and the cooling rate at the CMB all progressively increase. Core convection then develops from the bottom up at 0.8 Gyr. Eventually, the convective power available to sustain a core dynamo increases, initiating a core dynamo at 1.2 Gyr.

At 1.0 Gyr, the silicate dynamo vanishes as the magnetic Reynolds number becomes subcritical in a progressively thinner BMO. The BMO solidifies at 2.8 Gyr, leaving a solid mantle overlying a liquid core. At 3.8 Gyr, the central core temperature drops below the core liquidus, nucleating the inner core. The onset of compositional convection from the release of light elements at the ICB suddenly increases the convective power, enhancing the core dynamo and magnetic field.

Our Earth-like nominal model is broadly consistent with the present-day Earth structure, as well as previous evolution models involving a long-lived BMO. The inner core radius, temperatures at the CMB and ICB, and heat flows at the CMB and surface are close to Earth's values. Our model is also largely consistent with paleomagnetic data, except before 1.0 Gyr where the model predicts a silicate dynamo with a relatively strong magnetic field intensity. However, its value is particularly sensitive to the magnetic scaling laws being used.

Declaration of competing interest

The authors declare that they have no known competing financial interests or personal relationships that could have appeared to influence the work reported in this paper.

1058 Data availability

Data will be made available on request.

Funding

1055

1059

1060

1068

1069

Funding for this research was provided by the Center for Matter at Atomic Pressure (CMAP), a National Science
Foundation (NSF) Physics Frontier Center, under award PHY-2020249. Any opinions, findings, conclusions or
recommendations expressed in this material are those of the author(s) and do not necessarily reflect those of the
National Science Foundation. E.B. acknowledges working in part at the Aspen Center for Physics, which is supported by
National Science Foundation grant PHY-2210452. M.N. was supported in part by the National Aeronautics and Space
Administration (NASA) grant numbers 80NSSC19K0514, 80NSSC21K1184, and 80NSSC22K0107. Partial funding
for M.N. was also provided by NSF EAR-2237730 and by the Alfred P. Sloan Foundation under grant G202114194.

A. Equation of state of the mantle

The isothermal bulk modulus K_T of the solid mantle is defined using a third order Vinet-Rydberg EOS

$$K_T = K_0 X^{-2} \exp\left[\eta(1-X)\right] \left[1 + (1-X)(\eta X + 1)\right]$$
(57)

where $X = (\hat{V}/\hat{V}_0)^{1/3}$ and $\eta = \frac{3}{2} (K'_0 - 1)$ (Vinet et al., 1989). The molar volume \hat{V} is related to the density through $\rho \hat{V} = \rho_0 \hat{V}_0 = M$, where M is the molar mass. Furthermore, \hat{V}_0 , ρ_0 , K_0 and K'_0 are the reference molar volume, density, bulk modulus and derivative of the bulk modulus with respect to pressure. These parameters, identical to those of Boujibar et al. (2020), are defined for each phase of the reference model (Table S2). The volume dependence of the thermal expansivity and the Grüneisen parameter are respectively

$$\alpha = \alpha_0 x^3, \tag{58}$$

$$\gamma = \gamma_0 x^{\gamma_1}, \tag{59}$$

where $x = \hat{V}/\hat{V}_0$. α_0 , γ_0 and γ_1 are parameters defined in Table S2.

B. Equation of state of the basal magma ocean

1076

For MgSiO₃, we use a generalized Rosenfeld-Tarazona EOS (Rosenfeld and Tarazona, 1998; Wolf and Bower, 2018)

$$\begin{split} \hat{F}_{\text{MgSiO}_{3}}(\hat{V},T) &= \hat{U}_{0} + \hat{E}_{0}(\hat{V}) + \Delta \hat{E}(\hat{V},T_{0} \to T) \\ &+ \hat{S}_{0}(T_{0} - T) + T_{0}\Delta \hat{S}(\hat{V},T_{0_{s}} \to T_{0}) - T\Delta \hat{S}(\hat{V},T_{0_{s}} \to T) + \hat{F}_{e}(\hat{V},T) \end{split} \tag{60}$$

where \hat{U}_0 is the reference energy at reference temperature T_0 and volume \hat{V}_0 , \hat{E}_0 is the potential contribution of the free energy at T_0 , $\Delta \hat{E}$ is the perturbation in internal energy from T_0 , $\Delta \hat{S}$ is the perturbation in entropy from T_{0_S} , with T_{0_S} the reference adiabatic temperature profile at reference entropy \hat{S}_0 , and \hat{F}_e is the electronic contribution of the free energy. The potential contribution is expressed as a third order Vinet-Rydberg EOS (Vinet et al., 1989)

$$\hat{E}_0 = 9K_0\hat{V}_0\eta^{-2} \left\{ 1 - [1 - \eta(1 - X)] \exp\left[(1 - X)\eta\right] \right\}. \tag{61}$$

1083 The perturbation in internal energy is

$$\Delta \hat{E}(\hat{V}, T_0 \to T) = b(\hat{V}) \left[\left(\frac{T}{T_0} \right)^m - 1 \right] + \frac{3}{2} n R(T - T_0), \tag{62}$$

where m is the power-law exponent of the generalized Rosenfeld-Tarazona model, n is the number of atoms in the chemical formula of the compound and R is the gas constant. Furthermore, $b(\hat{V})$ is a polynomial representation of the thermal coefficients b_n , i.e.

$$b(\hat{V}) = \sum_{n=0}^{4} b_n (x-1)^n.$$
(63)

1087 The perturbation in entropy is

$$\Delta \hat{S}(\hat{V}, T_{0_S} \to T) = b(\hat{V}) \frac{m}{m-1} T_0^{-m} \left[T^{m-1} - T_{0_S}^{m-1} \right] + \frac{3}{2} nR \ln \left(\frac{T}{T_{0_S}} \right). \tag{64}$$

The reference adiabatic temperature profile $T_{0_{\mathcal{S}}}$ is obtained with

$$T_{0_{\mathcal{S}}} = T_0 \exp\left(-\int_{\hat{V}_0}^{\hat{V}} \frac{\gamma}{\hat{V}'} d\hat{V}'\right),\tag{65}$$

where we use a modified Altshuler form of the Grüneisen parameter of MgSiO₃ (Fratanduono et al., 2018) as the reference Grüneisen parameter

$$\gamma = \gamma_{\infty} + (\gamma_0 - \gamma_{\infty}) \left(\frac{\rho}{\rho_{0_{\gamma}}} \right)^{-\gamma_1} + \gamma_{01} \exp \left[-\frac{(\rho - \rho_e)^2}{\rho_{\sigma}^2} \right]. \tag{66}$$

1091 The electronic contribution is expressed as

$$\hat{V}_{e} = \begin{cases} \zeta \left[TT_{e} \ln \left(\frac{T}{T_{e}} \right) - \frac{1}{2} (T^{2} - T_{e}^{2}) \right] & \text{if} \quad T > T_{e} \\ 0 & \text{if} \quad T \leq T_{e} \end{cases}, \tag{67}$$

The thermo-electronic heat capacity coefficient ζ and the electronic temperature T_e both depend on volume as

$$\zeta = \zeta_0 x^{\zeta_1}, \tag{68}$$

$$T_e = T_{e_0} x^{T_{e_1}}. (69)$$

The parameters used for the EOS of MgSiO₃ are defined in Table S5.

For FeO (Dorogokupets et al., 2017; Morard et al., 2022), we use

$$\hat{F}_{\text{FeO}}(\hat{V},T) = \hat{U}_0 + \hat{E}_0(\hat{V}) + \hat{F}_{th}(\hat{V},T) + \hat{F}_e(\hat{V},T) - \hat{F}_{th}(\hat{V},T_0) - \hat{F}_e(\hat{V},T_0) - a_S R(T-T_0), \tag{70}$$

where \hat{F}_{th} is the thermal contribution of the free energy and where the part proportional to a_S corresponds to the residual entropy of the liquid at 0 K. The potential contribution is expressed as a third order Vinet-Rydberg EOS (Eq. 61). The thermal contribution is expressed with the Einstein model, *i.e.* the Debye model in the high temperature limit

$$\hat{F}_{th} = 3nRT \ln \left[1 - \exp\left(-\frac{\Theta}{T}\right) \right]. \tag{71}$$

The Einstein temperature Θ is

1094

1098

$$\Theta = \Theta_0 x^{-\gamma_\infty} \exp\left[\frac{\gamma_0 - \gamma_\infty}{\gamma_1} \left(1 - x^{\gamma_1}\right)\right],\tag{72}$$

where Θ_0 is the Einstein temperature prefactor. γ_0 , γ_1 and γ_∞ are defined in the Altshuler form of the Grüneisen parameter

$$\gamma = \gamma_{\infty} + (\gamma_0 - \gamma_{\infty}) \left(\frac{\rho}{\rho_0}\right)^{-\gamma_1}. \tag{73}$$

The electronic contribution is expressed as

$$\hat{F}_e = -\frac{3}{2}nRe_0 x^{e_1} T^2 \tag{74}$$

The parameters used for the EOS of FeO are defined in Table S5.

C. Thermal conductivity of the mantle

In this model (van den Berg et al., 2010), the thermal conductivity is the sum of the phonon k_l , photon k_r and electronic k_e contributions, *i.e.*

$$k = k_1 + k_r + k_\varrho. (75)$$

The phonon contribution corresponds to a truncated version of the model of Hofmeister (1999)

$$k_l = \left(k_l^{*-2} + k_{\text{trunc}}^{-2}\right)^{-1/2},\tag{76}$$

1108 with

1104

$$k_l^* = k_{l_0} \left(\frac{T_P}{T}\right)^{a_k} \exp\left[-\left(4\gamma + \frac{1}{3}\right)\alpha(T - T_P)\right] \left(1 + \frac{P}{K_T}\frac{\mathrm{d}K_T}{\mathrm{d}P}\right),\tag{77}$$

where k_{l_0} and a_k are the phonon conductivity prefactor and exponent and k_{trunc} is the truncation value. The photon contribution is set to k_{r_0} in an operational temperature window defined by T_{r_1} , T_{r_2} , T_{r_3} and T_{r_4} , and tapered off to zero

outside of this window using sine functions

$$k_{r} = \begin{cases} 0 & \text{if} \quad T < T_{r_{1}} \\ \frac{k_{r_{0}}}{2} \left\{ 1 + \sin \left[\pi \left(\frac{T - T_{r_{1}}}{T_{r_{2}} - T_{r_{1}}} - \frac{1}{2} \right) \right] \right\} & \text{if} \quad T_{r_{1}} \le T < T_{r_{2}} \\ k_{r_{0}} & \text{if} \quad T_{r_{2}} \le T < T_{r_{3}} \\ \frac{k_{r_{0}}}{2} \left\{ 1 + \sin \left[\pi \left(\frac{T - T_{r_{3}}}{T_{r_{4}} - T_{r_{3}}} + \frac{1}{2} \right) \right] \right\} & \text{if} \quad T_{r_{3}} \le T < T_{r_{4}} \\ 0 & \text{if} \quad T \ge T_{r_{4}} \end{cases}$$

$$(78)$$

1112 The electronic contribution is defined as

1115

$$k_e = k_{e_0} \exp\left(-\frac{E_k}{k_B T}\right),\tag{79}$$

where k_{e_0} and E_k are the electron conductivity prefactor and an electron transport activation energy and k_B is the Boltzmann constant. The parameters of the model are defined in Table S6.

D. Expression of the crystallization rates

In the BMO (Fig. 15a), the infinitesimal temperature drop that occurs during δt is $\delta T = AD = AC + BD - BC$, where $AC = -(\mathrm{d}T/\mathrm{d}r)\delta r$, $BC = -(\mathrm{d}T_l/\mathrm{d}r)\delta r$ and $BD = (\mathrm{d}T_l/\mathrm{d}t)\delta t$. δr is the corresponding radius decrease of the interface between the BMO and the mantle. Since we assume an adiabatic temperature profile, the cooling rate at the top of the BMO is proportional to the cooling rate at the CMB (Eq. 22). Thus $\delta T = (T_{BMO}/T_{CMB})\delta T_{CMB}$, where δT_{CMB} is the infinitesimal temperature drop at the CMB. Using Eq. 27, we have $\mathrm{d}T_l/\mathrm{d}t = (\mathrm{d}T_l/\mathrm{d}\xi)C_{\xi_b}(\mathrm{d}R_{BMO}/\mathrm{d}t)$, where $\mathrm{d}T_l/\mathrm{d}\xi$ is the slope of the linear phase diagram (Eq. 13) at a given pressure. We finally write the crystallization rate as

$$\frac{\mathrm{d}R_{BMO}}{\mathrm{d}t} = \frac{T_{BMO}}{T_{CMB}} \left[\left(\frac{\mathrm{d}T_l}{\mathrm{d}r} - \frac{\mathrm{d}T}{\mathrm{d}r} \right)_{R_{BMO}} + \left(\frac{\mathrm{d}T_l}{\mathrm{d}\xi} \right)_{R_{BMO}} C_{\xi_b} \right]^{-1} \frac{\mathrm{d}T_{CMB}}{\mathrm{d}t} = C_{R_b} \frac{\mathrm{d}T_{CMB}}{\mathrm{d}t}. \tag{80}$$

In the core (Fig. 15b), the infinitesimal temperature drop is $\delta T = AC = AD - CD$, where $AD = (dT_l/dr)\delta r$ and $CD = (dT/dr)\delta r$. δr is the corresponding radius increase of the ICB. Since we assume an adiabatic temperature profile, the cooling rate at the ICB is in particular proportional to the cooling rate at the CMB (Eq. 22), which means that $\delta T = (T_{ICB}/T_{CMB})\delta T_{CMB}$. We can then write the crystallization rate as

$$\frac{\mathrm{d}R_{ICB}}{\mathrm{d}t} = \frac{1}{\left(\frac{\mathrm{d}T_l}{\mathrm{d}r} - \frac{\mathrm{d}T}{\mathrm{d}r}\right)_{R_{ICB}}} \frac{T_{ICB}}{\mathrm{d}t} \frac{\mathrm{d}T_{CMB}}{\mathrm{d}t} = C_{R_c} \frac{\mathrm{d}T_{CMB}}{\mathrm{d}t}.$$
(81)

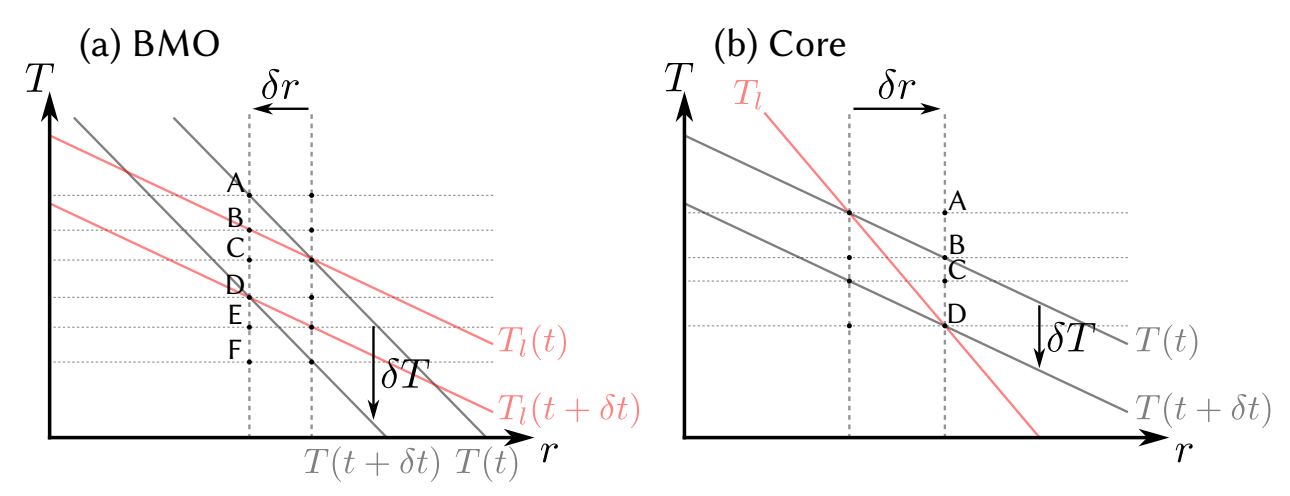


Figure 15: (a) Variation δr of the interface between the BMO and the mantle caused by a temperature decrease δT during a time δt . The adiabatic temperature T varies in response to the cooling of the BMO and changes in the composition of the BMO influence the mantle liquidus T_l . (b) Variation δr of the ICB radius caused by a temperature decrease δT during a time δt . The adiabatic temperature T varies in response to the cooling of the core but the mantle liquidus T_l is independent of the core composition.

E. Energy budget terms

1127

1128

1134

The radiogenic heating in the mantle is integrated over the volume V_m of the mantle

$$Q_{R,m} = \int_{V_m} \rho h_m f_h \mathrm{d}V \tag{82}$$

where h_m is the specific heat production rate of the BSE and f_h is the mantle fraction of the BSE production. We write the specific heat production rate as

$$h_m = \sum_i c_{m_i} a_i e_i \frac{N_A \lambda_i}{M_i} \exp\left[-\lambda_i (t - t_P)\right]$$
(83)

where c_{m_i} , a_i , e_i , M_i and λ_i are respectively the BSE concentration at $t = t_P = 4.5$ Gyr, the natural abundance, the energy per atom, the molar mass and the decay constant of the radioactive isotopes i. The radiogenic heating parameters are defined in Table S7.

The secular cooling of the mantle is

$$Q_{S,m} = -\int_{V_m} \rho c_P \frac{\mathrm{d}T_m}{\mathrm{d}t} \mathrm{d}V. \tag{84}$$

Using Eq. 22, the adiabatic temperature profile in the BMO allows to write (Gubbins et al., 2003)

$$\frac{1}{T_{BMO}} \frac{\mathrm{d}T_{BMO}}{\mathrm{d}t} = \frac{1}{T_{CMB}} \frac{\mathrm{d}T_{CMB}}{\mathrm{d}t},\tag{85}$$

which using Eq. 16 gives

$$\frac{\mathrm{d}T_m}{\mathrm{d}t} = \frac{1}{2} \frac{T_{BMO}}{T_{CMB}} \frac{\mathrm{d}T_{CMB}}{\mathrm{d}t}.$$
 (86)

The radiogenic heating in the BMO is integrated over the volume V_b of the BMO

$$Q_{R,b} = \int_{V_b} \rho h_m f_h \mathrm{d}V. \tag{87}$$

The secular cooling of the BMO is

$$Q_{S,b} = -\int_{V_b} \rho c_P \frac{T}{T_{CMB}} \frac{\mathrm{d}T_{CMB}}{\mathrm{d}t} \mathrm{d}V. \tag{88}$$

In Eq. 88, we assume an adiabatic temperature profile in the BMO (Eq. 22).

The gravitational energy of the BMO is

$$Q_{G,b} = \int_{V_b} \alpha_{c_b} \rho \psi \frac{\mathrm{D}\xi_b}{\mathrm{D}t} \mathrm{d}V, \tag{89}$$

where ψ is the gravitational potential. In Eq. 89, the compositional expansion coefficient α_{c_b} (Gubbins et al., 2004) is

$$\alpha_{c_b} = -\frac{1}{\rho} \left(\frac{\partial \rho}{\partial \xi} \right)_{P,T} \simeq \frac{\Delta_{\xi} \rho_{BMO}}{\rho_{BMO}^+ \Delta \xi_{BMO}},\tag{90}$$

where ρ_{BMO}^+ is the density in the solid mantle at the BMO interface and $\Delta_{\xi}\rho_{BMO}$ is the compositional contribution to the density jump due to a change in composition $\Delta\xi_{BMO}$ across the interface. Following Blanc et al. (2020), we use data from Caracas et al. (2019) to set $\Delta_{\xi}\rho_{BMO} = 250 \text{ kg.m}^{-3}$.

The latent heat of the BMO is

1145

$$Q_{L,b} = -4\pi R_{BMO}^2 \Delta S_m T_{BMO} \rho_{BMO}^- \frac{\mathrm{d}R_{BMO}}{\mathrm{d}t},\tag{91}$$

where $\Delta S_m = 300 \,\text{J.kg}^{-1}.\text{K}^{-1}$ is the entropy of fusion in the mantle (Labrosse et al., 2007).

The radiogenic heating in the core is integrated over the volume V_{oc} of the outer core

$$Q_{R,c} = \int_{V_{oc}} \rho h_c dV, \tag{92}$$

where h_c is the specific heat production rate of the core. The heat production rate is

$$h_c = c_c a_{40}_{\rm K} e_{40}_{\rm K} \frac{N_A \lambda_{40}_{\rm K}}{M_{40}_{\rm K}} \exp\left[-\lambda_{40}_{\rm K}(t - t_P)\right], \tag{93}$$

where c_c , a_{40} K, e_{40} K, M_{40} K and λ_{40} K are respectively the core concentration at $t = t_P$, the natural abundance, the energy per atom, the molar mass and the decay constant of 40 K. The radiogenic heating parameters are defined in Table S7.

The secular cooling of the outer core is

1151

1158

1160

1161

$$Q_{S,c} = -\int_{V_{cc}} \rho c_P \frac{T}{T_{CMB}} \frac{\mathrm{d}T_{CMB}}{\mathrm{d}t} \mathrm{d}V. \tag{94}$$

In Eq. 94, we assume an adiabatic temperature profile in the outer core (Eq. 22).

The gravitational energy of the core is

$$Q_{G,c} = \int_{V_{oc}} \alpha_{c_c} \rho \psi \frac{\mathrm{D}\xi_c}{\mathrm{D}t} \mathrm{d}V. \tag{95}$$

As with the BMO, the compositional expansion coefficient α_{c_a} (Gubbins et al., 2004) is

$$\alpha_{c_c} = -\frac{1}{\rho} \left(\frac{\partial \rho}{\partial \xi} \right)_{P,T} \simeq \frac{\Delta_{\xi} \rho_{ICB}}{\rho_{ICB}^{-} \Delta \xi_{ICB}},\tag{96}$$

where ρ_{ICB}^{-} is the density of the solid inner core at the ICB and $\Delta_{\xi}\rho_{ICB}$ is the compositional contribution to the density jump due to a change in composition $\Delta\xi_{ICB}$ across the interface. Following Labrosse (2015), we use data from Alfè et al. (1999) and Masters and Gubbins (2003) to set $\Delta_{\xi}\rho_{ICB} = 580 \text{ kg.m}^{-3}$.

The latent heat of the core is

$$Q_{L,c} = 4\pi R_{ICB}^2 \Delta S_c T_{ICB} \rho_{ICB}^+ \frac{dR_{ICB}}{dt},$$
(97)

where $\Delta S_c = 127 \text{ J.kg}^{-1} \cdot \text{K}^{-1}$ is the entropy of fusion in the core (Hirose et al., 2013; Labrosse, 2015).

The radiogenic heating of the inner is the core is integrated over the volume V_{ic} of the inner core

$$Q_{R,ic} = \int_{V_{ic}} \rho h_c dV. \tag{98}$$

The secular cooling of the inner core is

$$Q_{S,ic} = -\int_{V_{ic}} \rho c_P \frac{T_{ICB}}{T_{CMB}} \frac{dT_{CMB}}{dt} dV.$$
(99)

In Eq. 99, we assume an adiabatic temperature profile in the outer core (Eq. 22).

1163 F. Buoyancy source terms

1164

The volumetric buoyancy sources associated with radiogenic heating are

$$\begin{cases}
\epsilon_{R_b} = \frac{\bar{\alpha}}{\bar{c}_P} \left(\rho h_m f_h \right) \\
\epsilon_{R_c} = \frac{\bar{\alpha}}{\bar{c}_P} \left(\rho h_c \right)
\end{cases}$$
(100)

The boundary conditions, corresponding to the radiogenic heat flow at the top of the layer, are

$$\begin{cases} \kappa_T C'_{0_{R,b}}(r = R_{BMO}) &= -Q_{R,b} \frac{\tilde{\alpha}}{\tilde{c}_P} \frac{1}{4\pi R_{BMO}^2} \\ \kappa_T C'_{0_{R,c}}(r = R_{CMB}) &= -Q_{R,c} \frac{\tilde{\alpha}}{\tilde{c}_P} \frac{1}{4\pi R_{CMB}^2} \end{cases}$$
(101)

1166 The radiogenic mass anomaly fluxes are then

$$\begin{cases}
q_{R,b} = -\frac{1}{4\pi r^2} \frac{\bar{\alpha}}{\bar{c}_P} Q_{R,b} \left(\frac{r^3 - R_{CMB}^3}{R_{BMO}^3 - R_{CMB}^3} \right) \\
q_{R,c} = -\frac{1}{4\pi r^2} \frac{\bar{\alpha}}{\bar{c}_P} Q_{R,c} \left(\frac{r^3 - R_{ICB}^3}{R_{CMB}^3 - R_{ICB}^3} \right)
\end{cases}$$
(102)

The volumetric buoyancy sources associated with secular cooling are

$$\epsilon_{S_b} = \epsilon_{S_c} = \frac{\bar{\alpha}}{\bar{c}_P} \left(-\rho c_P \frac{T}{T_{CMB}} \frac{dT_{CMB}}{dt} \right). \tag{103}$$

The boundary conditions, corresponding to the secular heat flow at the top of the layer, are

$$\begin{cases} \kappa_T C'_{0_{S,b}}(r = R_{BMO}) &= -Q_{S,b} \frac{\bar{\alpha}}{\bar{c}_p} \frac{1}{4\pi R_{BMO}^2} \\ \kappa_T C'_{0_{S,c}}(r = R_{CMB}) &= -Q_{S,c} \frac{\bar{\alpha}}{\bar{c}_p} \frac{1}{4\pi R_{CMB}^2} \end{cases}$$
(104)

The secular mass anomaly fluxes are then

$$\begin{cases} q_{S,b} = -\frac{1}{r^2} \int_{R_{CMB}}^{r} x^2 \epsilon_{S_b} dx \\ q_{S,c} = -\frac{1}{r^2} \int_{R_{ICB}}^{r} x^2 \epsilon_{S_c} dx \end{cases}$$
(105)

The volumetric buoyancy sources associated with dissipation are

$$\begin{cases}
\epsilon_{G_b} = \frac{\bar{\alpha}}{\bar{c}_P} \left(\frac{Q_{G,b}}{V_b} \right) \\
\epsilon_{G_c} = \frac{\bar{\alpha}}{\bar{c}_P} \left(\frac{Q_{G,c}}{V_{oc}} \right)
\end{cases}$$
(106)

This term is not involved in the heat equation under the Boussinesq approximation, but it contributes to the total mass anomaly flux as a heat source for the convecting system (Gubbins et al., 2015). The distribution of the dissipation term depends on the actual velocity and the magnetic fields and is therefore unknown. Here, we thus assume a uniform dissipation throughout the layer. The boundary conditions, corresponding to the heat flow associated with the gravitational energy at the top of the layer, are

$$\begin{cases} \kappa_T C'_{0_{G,b}}(r = R_{BMO}) &= -Q_{G,b} \frac{\bar{\alpha}}{\bar{c}_P} \frac{1}{4\pi R_{BMO}^2} \\ \kappa_T C'_{0_{G,c}}(r = R_{CMB}) &= -Q_{G,c} \frac{\bar{\alpha}}{\bar{c}_P} \frac{1}{4\pi R_{CMB}^2} \end{cases}$$
(107)

The dissipation mass anomaly fluxes are then

1170

1177

$$\begin{cases}
q_{G,b} = -\frac{1}{4\pi r^2} \frac{\bar{\alpha}}{\bar{c}_P} Q_{G,b} \left(\frac{r^3 - R_{CMB}^3}{R_{BMO}^3 - R_{CMB}^3} \right) \\
q_{G,c} = -\frac{1}{4\pi r^2} \frac{\bar{\alpha}}{\bar{c}_P} Q_{G,c} \left(\frac{r^3 - R_{ICB}^3}{R_{CMB}^3 - R_{ICB}^3} \right)
\end{cases}$$
(108)

The volumetric buoyancy sources associated with the latent heat are

$$\epsilon_{L_b} = \epsilon_{L_c} = 0. \tag{109}$$

In the BMO, the latent heat is released at the top of the layer, it does not contribute to the buoyancy profile. The corresponding mass anomaly flux is therefore zero. In the core, the latent heat is released at the ICB, it passes through the outer core. Since there is no internal buoyancy source, the mass anomaly flux is determined by the boundary condition, obtained by converting the heat flow associated with latent heat at the ICB. This gives

$$\begin{cases} \kappa_T C'_{0_{L,b}}(r = R_{BMO}) = 0 \\ \kappa_T C'_{0_{L,c}}(r = R_{ICB}) = -Q_{L,c} \frac{\tilde{\alpha}}{\tilde{c}_P} \frac{1}{4\pi R_{ICB}^2}. \end{cases}$$
(110)

The latent heat mass anomaly fluxes are then

$$\begin{cases}
q_{L,b} = 0 \\
q_{L,c} = -\frac{1}{4\pi r^2} \frac{\bar{\alpha}}{\bar{c}_P} Q_{L,c}
\end{cases}$$
(111)

The volumetric buoyancy sources associated with the heat source at the CMB and the ICB are

$$\epsilon_{CMB} = \epsilon_{ICB} = 0. \tag{112}$$

Since the heat is released at the bottom of the layer, the internal buoyancy source is zero. The boundary conditions, corresponding to the heat flow at the CMB and the ICB, are

$$\begin{cases} \kappa_T C'_{0_{CMB}}(r = R_{CMB}) &= -Q_{CMB} \frac{\bar{\alpha}}{\bar{c}_P} \frac{1}{4\pi R_{CMB}^2} \\ \kappa_T C'_{0_{ICB}}(r = R_{ICB}) &= -Q_{ICB} \frac{\bar{\alpha}}{\bar{c}_P} \frac{1}{4\pi R_{ICB}^2} \end{cases}$$
(113)

The mass anomaly fluxes associated with the heat flow at the CMB and the ICB are then

$$\begin{cases}
q_{CMB} = -\frac{1}{4\pi r^2} \frac{\bar{\alpha}}{\bar{c}_P} Q_{CMB} \\
q_{ICB} = -\frac{1}{4\pi r^2} \frac{\bar{\alpha}}{\bar{c}_P} Q_{ICB}
\end{cases}$$
(114)

The volumetric buoyancy sources associated with compositional convection are

$$\begin{cases}
\epsilon_{C_b} = \bar{\rho}\alpha_{c_b} \frac{\mathrm{D}\xi_b}{\mathrm{D}t} \\
\epsilon_{C_c} = \bar{\rho}\alpha_{c_c} \frac{\mathrm{D}\xi_c}{\mathrm{D}t}
\end{cases}$$
(115)

If we neglect exchanges between the BMO and the core, as well as thermodiffusion and barodiffusion, the flux of FeO and light elements at the CMB are zero. The boundary conditions, corresponding to a zero mass anomaly flux at the CMB, are

$$\kappa_T C'_{0_{C,b}}(r = R_{CMB}) = \kappa_T C'_{0_{C,c}}(r = R_{CMB}) = 0.$$
(116)

The compositional mass anomaly fluxes, are then

$$\begin{cases}
q_{C,b} = -\frac{1}{3r^2} \epsilon_{C_b} \left(r^3 - R_{CMB}^3 \right) \\
q_{C,c} = -\frac{1}{3r^2} \epsilon_{C_c} \left(R_{CMB}^3 - r^3 \right)
\end{cases}$$
(117)

92 G. Entropy budget terms

1193

1194

1195

1198

1201

The radiogenic heating terms are respectively integrated over the volume of the BMO and the outer core

$$\begin{cases}
E_{R,b} = \int_{V_b} \rho h_m f_h \left(\frac{1}{T_{BMO}} - \frac{1}{T} \right) dV \\
E_{R,c} = \int_{V_{oc}} \rho h_c \left(\frac{1}{T_{CMB}} - \frac{1}{T} \right) dV
\end{cases}$$
(118)

The secular cooling terms, where we assume an adiabatic temperature profile (Eq. 22), are

$$\begin{cases} E_{S,b} = -\int_{V_b} \rho c_P \frac{1}{T_{CMB}} \left(\frac{T}{T_{BMO}} - 1 \right) \frac{dT_{CMB}}{dt} dV \\ E_{S,c} = -\int_{V_{oc}} \rho c_P \frac{1}{T_{CMB}} \left(\frac{T}{T_{CMB}} - 1 \right) \frac{dT_{CMB}}{dt} dV \end{cases}$$
(119)

The entropy terms, associated with the gravitational energy of the BMO and the core, are

$$\begin{cases}
E_{G,b} = \frac{Q_{G,b}}{T_{BMO}} \\
E_{G,c} = \frac{Q_{G,c}}{T_{CMB}}
\end{cases}$$
(120)

This terms are expected to have a higher efficiency than the other buoyancy sources due to the intrinsic definition of their efficiency factor (Nimmo, 2015a).

The latent heat terms in the BMO and the core are

$$\begin{cases} E_{L,b} = 0 \\ E_{L,c} = Q_{L,c} \left(\frac{1}{T_{CMB}} - \frac{1}{T_{ICB}} \right) \end{cases}$$
 (121)

Since the latent heat of the BMO is released at the top of the layer, this term does not contribute to the convection in the BMO and the corresponding rate of entropy production is zero (Blanc et al., 2020).

The entropy terms associated with the heat source at the CMB and the ICB are respectively

$$\begin{cases} E_{CMB} = Q_{CMB} \left(\frac{1}{T_{BMO}} - \frac{1}{T_{CMB}} \right) \\ E_{ICB} = Q_{ICB} \left(\frac{1}{T_{CMB}} - \frac{1}{T_{ICB}} \right) \end{cases}$$
 (122)

The thermal diffusion terms, obtained using adiabatic temperature profiles, are

$$\begin{cases}
E_{k,b} = \int_{V_b} k_b \left(\frac{\nabla T}{T}\right)^2 dV \\
E_{k,c} = \int_{V_{oc}} k_c \left(\frac{\nabla T}{T}\right)^2 dV
\end{cases}$$
(123)

The molecular diffusion terms, corresponding to a flux of FeO, or light elements, in a hydrostatic pressure gradient (Gubbins et al., 2004), are

$$\begin{cases}
E_{\alpha,b} = \alpha_{c_b}^2 \alpha_D \int_{V_b} \frac{g^2}{T} dV \\
E_{\alpha,c} = \alpha_{c_c}^2 \alpha_D \int_{V_{oc}} \frac{g^2}{T} dV
\end{cases},$$
(124)

where $\alpha_D = 1.0 \times 10^{12} \text{ kg.m}^{-3}$.s (Gubbins et al., 2004) is a material constant assumed to be identical in the BMO and the core. In these barodiffusion terms, we neglect thermodiffusion and assume a well-mixed liquid associated with zero concentration diffusion.

H. Velocity and magnetic scaling laws

1202

1208

1216

The convective power, or total dissipation (Buffett et al., 1996; Lister, 2003), available to the dynamo in the BMO or the outer core is approximated by

$$\Phi = F_i \left(\bar{\psi} - \psi_i \right) + F_o \left(\psi_o - \bar{\psi} \right), \tag{125}$$

where F_i and F_o are the mass anomaly flow rates at the inner and outer boundary of the layer, ψ_i and ψ_o are the gravitational potential at the corresponding boundaries and $\bar{\psi}$ is the mass-averaged gravitational potential in the layer. Eq. 125 shows that the convective power is produced by taking the mass anomaly flow rate at the gravitational potential of the inner and outer boundaries, and redistributing it in the layer at the mean gravitational potential, which implies in particular that the layer is well-mixed.

In practice, we obtain the convective power from the dissipation term of the entropy budget with

$$\Phi = E_{\Phi} T_D = \begin{cases} E_{\Phi} \left(\frac{1}{M_b} \int_{V_b} \frac{\rho}{T} dV \right)^{-1} \\ E_{\Phi} \left(\frac{1}{M_{oc}} \int_{V_{oc}} \frac{\rho}{T} dV \right)^{-1} \end{cases}, \tag{126}$$

where T_D is an effective dissipation temperature calculated using the mass-averaged adiabatic temperature profile (Labrosse, 2003). Following Aubert et al. (2009), the convective power is made dimensionless with

$$\tilde{\Phi} = \begin{cases} \frac{\Phi}{M_b \Omega^3 L_b^2} \\ \frac{\Phi}{M_{oc} \Omega^3 L_c^2} \end{cases} . \tag{127}$$

Fig. 16 shows the Rossby number and the dimensionless internal magnetic field intensity as a function of the dimensionless convective power. Scaling laws, fitted on a set of numerical dynamo simulations (Aubert et al., 2009), are compared with scaling laws based on force balance arguments (Christensen, 2010), *i.e.* the MLT, CIA and MAC regimes. The scaling law parameters are defined in Table S8. In both the BMO and the core, the range of dimensionless convective power predicted by the entropy budget (shaded areas) is several orders of magnitude smaller than the convective power obtained in the dynamo simulations (black markers). This implies in particular that even a moderate variation of the scaling law exponent may be responsible for significant changes in the convective velocities and magnetic field intensities. This explains the magnetic evolution variability observed in the nominal model, depending on the exponent of the scaling law (Fig. 9).

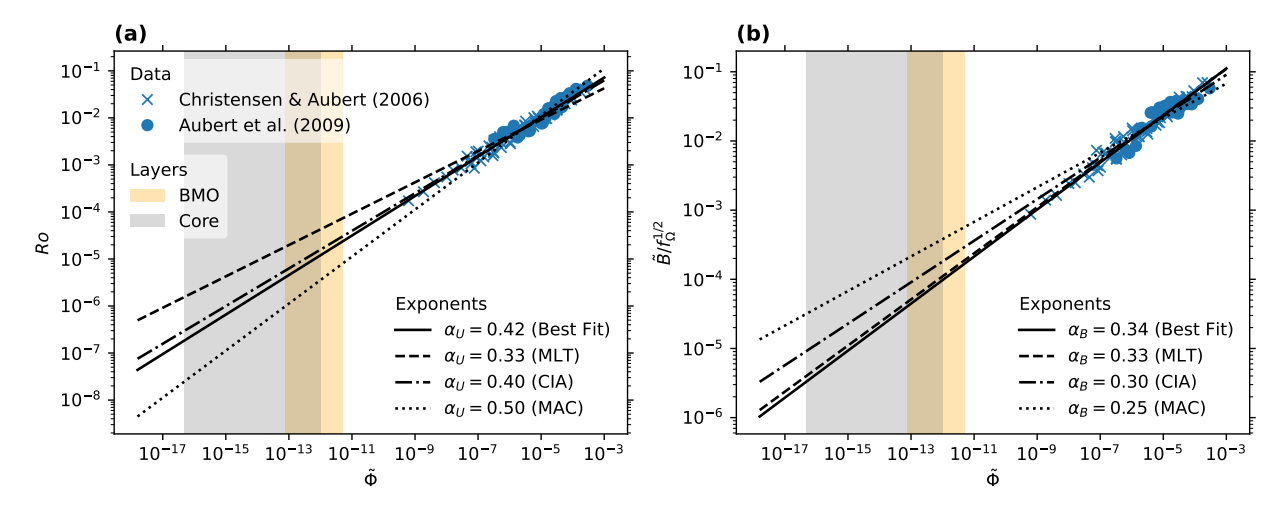


Figure 16: (a) Scaling of the Rossby number Ro as a function of the dimensionless convective power $\tilde{\Phi}$. (b) Scaling of the dimensionless internal magnetic field intensity, normalized by $f_{\Omega}^{1/2}$, where f_{Ω} is the ohmic dissipation fraction of the convective power, as a function of the dimensionless convective power $\tilde{\Phi}$. The black markers correspond to the set of MHD simulations extracted from Aubert et al. (2009), but respectively computed by Christensen and Aubert (2006) (crosses) and Aubert et al. (2009) (disks). The solid lines correspond to the best-fit power-law scaling obtained by Aubert et al. (2009) using a least-square fit in the set of MHD simulations. The dashed lines correspond to power-law scalings, obtained using a least-square fit on the set of MHD simulations, with an imposed exponent derived from the mixing length theory (MLT), the Coriolis-Inertia-Archimedean (CIA) or the Magnetic-Archimedean-Coriolis (MAC) regime (Christensen, 2010). The orange and gray shaded areas correspond respectively to the dimensionless convective power derived from the entropy budget in the BMO and the core, with $R_m > 40$.

CRediT authorship contribution statement

- Victor Lherm: Conceptualization, Methodology, Software, Formal analysis, Writing Original Draft. Miki
- Nakajima: Conceptualization, Methodology, Formal analysis, Writing Original Draft. Eric G. Blackman: Con-
- ceptualization, Methodology, Formal analysis, Writing Original Draft.

1232 References

- Alfè, D., Gillan, M.J., Price, G.D., 1999. The melting curve of iron at the pressures of the Earth's core from ab initio calculations. Nature 401,
- 1234 462-464.
- Alken, P., Thébault, E., Beggan, C.D., Amit, H., Aubert, J., Baerenzung, J., Bondar, T.N., Brown, W.J., Califf, S., Chambodut, A., Chulliat, A., Cox,
- 1236 G.A., Finlay, C.C., Fournier, A., Gillet, N., Grayver, A., Hammer, M.D., Holschneider, M., Huder, L., Hulot, G., Jager, T., Kloss, C., Korte, M.,
- Kuang, W., Kuvshinov, A., Langlais, B., Léger, J.M., Lesur, V., Livermore, P.W., Lowes, F.J., Macmillan, S., Magnes, W., Mandea, M., Marsal,
- 1238 S., Matzka, J., Metman, M.C., Minami, T., Morschhauser, A., Mound, J.E., Nair, M., Nakano, S., Olsen, N., Pavón-Carrasco, F.J., Petrov, V.G.,
- Ropp, G., Rother, M., Sabaka, T.J., Sanchez, S., Saturnino, D., Schnepf, N.R., Shen, X., Stolle, C., Tangborn, A., Tøffner-Clausen, L., Toh,
- H., Torta, J.M., Varner, J., Vervelidou, F., Vigneron, P., Wardinski, I., Wicht, J., Woods, A., Yang, Y., Zeren, Z., Zhou, B., 2021. International
- Geomagnetic Reference Field: The thirteenth generation. Earth, Planets and Space 73, 49.
- Andrault, D., Petitgirard, S., Lo Nigro, G., Devidal, J.L., Veronesi, G., Garbarino, G., Mezouar, M., 2012. Solid-liquid iron partitioning in Earth's
- deep mantle. Nature 487, 354–357.
- Aubert, J., Labrosse, S., Poitou, C., 2009. Modelling the palaeo-evolution of the geodynamo. Geophysical Journal International 179, 1414–1428.
- Backus, G.E., 1975. Gross Thermodynamics of Heat Engines in Deep Interior of Earth. Proceedings of the National Academy of Sciences 72,
- 1246 1555-1558.
- 1247 Badro, J., Aubert, J., Hirose, K., Nomura, R., Blanchard, I., Borensztajn, S., Siebert, J., 2018. Magnesium Partitioning Between Earth's Mantle and
- Core and its Potential to Drive an Early Exsolution Geodynamo. Geophysical Research Letters 45, 13,240–13,248.
- Ballmer, M.D., Lourenço, D.L., Hirose, K., Caracas, R., Nomura, R., 2017. Reconciling magma-ocean crystallization models with the present-day
- structure of the Earth's mantle. Geochemistry, Geophysics, Geosystems 18, 2785–2806.
- Basu, A., Field, M.R., McCulloch, D.G., Boehler, R., 2020. New measurement of melting and thermal conductivity of iron close to outer core
- conditions. Geoscience Frontiers 11, 565–568.
- Biggin, A.J., de Wit, M.J., Langereis, C.G., Zegers, T.E., Voûte, S., Dekkers, M.J., Drost, K., 2011. Palaeomagnetism of Archaean rocks of the
- Onverwacht Group, Barberton Greenstone Belt (southern Africa): Evidence for a stable and potentially reversing geomagnetic field at ca. 3.5Ga.
- Earth and Planetary Science Letters 302, 314–328.
- 1256 Biggin, A.J., Piispa, E.J., Pesonen, L.J., Holme, R., Paterson, G.A., Veikkolainen, T., Tauxe, L., 2015. Palaeomagnetic field intensity variations
- suggest Mesoproterozoic inner-core nucleation. Nature 526, 245–248.
- 1258 Blackman, E.G., Tarduno, J.A., 2018. Mass, energy, and momentum capture from stellar winds by magnetized and unmagnetized planets:
- 1259 Implications for atmospheric erosion and habitability. Monthly Notices of the Royal Astronomical Society 481, 5146–5155.
- Blanc, N.A., Stegman, D.R., Ziegler, L.B., 2020. Thermal and magnetic evolution of a crystallizing basal magma ocean in Earth's mantle. Earth
- and Planetary Science Letters 534, 116085.
- Blaske, C.H., O'Rourke, J.G., 2021. Energetic Requirements for Dynamos in the Metallic Cores of Super-Earth and Super-Venus Exoplanets. Journal
- of Geophysical Research: Planets 126, e2020JE006739.

- Bonati, I., Lasbleis, M., Noack, L., 2021. Structure and Thermal Evolution of Exoplanetary Cores. Journal of Geophysical Research: Planets 126,
- 1265 e2020JE006724.
- Bono, R.K., Paterson, G.A., van der Boon, A., Engbers, Y.A., Michael Grappone, J., Handford, B., Hawkins, L.M.A., Lloyd, S.J., Sprain, C.J.,
- Thallner, D., Biggin, A.J., 2022. The PINT database: A definitive compilation of absolute palaeomagnetic intensity determinations since 4
- billion years ago. Geophysical Journal International 229, 522–545.
- Borlina, C.S., Weiss, B.P., Lima, E.A., Tang, F., Taylor, R.J.M., Einsle, J.F., Harrison, R.J., Fu, R.R., Bell, E.A., Alexander, E.W., Kirkpatrick,
- 1270 H.M., Wielicki, M.M., Harrison, T.M., Ramezani, J., Maloof, A.C., 2020. Reevaluating the evidence for a Hadean-Eoarchean dynamo. Science
- 1271 Advances 6, eaav9634.
- Boujibar, A., Driscoll, P., Fei, Y., 2020. Super-Earth Internal Structures and Initial Thermal States. Journal of Geophysical Research: Planets 125,
- 1273 e2019JE006124.
- Boukaré, C.E., Ricard, Y., 2017. Modeling phase separation and phase change for magma ocean solidification dynamics. Geochemistry, Geophysics,
- 1275 Geosystems 18, 3385–3404.
- 1276 Boukaré, C.E., Ricard, Y., Fiquet, G., 2015. Thermodynamics of the MgO-FeO-SiO2 system up to 140 GPa: Application to the crystallization of
- Earth's magma ocean. Journal of Geophysical Research: Solid Earth 120, 6085–6101.
- Boyet, M., Carlson, R.W., 2005. 142Nd Evidence for Early (>4.53 Ga) Global Differentiation of the Silicate Earth. Science 309, 576–581.
- 1279 Braginsky, S.I., Roberts, P.H., 1995. Equations governing convection in earth's core and the geodynamo. Geophysical & Astrophysical Fluid
- 1280 Dynamics 79, 1–97.
- Buffett, B.A., Huppert, H.E., Lister, J.R., Woods, A.W., 1996. On the thermal evolution of the Earth's core. Journal of Geophysical Research: Solid
- 1282 Earth 101, 7989-8006.
- Camprubí, E., de Leeuw, J.W., House, C.H., Raulin, F., Russell, M.J., Spang, A., Tirumalai, M.R., Westall, F., 2019. The Emergence of Life. Space
- Science Reviews 215, 56.
- Canup, R.M., Asphaug, E., 2001. Origin of the Moon in a giant impact near the end of the Earth's formation. Nature 412, 708–712.
- 1286 Caracas, R., Hirose, K., Nomura, R., Ballmer, M.D., 2019. Melt-crystal density crossover in a deep magma ocean. Earth and Planetary Science
- 1287 Letters 516, 202-211.
- Chen, L., Herreman, W., Li, K., Livermore, P.W., Luo, J.W., Jackson, A., 2018. The optimal kinematic dynamo driven by steady flows in a sphere.
- Journal of Fluid Mechanics 839, 1–32.
- 1290 Christensen, U.R., 2010. Dynamo Scaling Laws and Applications to the Planets. Space Science Reviews 152, 565–590.
- 1291 Christensen, U.R., Aubert, J., 2006. Scaling properties of convection-driven dynamos in rotating spherical shells and application to planetary
- magnetic fields. Geophysical Journal International 166, 97–114.
- 1293 Christensen, U.R., Wicht, J., 2015. 8.10 Numerical Dynamo Simulations, in: Schubert, G. (Ed.), Treatise on Geophysics (Second Edition). Elsevier,
- 1294 Oxford, pp. 245–277.
- 1295 Cuk, M., Stewart, S.T., 2012. Making the Moon from a Fast-Spinning Earth: A Giant Impact Followed by Resonant Despinning. Science 338,
- 1296 1047-1052.
- Daher, H., Arbic, B.K., Williams, J.G., Ansong, J.K., Boggs, D.H., Müller, M., Schindelegger, M., Austermann, J., Cornuelle, B.D., Crawford, E.B.,
- Fringer, O.B., Lau, H.C.P., Lock, S.J., Maloof, A.C., Menemenlis, D., Mitrovica, J.X., Green, J.A.M., Huber, M., 2021. Long-Term Earth-Moon
- Evolution With High-Level Orbit and Ocean Tide Models. Journal of Geophysical Research: Planets 126, e2021JE006875.
- Davies, C.J., 2015. Cooling history of Earth's core with high thermal conductivity. Physics of the Earth and Planetary Interiors 247, 65–79.
- Davies, C.J., Gubbins, D., 2011. A buoyancy profile for the Earth's core. Geophysical Journal International 187, 549–563.

- de Koker, N., Steinle-Neumann, G., Vlček, V., 2012. Electrical resistivity and thermal conductivity of liquid Fe alloys at high P and T, and heat
- flux in Earth's core. Proceedings of the National Academy of Sciences 109, 4070–4073.
- Deguen, R., Landeau, M., Olson, P., 2014. Turbulent metal-silicate mixing, fragmentation, and equilibration in magma oceans. Earth and Planetary
- 1305 Science Letters 391, 274–287.
- 1306 Deng, J., Stixrude, L., 2021. Thermal Conductivity of Silicate Liquid Determined by Machine Learning Potentials. Geophysical Research Letters
- 1307 48, e2021GL093806.
- Dobrosavljevic, V.V., Zhang, D., Sturhahn, W., Chariton, S., Prakapenka, V.B., Zhao, J., Toellner, T.S., Pardo, O.S., Jackson, J.M., 2023. Melting
- and defect transitions in FeO up to pressures of Earth's core-mantle boundary. Nature Communications 14, 7336.
- Dorogokupets, P.I., Dymshits, A.M., Litasov, K.D., Sokolova, T.S., 2017. Thermodynamics and Equations of State of Iron to 350 GPa and 6000 K.
- Scientific Reports 7, 41863.
- 1312 Driscoll, P., Bercovici, D., 2014. On the thermal and magnetic histories of Earth and Venus: Influences of melting, radioactivity, and conductivity.
- Physics of the Earth and Planetary Interiors 236, 36–51.
- Driscoll, P., Davies, C., 2023. The "New Core Paradox": Challenges and Potential Solutions. Journal of Geophysical Research: Solid Earth 128,
- 1315 e2022JB025355.
- Driscoll, P., Olson, P., 2011. Optimal dynamos in the cores of terrestrial exoplanets: Magnetic field generation and detectability. Icarus 213, 12–23.
- Du, Z., Boujibar, A., Driscoll, P., Fei, Y., 2019. Experimental Constraints on an MgO Exsolution-Driven Geodynamo. Geophysical Research Letters
- 1318 46, 7379–7385.
- Du, Z., Jackson, C., Bennett, N., Driscoll, P., Deng, J., Lee, K.K.M., Greenberg, E., Prakapenka, V.B., Fei, Y., 2017. Insufficient Energy From MgO
- Exsolution to Power Early Geodynamo. Geophysical Research Letters 44, 11,376–11,381.
- 1321 Dziewonski, A.M., Anderson, D.L., 1981. Preliminary reference Earth model. Physics of the Earth and Planetary Interiors 25, 297–356.
- 1322 Dziewonski, A.M., Hager, B.H., O'Connell, R.J., 1977. Large-scale heterogeneities in the lower mantle. Journal of Geophysical Research (1896-
- 1323 1977) 82, 239–255.
- Egan, H., Jarvinen, R., Ma, Y., Brain, D., 2019. Planetary magnetic field control of ion escape from weakly magnetized planets. Monthly Notices
- of the Royal Astronomical Society 488, 2108–2120.
- Fei, Y., Seagle, C.T., Townsend, J.P., McCoy, C.A., Boujibar, A., Driscoll, P., Shulenburger, L., Furnish, M.D., 2021. Melting and density of MgSiO3
- determined by shock compression of bridgmanite to 1254GPa. Nature Communications 12, 876.
- 1328 Fischer, R.A., Campbell, A.J., Ciesla, F.J., 2017. Sensitivities of Earth's core and mantle compositions to accretion and differentiation processes.
- Earth and Planetary Science Letters 458, 252–262.
- Fratanduono, D.E., Millot, M., Kraus, R.G., Spaulding, D.K., Collins, G.W., Celliers, P.M., Eggert, J.H., 2018. Thermodynamic properties of
- MgSiO3 at super-Earth mantle conditions. Physical Review B 97, 214105.
- Fumagalli, P., Klemme, S., 2015. 2.02 Mineralogy of the Earth: Phase Transitions and Mineralogy of the Upper Mantle, in: Schubert, G. (Ed.),
- 1333 Treatise on Geophysics (Second Edition). Elsevier, Oxford, pp. 7–31.
- Garnero, E.J., Grand, S.P., Helmberger, D.V., 1993. Low P-wave velocity at the base of the mantle. Geophysical Research Letters 20, 1843–1846.
- Garnero, E.J., McNamara, A.K., 2008. Structure and Dynamics of Earth's Lower Mantle. Science 320, 626–628.
- Gomi, H., Ohta, K., Hirose, K., Labrosse, S., Caracas, R., Verstraete, M.J., Hernlund, J.W., 2013. The high conductivity of iron and thermal evolution
- of the Earth's core. Physics of the Earth and Planetary Interiors 224, 88–103.
- Grannan, A., Favier, B., Le Bars, M., Aurnou, J., 2017. Tidally forced turbulence in planetary interiors. Geophysical Journal International 208,
- 1339 1690-1703.

- Greenwood, S., Davies, C.J., Mound, J.E., 2021. On the evolution of thermally stratified layers at the top of Earth's core. Physics of the Earth and
- Planetary Interiors 318, 106763.
- Gubbins, D., Alfè, D., Davies, C., Pozzo, M., 2015. On core convection and the geodynamo: Effects of high electrical and thermal conductivity.
- Physics of the Earth and Planetary Interiors 247, 56–64.
- Gubbins, D., Alfè, D., Davies, C.J., 2013. Compositional instability of Earth's solid inner core. Geophysical Research Letters 40, 1084–1088.
- Gubbins, D., Alfè, D., Masters, G., Price, G.D., Gillan, M., 2004. Gross thermodynamics of two-component core convection. Geophysical Journal
- 1346 International 157, 1407–1414.
- Gubbins, D., Alfè, D., Masters, G., Price, G.D., Gillan, M.J., 2003. Can the Earth's dynamo run on heat alone? Geophysical Journal International
- 1348 155, 609–622.
- Gunell, H., Maggiolo, R., Nilsson, H., Wieser, G.S., Slapak, R., Lindkvist, J., Hamrin, M., Keyser, J.D., 2018. Why an intrinsic magnetic field does
- not protect a planet against atmospheric escape. Astronomy & Astrophysics 614, L3.
- Hamid, S.S., O'Rourke, J.G., Soderlund, K.M., 2023. A Long-lived Lunar Magnetic Field Powered by Convection in the Core and a Basal Magma
- Ocean. The Planetary Science Journal 4, 88.
- Heimpel, M.H., Aurnou, J.M., Al-Shamali, F.M., Gomez Perez, N., 2005. A numerical study of dynamo action as a function of spherical shell
- geometry. Earth and Planetary Science Letters 236, 542–557.
- Hewitt, J.M., Mckenzie, D.P., Weiss, N.O., 1975. Dissipative heating in convective flows. Journal of Fluid Mechanics 68, 721–738.
- Hirose, K., Labrosse, S., Hernlund, J., 2013. Composition and State of the Core. Annual Review of Earth and Planetary Sciences 41, 657–691.
- 1357 Hirose, K., Morard, G., Sinmyo, R., Umemoto, K., Hernlund, J., Helffrich, G., Labrosse, S., 2017. Crystallization of silicon dioxide and
- compositional evolution of the Earth's core. Nature 543, 99–102.
- Hirose, K., Wood, B., Vočadlo, L., 2021. Light elements in the Earth's core. Nature Reviews Earth & Environment 2, 645–658.
- Hofmeister, A.M., 1999. Mantle Values of Thermal Conductivity and the Geotherm from Phonon Lifetimes. Science 283, 1699–1706.
- Holmström, E., Stixrude, L., Scipioni, R., Foster, A.S., 2018. Electronic conductivity of solid and liquid (Mg, Fe)O computed from first principles.
- Earth and Planetary Science Letters 490, 11–19.
- Howard, L.N., 1966. Convection at high Rayleigh number, in: Görtler, H. (Ed.), Applied Mechanics, Springer, Berlin, Heidelberg. pp. 1109–1115.
- Hsieh, W.P., Goncharov, A.F., Labrosse, S., Holtgrewe, N., Lobanov, S.S., Chuvashova, I., Deschamps, F., Lin, J.F., 2020. Low thermal conductivity
- of iron-silicon alloys at Earth's core conditions with implications for the geodynamo. Nature Communications 11, 3332.
- 1366 Irifune, T., Tsuchiya, T., 2015. 2.03 Phase Transitions and Mineralogy of the Lower Mantle, in: Schubert, G. (Ed.), Treatise on Geophysics (Second
- Edition). Elsevier, Oxford, pp. 33-60.
- Jaupart, C., Labrosse, S., Lucazeau, F., Mareschal, J.C., 2015. 7.06 Temperatures, Heat, and Energy in the Mantle of the Earth, in: Schubert, G.
- (Ed.), Treatise on Geophysics (Second Edition). Elsevier, Oxford, pp. 223–270.
- Jones, C.A., 2015. 8.05 Thermal and Compositional Convection in the Outer Core, in: Schubert, G. (Ed.), Treatise on Geophysics (Second Edition).
- 1371 Elsevier, Oxford, pp. 115–159.
- Karato, S.i., Murthy, VR., 1997. Core formation and chemical equilibrium in the Earth—I. Physical considerations. Physics of the Earth and
- Planetary Interiors 100, 61–79.
- Kendall, J.D., Melosh, H.J., 2016. Differentiated planetesimal impacts into a terrestrial magma ocean: Fate of the iron core. Earth and Planetary
- 1375 Science Letters 448, 24–33.
- Khan, A., Huang, D., Durán, C., Sossi, P.A., Giardini, D., Murakami, M., 2023. Evidence for a liquid silicate layer atop the Martian core. Nature
- 1377 622, 718–723.

- Labrosse, S., 2003. Thermal and magnetic evolution of the Earth's core. Physics of the Earth and Planetary Interiors 140, 127–143.
- Labrosse, S., 2014. Thermal and compositional stratification of the inner core. Comptes Rendus Geoscience 346, 119–129.
- Labrosse, S., 2015. Thermal evolution of the core with a high thermal conductivity. Physics of the Earth and Planetary Interiors 247, 36–55.
- Labrosse, S., Hernlund, J.W., Coltice, N., 2007. A crystallizing dense magma ocean at the base of the Earth's mantle. Nature 450, 866.
- Labrosse, S., Hernlund, J.W., Hirose, K., 2015. Fractional Melting and Freezing in the Deep Mantle and Implications for the Formation of a Basal
- Magma Ocean, in: The Early Earth. American Geophysical Union (AGU). chapter 7, pp. 123–142.
- Labrosse, S., Poirier, J.P., Le Mouël, J.L., 1997. On cooling of the Earth's core. Physics of the Earth and Planetary Interiors 99, 1–17.
- Labrosse, S., Poirier, J.P., Le Mouël, J.L., 2001. The age of the inner core. Earth and Planetary Science Letters 190, 111–123.
- Landeau, M., Deguen, R., Phillips, D., Neufeld, J.A., Lherm, V., Dalziel, S.B., 2021. Metal-silicate mixing by large Earth-forming impacts. Earth
- and Planetary Science Letters 564, 116888.
- Landeau, M., Fournier, A., Nataf, H.C., Cébron, D., Schaeffer, N., 2022. Sustaining Earth's magnetic dynamo. Nature Reviews Earth & Environment
- 1389 , 1–15.
- Laneuville, M., Hernlund, J., Labrosse, S., Guttenberg, N., 2018. Crystallization of a compositionally stratified basal magma ocean. Physics of the
- Earth and Planetary Interiors 276, 86–92.
- Lay, T., 2015. 1.22 Deep Earth Structure: Lower Mantle and D", in: Schubert, G. (Ed.), Treatise on Geophysics (Second Edition). Elsevier, Oxford,
- pp. 683-723.
- Le Bars, M., Cébron, D., Le Gal, P., 2015. Flows Driven by Libration, Precession, and Tides. Annual Review of Fluid Mechanics 47, 163–193.
- Lejeune, A.M., Richet, P., 1995. Rheology of crystal-bearing silicate melts: An experimental study at high viscosities. Journal of Geophysical
- 1396 Research: Solid Earth 100, 4215–4229.
- 1397 Lekic, V., Cottaar, S., Dziewonski, A., Romanowicz, B., 2012. Cluster analysis of global lower mantle tomography: A new class of structure and
- implications for chemical heterogeneity. Earth and Planetary Science Letters 357–358, 68–77.
- Lherm, V., Deguen, R., 2018. Small-Scale Metal/Silicate Equilibration During Core Formation: The Influence of Stretching Enhanced Diffusion
- on Mixing. Journal of Geophysical Research: Solid Earth 123, 10,496–10,516.
- Lherm, V., Deguen, R., 2023. Velocity field and cavity dynamics in drop impact experiments. Journal of Fluid Mechanics 962, A21.
- Lherm, V., Deguen, R., Alboussière, T., Landeau, M., 2022. Rayleigh–Taylor instability in impact cratering experiments. Journal of Fluid Mechanics
- 1403 937.
- Lister, J.R., 2003. Expressions for the dissipation driven by convection in the Earth's core. Physics of the Earth and Planetary Interiors 140, 145–158.
- Lister, J.R., Buffett, B.A., 1995. The strength and efficiency of thermal and compositional convection in the geodynamo. Physics of the Earth and
- Planetary Interiors 91, 17–30.
- Loper, D.E., 1975. Torque balance and energy budget for the precessionally driven dynamo. Physics of the Earth and Planetary Interiors 11, 43–60.
- Loper, D.E., 1978. The gravitationally powered dynamo. Geophysical Journal of the Royal Astronomical Society 54, 389–404.
- Lundin, R., Lammer, H., Ribas, I., 2007. Planetary Magnetic Fields and Solar Forcing: Implications for Atmospheric Evolution. Space Science
- 1410 Reviews 129, 245–278.
- Malkus, W.V.R., 1968. Precession of the Earth as the Cause of Geomagnetism. Science 160, 259–264.
- Masters, G., Gubbins, D., 2003. On the resolution of density within the Earth. Physics of the Earth and Planetary Interiors 140, 159–167.
- 1413 Mittal, T., Knezek, N., Arveson, S.M., McGuire, C.P., Williams, C.D., Jones, T.D., Li, J., 2020. Precipitation of multiple light elements to power
- Earth's early dynamo. Earth and Planetary Science Letters 532, 116030.

- 1415 Morard, G., Antonangeli, D., Bouchet, J., Rivoldini, A., Boccato, S., Miozzi, F., Boulard, E., Bureau, H., Mezouar, M., Prescher, C., Chariton, S.,
- Greenberg, E., 2022. Structural and Electronic Transitions in Liquid FeO Under High Pressure. Journal of Geophysical Research: Solid Earth
- 1417 127, e2022JB025117.
- Mukhopadhyay, S., 2012. Early differentiation and volatile accretion recorded in deep-mantle neon and xenon. Nature 486, 101-104.
- Mundl, A., Touboul, M., Jackson, M.G., Day, J.M.D., Kurz, M.D., Lekic, V., Helz, R.T., Walker, R.J., 2017. Tungsten-182 heterogeneity in modern
- ocean island basalts. Science 356, 66–69.
- Nabiei, F., Badro, J., Boukaré, C.E., Hébert, C., Cantoni, M., Borensztajn, S., Wehr, N., Gillet, P., 2021. Investigating Magma Ocean Solidification
- on Earth Through Laser-Heated Diamond Anvil Cell Experiments. Geophysical Research Letters 48, e2021GL092446.
- Nakajima, M., Golabek, G.J., Wünnemann, K., Rubie, D.C., Burger, C., Melosh, H.J., Jacobson, S.A., Manske, L., Hull, S.D., 2021. Scaling laws
- for the geometry of an impact-induced magma ocean. Earth and Planetary Science Letters 568, 116983.
- Nakajima, M., Stevenson, D.J., 2015. Melting and mixing states of the Earth's mantle after the Moon-forming impact. Earth and Planetary Science
- 1426 Letters 427, 286-295.
- Ni, H., Hui, H., Steinle-Neumann, G., 2015. Transport properties of silicate melts. Reviews of Geophysics 53, 715–744.
- Nimmo, F., 2015a. 8.02 Energetics of the Core, in: Schubert, G. (Ed.), Treatise on Geophysics (Second Edition). Elsevier, Oxford, pp. 27–55.
- Nimmo, F., 2015b. 9.08 Thermal and Compositional Evolution of the Core, in: Schubert, G. (Ed.), Treatise on Geophysics (Second Edition).
- 1430 Elsevier, Oxford, pp. 201–219.
- Nimmo, F., Price, G.D., Brodholt, J., Gubbins, D., 2004. The influence of potassium on core and geodynamo evolution. Geophysical Journal
- 1432 International 156, 363–376.
- Nomura, R., Ozawa, H., Tateno, S., Hirose, K., Hernlund, J., Muto, S., Ishii, H., Hiraoka, N., 2011. Spin crossover and iron-rich silicate melt in the
- 1434 Earth's deep mantle. Nature 473, 199–202.
- Ohta, K., Kuwayama, Y., Hirose, K., Shimizu, K., Ohishi, Y., 2016. Experimental determination of the electrical resistivity of iron at Earth's core
- conditions. Nature 534, 95–98.
- 1437 Olson, P., 2013. The New Core Paradox. Science 342, 431–432.
- Olson, P., Weeraratne, D., 2008. Experiments on metal-silicate plumes and core formation. Philosophical Transactions of the Royal Society A:
- Mathematical, Physical and Engineering Sciences 366, 4253–4271.
- 1440 O'Rourke, J.G., 2020. Venus: A Thick Basal Magma Ocean May Exist Today. Geophysical Research Letters 47, e2019GL086126.
- 1441 O'Rourke, J.G., Gillmann, C., Tackley, P., 2018. Prospects for an ancient dynamo and modern crustal remanent magnetism on Venus. Earth and
- Planetary Science Letters 502, 46–56.
- O'Rourke, J.G., Korenaga, J., Stevenson, D.J., 2017. Thermal evolution of Earth with magnesium precipitation in the core. Earth and Planetary
- 1444 Science Letters 458, 263–272.
- 1445 O'Rourke, J.G., Stevenson, D.J., 2016. Powering Earth's dynamo with magnesium precipitation from the core. Nature 529, 387–389.
- Pozzo, M., Davies, C., Gubbins, D., Alfè, D., 2012. Thermal and electrical conductivity of iron at Earth's core conditions. Nature 485, 355–358.
- Pozzo, M., Davies, C.J., Alfè, D., 2022. Towards reconciling experimental and computational determinations of Earth's core thermal conductivity.
- Earth and Planetary Science Letters 584, 117466.
- Reddy, K.S., Favier, B., Le Bars, M., 2018. Turbulent Kinematic Dynamos in Ellipsoids Driven by Mechanical Forcing. Geophysical Research
- 1450 Letters 45, 1741–1750.
- Ricard, Y., 2015. 7.02 Physics of Mantle Convection, in: Schubert, G. (Ed.), Treatise on Geophysics (Second Edition). Elsevier, Oxford, pp. 23–71.

- Rochester, M.G., Jacobs, J.A., Smylie, D.E., Chong, K.F., 1975. Can Precession Power the Geomagnetic Dynamo? Geophysical Journal International
- 1453 43, 661–678.
- Rosenfeld, Y., Tarazona, P., 1998. Density functional theory and the asymptotic high density expansion of the free energy of classical solids and
- fluids. Molecular Physics 95, 141–150.
- Rubie, D.C., Melosh, H.J., Reid, J.E., Liebske, C., Righter, K., 2003. Mechanisms of metal-silicate equilibration in the terrestrial magma ocean.
- Earth and Planetary Science Letters 205, 239–255.
- Rubie, D.C., Nimmo, F., Melosh, H.J., 2015. 9.03 Formation of the Earth's Core, in: Schubert, G. (Ed.), Treatise on Geophysics (Second Edition).
- Elsevier, Oxford, pp. 43–79.
- Rubin, A.M., 1995. Propagation of Magma-Filled Cracks. Annual Review of Earth and Planetary Sciences 23, 287–336.
- Samuel, H., Drilleau, M., Rivoldini, A., Xu, Z., Huang, Q., Garcia, R.F., Lekić, V., Irving, J.C.E., Badro, J., Lognonné, P.H., Connolly, J.A.D.,
- Kawamura, T., Gudkova, T., Banerdt, W.B., 2023. Geophysical evidence for an enriched molten silicate layer above Mars's core. Nature 622,
- 1463 712–717.
- Samuel, H., Tackley, P.J., Evonuk, M., 2010. Heat partitioning in terrestrial planets during core formation by negative diapirism. Earth and Planetary
- 1465 Science Letters 290, 13–19.
- scheinberg, A.L., Soderlund, K.M., Elkins-Tanton, L.T., 2018. A basal magma ocean dynamo to explain the early lunar magnetic field. Earth and
- Planetary Science Letters 492, 144–151.
- 1468 Schubert, G., Turcotte, D.L., Olson, P., 2001. Mantle Convection in the Earth and Planets. Cambridge University Press.
- scipioni, R., Stixrude, L., Desjarlais, M.P., 2017. Electrical conductivity of SiO2 at extreme conditions and planetary dynamos. Proceedings of the
- National Academy of Sciences 114, 9009–9013.
- 1471 Seager, S., Kuchner, M., Hier-Majumder, C.A., Militzer, B., 2007. Mass-Radius Relationships for Solid Exoplanets. The Astrophysical Journal
- 1472 669, 1279.
- Simitev, R., Busse, F.H., 2005. Prandtl-number dependence of convection-driven dynamos in rotating spherical fluid shells. Journal of Fluid
- 1474 Mechanics 532, 365–388,
- 1475 Simon, F., Glatzel, G., 1929. Bemerkungen zur Schmelzdruckkurve. Zeitschrift für anorganische und allgemeine Chemie 178, 309–316.
- Solomatov, V.S., 1995. Scaling of temperature- and stress-dependent viscosity convection. Physics of Fluids 7, 266–274.
- Solomatov, V.S., Stevenson, D.J., 1993. Nonfractional crystallization of a terrestrial magma ocean. Journal of Geophysical Research: Planets 98,
- 1478 5391-5406.
- 1479 Soubiran, F., Militzer, B., 2018. Electrical conductivity and magnetic dynamos in magma oceans of Super-Earths. Nature Communications 9, 3883.
- Stacey, F.D., 1973. The Coupling of the Core to the Precession of the Earth. Geophysical Journal International 33, 47–55.
- Stacey, F.D., Anderson, O.L., 2001. Electrical and thermal conductivities of Fe-Ni-Si alloy under core conditions. Physics of the Earth and
- 1482 Planetary Interiors 124, 153–162.
- 1483 Stacey, F.D., Loper, D.E., 2007. A revised estimate of the conductivity of iron alloy at high pressure and implications for the core energy balance.
- Physics of the Earth and Planetary Interiors 161, 13–18.
- Stevenson, D.J., 2003. Planetary science: Mission to Earth's core a modest proposal. Nature 423, 239.
- 1486 Stixrude, L., 2014. Melting in super-earths. Philosophical Transactions of the Royal Society A: Mathematical, Physical and Engineering Sciences
- 1487 372, 20130076.
- Stixrude, L., Scipioni, R., Desjarlais, M.P., 2020. A silicate dynamo in the early Earth. Nature Communications 11, 935.

- Tarduno, J.A., Blackman, E.G., Mamajek, E.E., 2014. Detecting the oldest geodynamo and attendant shielding from the solar wind: Implications
- for habitability. Physics of the Earth and Planetary Interiors 233, 68–87.
- Tarduno, J.A., Cottrell, R.D., Bono, R.K., Oda, H., Davis, W.J., Fayek, M., van 't Erve, O., Nimmo, F., Huang, W., Thern, E.R., Fearn, S., Mitra,
- 1492 G., Smirnov, A.V., Blackman, E.G., 2020. Paleomagnetism indicates that primary magnetite in zircon records a strong Hadean geodynamo.
- Proceedings of the National Academy of Sciences 117, 2309–2318.
- Tarduno, J.A., Cottrell, R.D., Davis, W.J., Nimmo, F., Bono, R.K., 2015. A Hadean to Paleoarchean geodynamo recorded by single zircon crystals.
- science 349, 521-524.
- Tarduno, J.A., Cottrell, R.D., Watkeys, M.K., Hofmann, A., Doubrovine, P.V., Mamajek, E.E., Liu, D., Sibeck, D.G., Neukirch, L.P., Usui, Y., 2010.
- Geodynamo, Solar Wind, and Magnetopause 3.4 to 3.45 Billion Years Ago. Science 327, 1238–1240.
- Tateno, S., Hirose, K., Ohishi, Y., 2014. Melting experiments on peridotite to lowermost mantle conditions. Journal of Geophysical Research: Solid
- 1499 Earth 119, 4684-4694.
- Taylor, R.J.M., Reddy, S.M., Saxey, D.W., Rickard, W.D.A., Tang, F., Borlina, C.S., Fu, R.R., Weiss, B.P., Bagot, P., Williams, H.M., Harrison,
- R.J., 2023. Direct age constraints on the magnetism of Jack Hills zircon. Science Advances 9, eadd1511.
- Thorne, M.S., Garnero, E.J., 2004. Inferences on ultralow-velocity zone structure from a global analysis of SPdKS waves. Journal of Geophysical
- Research: Solid Earth 109.
- Tilgner, A., 2005. Precession driven dynamos. Physics of Fluids 17, 034104.
- Tonks, W.B., Melosh, H.J., 1993. Magma ocean formation due to giant impacts. Journal of Geophysical Research: Planets 98, 5319-5333.
- Touma, J., Wisdom, J., 1994. Evolution of the Earth-Moon System. The Astronomical Journal 108, 1943.
- Tsuchiya, T., Tsuchiya, J., 2011. Prediction of a hexagonal SiO₂ phase affecting stabilities of MgSiO₃ and CaSiO₃ at multimegabar pressures.
- Proceedings of the National Academy of Sciences 108, 1252–1255.
- 1509 Umemoto, K., Wentzcovitch, R.M., Wu, S., Ji, M., Wang, C.Z., Ho, K.M., 2017. Phase transitions in MgSiO3 post-perovskite in super-Earth mantles.
- Earth and Planetary Science Letters 478, 40–45.
- Valencia, D., O'Connell, R.J., Sasselov, D., 2006. Internal structure of massive terrestrial planets. Icarus 181, 545-554.
- van den Berg, A.P., Yuen, D.A., Beebe, G.L., Christiansen, M.D., 2010. The dynamical impact of electronic thermal conductivity on deep mantle
- convection of exosolar planets. Physics of the Earth and Planetary Interiors 178, 136–154.
- Verhoogen, J., 1961. Heat Balance of the Earth's Core. Geophysical Journal of the Royal Astronomical Society 4, 276–281.
- Vinet, P., Rose, J.H., Ferrante, J., Smith, J.R., 1989. Universal features of the equation of state of solids. Journal of Physics: Condensed Matter 1,
- 1516 1941.
- 1517 Williams, Q., 2018. The Thermal Conductivity of Earth's Core: A Key Geophysical Parameter's Constraints and Uncertainties. Annual Review of
- Earth and Planetary Sciences 46, 47–66.
- Wolf, A.S., Bower, D.J., 2018. An equation of state for high pressure-temperature liquids (RTpress) with application to MgSiO3 melt. Physics of
- the Earth and Planetary Interiors 278, 59–74.
- ¹⁵²¹ Zhang, J., Rogers, L.A., 2022. Thermal Evolution and Magnetic History of Rocky Planets. The Astrophysical Journal 938, 131.
- ziegler, L.B., Stegman, D.R., 2013. Implications of a long-lived basal magma ocean in generating Earth's ancient magnetic field. Geochemistry,
- Geophysics, Geosystems 14, 4735–4742.